

AD-A184 173

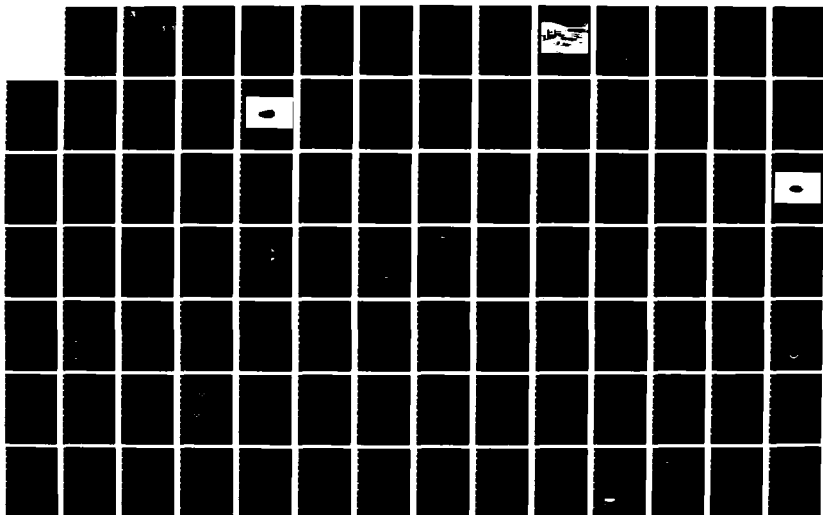
PLASMA THRUSTER DEVELOPMENT(U) STUTTGART UNIV (GERMANY  
F R) INST FUER RAUMFAHRTANTRIEBE H O SCHRADE ET AL  
JUL 87 IRS-87-P-10 AFAL-TR-87-053 AFOSR-84-0394

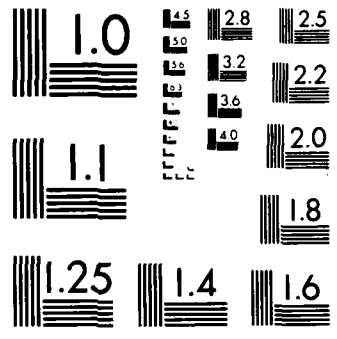
1/2

UNCLASSIFIED

F/G 21/3

NL





MICROCOPY RESOLUTION TEST CHART  
NATIONAL BUREAU OF STANDARDS 1963-A



AFAL TR-87-053

AD:

DTIC FILE COPY

2

Final Report  
for the period  
October 1984 to  
September 1986

# Plasma Thruster Development

DTIC  
ELECTE  
SEP 02 1987  
S D

July 1987

Authors:  
H. O. Schrade  
M. Auweter-Kurtz  
H. L. Kurtz  
W. D. Merke  
P. C. Sleziona

Institut Für Raumfahrtsysteme  
Universität Stuttgart  
Pfaffenwalkring 31  
D-7000 Stuttgart 80  
West Germany

IRS-87-P-10  
AFOSR-84-0394

AD-A184 173

### Approved for Public Release

Distribution is unlimited. The AFAL Technical Services Office has reviewed this report, and it is releasable to the National Technical Information Service, where it will be available to the general public, including foreign nationals.

*prepared for the:* **Air Force  
Astronautics  
Laboratory**

Air Force Space Technology Center  
Space Division, Air Force Systems Command  
Edwards Air Force Base,  
California 93523-5000

**DISTRIBUTION STATEMENT A**

Approved for public release  
Distribution Unlimited

87 3 1 3 8

## NOTICE

When U.S. Government drawings, specifications, or other data are used for any purpose other than a definitely related government procurement operation, the government thereby incurs no responsibility nor any obligation whatsoever, and the fact that the government may have formulated, furnished, or in any way supplied the said drawings, specifications, or other data, is not to be regarded by implication or otherwise, or conveying any rights or permission to manufacture, use, or sell any patented invention that may in any way be related thereto.

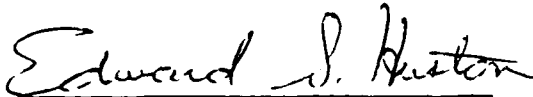
## FOREWORD

This final report was prepared for the Air Force Astronautics Laboratory (AFAL) under contract AFOSR 84-0394 by the University of Stuttgart, Federal Republic of West Germany. The study was performed during the period October 1984 to September 1986. Project Manager for the AFRPL was Lt Robert D. Meya.

This technical report has been reviewed and is approved for publication and distribution in accordance with the distribution statement on the cover and on the DD Form 1473.

  
\_\_\_\_\_  
ROBERT D. MEYA, 1Lt, USAF  
Project Manager

FOR THE COMMANDER

  
\_\_\_\_\_  
EDWARD S. HUSTON, Maj, USAF  
Chief, Space Propulsion Branch

  
\_\_\_\_\_  
CLARK W. HAWK  
Chief, Liquid Rocket Division

## REPORT DOCUMENTATION PAGE

1a. REPORT SECURITY CLASSIFICATION unclassified		1b. RESTRICTIVE MARKINGS	
2a. SECURITY CLASSIFICATION AUTHORITY		3. DISTRIBUTION/AVAILABILITY OF REPORT Approved for Public Release, Distribution is Unlimited.	
2b. DECLASSIFICATION/DOWNGRADING SCHEDULE			
4. PERFORMING ORGANIZATION REPORT NUMBER(S) IRS-87-P-10		5. MONITORING ORGANIZATION REPORT NUMBER(S) AFAL-TR-87-053	
6a. NAME OF PERFORMING ORGANIZATION Institut für Raumfahrtssysteme Universität Stuttgart	6b. OFFICE SYMBOL (If applicable)	7a. NAME OF MONITORING ORGANIZATION Air Force Astronautics Laboratory	
6c. ADDRESS (City, State and ZIP Code) Pfaffenwaldring 31 D-7000 Stuttgart 80 West Germany		7b. ADDRESS (City, State and ZIP Code) AFAL / LKCJ Edwards AFB, CA 93523-5000	
8a. NAME OF FUNDING/SPONSORING ORGANIZATION Air Force Office of Scientific Research	8b. OFFICE SYMBOL (If applicable)	9. PROCUREMENT INSTRUMENT IDENTIFICATION NUMBER AFOSR-84-0394	
8c. ADDRESS (City, State and ZIP Code) Bolling AFB Washington, DC 20036		10. SOURCE OF FUNDING NOS.	
11. TITLE (Include Security Classification) Plasma Thruster Development (U)		PROGRAM ELEMENT NO. 62302F	PROJECT NO. 5730
		TASK NO. 00	WORK UNIT NO. GS
12. PERSONAL AUTHOR(S) H. O. Schrade, M. Auweter-Kurtz, H. L. Kurtz, W. D. Merke, P. C. Sleziona			
13a. TYPE OF REPORT Final	13b. TIME COVERED FROM 84/10 TO 86/9	14. DATE OF REPORT (Yr., Mo., Day) 87/7	15. PAGE COUNT 117
16. SUPPLEMENTARY NOTATION			
17. COSATI CODES		18. SUBJECT TERMS (Continue on reverse if necessary and identify by block number)	
FIELD 21	GROUP 03	Electric Propulsion, MPD Propulsion, Electrode Erosion, Flow Discharge	
19. ABSTRACT			
Coaxial plasma accelerators without an external field are operated stationarily at discharge currents between 800 and 5000 A, using argon and nitrogen as main propellants. The influence of ambient pressure, cathode position, anode gas injection and different propellant masses on the performance are investigated. Experimental results are presented for two geometries, a nozzle-type and a cylindrical one. With the nozzle-type thruster, the influence of anode gas injection on performance is not significantly changed for up to 10% anode gas mass fraction, but the onset phenomena are split. A spotty anode attachment is shifted to higher current values. The occurrence of oscillations of 200 - 300 kHz, which almost coincides at no anode gas with these anode			
20. DISTRIBUTION/AVAILABILITY OF ABSTRACT UNCLASSIFIED/UNLIMITED <input checked="" type="checkbox"/> SAME AS RPT <input type="checkbox"/> DTIC USERS <input type="checkbox"/>		21. ABSTRACT SECURITY CLASSIFICATION unclassified	
22a. NAME OF RESPONSIBLE INDIVIDUAL Robert D. Meya, 1Lt, USAF		22b. TELEPHONE NUMBER (Include Area Code) (805) 275-5473	22c. OFFICE SYMBOL LKCJ

spots, is with anode gas injection clearly distinct from it. The incidence of these instabilities is also delayed with rising anode gas, but in a slower manner than the spot phenomenon. This indicates different onset mechanisms. Nitrogen as propellant shows no merit over argon in the investigated current ranges; the discharge voltage is higher and thus it lowers the efficiency. First experiments with a cylindrical thruster are demonstrated. They show the feasibility of a hot, protruding cathode and anode current attachment dependencies on the cathode position. A concept of a 200 - 300 kW MPD thruster with a radiation-cooled anode is presented.

Since there are differences in the results of steady state and quasi-steady pulsed thrusters, experiments with thrusters similar in geometry and electrode material have also been performed in quasi-steady operation mode. They indicate lower performances due to lower thrust, higher discharge voltages and lower onset points. Data of quasi-steady thrusters cannot be extrapolated to the continuous mode.

Cathode erosion studies were made for cold cathodes (pulsed thrusters and ignition phase of steady state ones) and hot cathodes. They indicate an erosion of almost three orders of magnitude higher with the cold cathode than with the hot ones. An explanation by spotty arc attachment to the cathode is given.

Three theoretical models for calculating the current and flow distributions in self-field MPD thrusters are being developed and will be applied to evaluate the effects of geometry, propellant type, scale and other parameters on the thruster performance.

- 1) A semi-analytical, two-dimensional code based on a source flow model.
- 2) For continuous thrusters, a stationary code is being developed. The extended Ohm's law is used to calculate the current contour lines, and a one-dimensional, two-component expansion flow model is used to obtain the velocity, temperature and pressure distributions for calculating the gas properties, which are again used in Ohm's law. The differential equation is solved by means of a finite difference method for the geometry of the nozzle-type plasma thruster DT2, which has been investigated at IRS in a steady state as well as in a quasi-steady state mode.

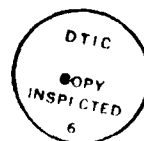
An integration over the volume and thermal forces equals to the thrust. The calculated current density distribution and the computed thrust are compared with experimental results.

- 3) For the starting phase of the steady state MPD thrusters as well as for pulsed thrusters, a time dependent, fully two-dimensional code is being developed. It uses a modified McCormack FD method in cylindrical coordinates to calculate the time dependent flow, temperature and pressure fields. The current and magnetic contour lines, which must be known for the energy and impulse input in this code, are calculated with an instantaneous Ohm's law solved in a manner similar to the computer code for continuous thrusters. This code is used for a simplified cylindrical thruster model.

TABLE OF CONTENTS

	Page
1. Introduction	2
2. Steady State Self-Field MPD Thrusters	5
1. Nozzle-Type Thrusters	5
2. Cylindrical MPD Thruster	31
3. Hot Anode Thruster	37
3. Quasi-Steady Pulsed MPD Thrusters	40
4. Cathode Erosion	56
5. Numerical Modeling	79
1. Semi-Empirical Hgel Code	79
2. Steady State MPD Thruster Calculations	80
3. Time Dependent Two-Dimensional Code	85
6. Mission Optimizations Calculations	104
7. List of Reports and Publications	105
8. References	108

Accession For	
NTIS CRA&I	<input checked="" type="checkbox"/>
DTIC TAB	<input type="checkbox"/>
Unannounced Justification	<input type="checkbox"/>
By _____	
Distribution/	
Availability Codes	
Dist	Avail and/or Special
A-1	



## 1. Introduction

Despite the present great lead of ion engines in development level, performance and life for sizes up to several kW, new interest in magnetoplasmadynamic thrusters for higher power levels (up to hundreds of kW) has arisen in recent years. Mission studies<sup>1,2</sup> showed specific impulse values between 1000 and 2000 s for orbit raising and orbit transfers for optimized mass savings and trip times, and advantages for MPD propulsion even with relatively low efficiencies.

With the probable realization of the SP-100 nuclear space power plant, sufficient power would also be available for steady state MPD propulsion, so that the benefits of these thrusters versus pulsed ones could be utilized; i.e., the ruggedness and simplicity of power and propellant conditioning and the about 3 orders of magnitude smaller cathode erosion. But there are also disadvantages of steady state thrusters; e.g., with quasi-steady ones (but with other geometries) the achieved efficiencies and specific impulses were in some cases higher.<sup>3</sup>

The research work covered in this report deals with these and related problems: in chapter two, the experimental results with nozzle-type and cylindrical thrusters are presented. The influence of cathode position, ambient pressure, anode gas injection and propellant type on the performance is investigated. The thruster design studies and the heat transfer calculations for the MPD thruster with a radiation-cooled anode are reported.

With the continuously running Stuttgart thrusters, the critical  $I^2/\dot{m}$  values and therefore the attainable specific impulses are smaller compared with the data read at Princeton and Tokyo. To check whether these differences are a function of the design configuration or of the operation mode, thrusters identical in geometry and electrode material were built and tested in both the continuously running and the pulsed mode. The experimental results are discussed in chapter 3.

Chapter 4 reports about erosion measurements on pulsed and continuous MPD thrusters. In the case of steady state operation, two different kinds of erosion must be distinguished: erosion during starting phase, when the cathode is cold, and the much lower erosion during steady state operation, when the cathode is hot. For both phases, the cathode mass loss has been separately measured. Erosion measurements on a pulsed thruster with the same electrode material and geometry allow the comparison of both operation modes with respect to electrode erosion.

The theoretical evaluation of the electrode erosion mechanisms, also a part of chapter 4, has been carried out under contract AFOSR 82-0298.<sup>4</sup>

Parallel to the experimental investigations, analytical and numerical approaches to determine flow, pressure, temperature and current density field of the midstream flow discharge region in MPD thrusters were carried out (partly under Grant AFOSR 82-0298). These programs are applied to the specific geometries of the Stuttgart thrusters. In chapter 5, results are demonstrated and compared with experiments.

The steady state experiments presented are made possible by a facility unique in Europe with highly regulated (low ripple) dc power up to 48,000 A and 6 MW continuous. A large flexible vacuum system with up to about 33 m<sup>3</sup>/s (33,000 l/s) pumping capacity permits continuous testing over a wide range of tank pressures and massflow values. Tank pressures at or below  $2 \cdot 10^{-2}$  mbar, adequate at least for self-field thrusters, can be maintained with a flow rate of up to 1 g/s with argon. The vacuum system blank-off pressure (without the large tanks) is  $4 \times 10^{-4}$  mbar, and with tanks connected at present about  $10^{-3}$  mbar--the difference being due to moisture and other outgassing, e.g. from leaks and from the silicone oil of the thrust balance.

In Fig. 1 a view of the laboratory hall of the IRS, as of summer 1986, is shown with the different vacuum tanks and the computer platform.



## 2. Steady State MPD Thrusters

### 2.1 Nozzle-Type Thruster

The emphasis of the design and test work during the research period has been on nozzle-type self-field MPD thrusters.

Two different design concepts with both the same nozzle and electrode dimensions were investigated. While the first, DT1 (Fig. 2), originates from a DFVLR concept of Hügel<sup>5</sup> and was built for argon as propellant, the newer DT2 (Fig. 3), with thinner segmentation allowed molecular propellants as well as argon. Thinner segmentation avoids breakdown between the segments and is necessary, since the voltage drop along the arc axis and the nozzle wall increases by taking nitrogen and hydrogen as propellants.

The thrusters consist of an upstream cathode made of 2% thoriated tungsten which is cast in a water-cooled copper rod, an arc chamber, and an expansion nozzle. The arc chamber and nozzle are

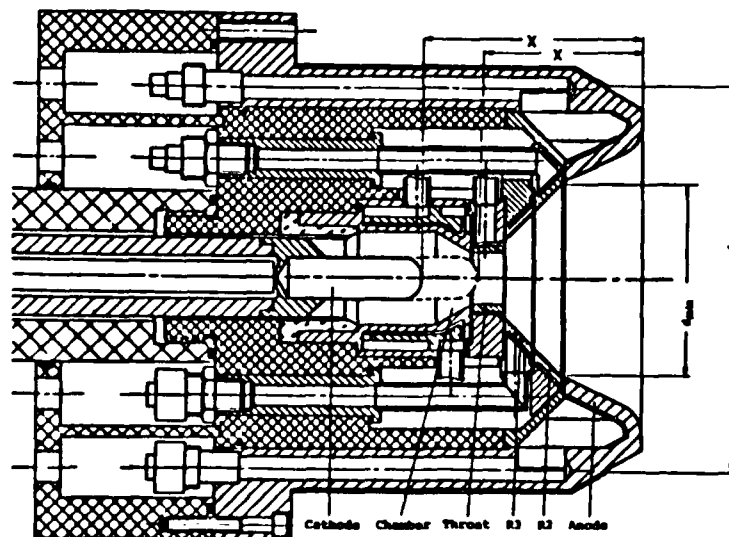


Fig. 2 DT1 thruster head with two different cathode positions.

made of individual water-cooled segments; these are insulated against each other and are electrically floating. The last and largest of the segments represents the anode.

The thruster's dimensions include a throat diameter of 24 mm and an outer anode diameter of 142 mm. All parts of the anode with greater diameter are covered with a ceramic insulation. In this manner the region of the arc's anode attachment is relatively well defined. The propellant is fed mainly through the nozzle chamber, but additional gas can be injected at the anode ring with the DT2 thruster.

The thrusters are operated at currents of up to 6000 A with propellant flows between 0.2 and 1.5 g/s, mainly using argon.

For direct thrust measurements, the thruster is mounted on a thrust balance and placed into a vacuum tank with a length of about 5 m and a diameter of 2 m and which has double, water-cooled walls. The current feed to the balance is achieved through mercury baths. Propellant and cooling water are supplied

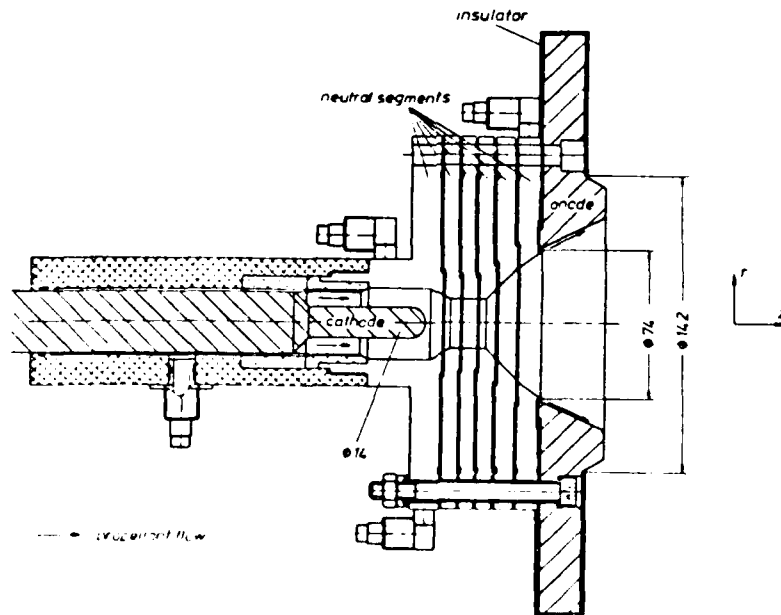


Fig. 3 Nozzle-type MPD thruster DT2 with anode gas injection equipment.

by nylon hoses which form large bows in vertical planes. In order to eliminate errors due to electromagnetic and mechanical interactions, calibration measurements have been performed with the thruster short circuited and with running cooling water. In addition, the thrust balance is remotely calibrated always before and after every test, allowing thrust measurements within an error of less than 2%. The schematic of the thrust stand is shown in Fig. 4. Further, the current discharge voltage, propellant mass throughflow, and thermal losses for each thruster segment and for the electrodes are measured.

The measured dates were recorded by an automatic data acquisition system which is connected to a DEC laboratory computer.

### Experimental results

#### Influence of the ambient pressure on thruster performance (measured with DT1 thruster)

In some recent papers,<sup>6</sup> questions were raised about the validity of test results of continuous self-field MPD thrusters because of the relatively high ambient pressure of about  $5 \cdot 10^{-3}$  to  $5 \cdot 10^{-2}$  mbar in the vacuum systems. These authors referred to measurements which were not made with self-field, but with axial applied-field (MPD-A or Hallarcjet or MAARC) thrusters. This sort of thruster indeed showed a strong influence by the ambient pressure on its performance:<sup>7,8,9</sup> the curve of measured thrust versus vacuum tank pressure showed a declining thrust with increasing pressure in the region between  $10^{-4}$  and  $10^{-1}$  mbar.

But there is no indication anywhere in the literature that any tests of continuous self-field thrusters at tank pressures in the regime reported here ( $\sim 1-2.5 \cdot 10^{-2}$  mbar) have produced erroneous or questionable data. This has been confirmed by measurements in our facility, shown in Fig. 5. With increasing tank pressure, there was initially no measurable change in thruster performance. Only large changes in pressure (by a factor of  $\sim 5$

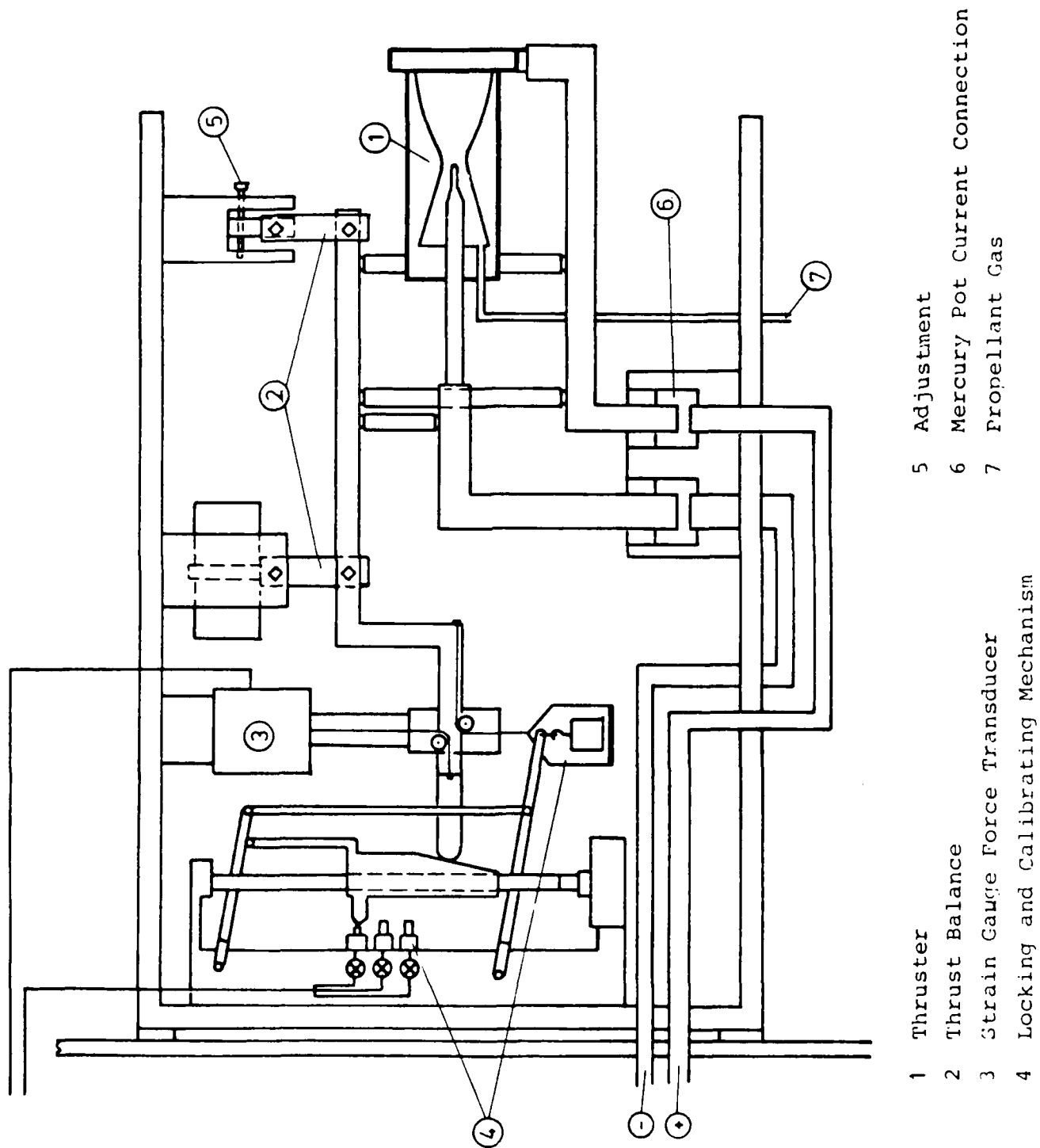


Fig. 4 Thrust balance schematic.

to 10, into the  $10^{-1}$  mbar range) produced some modest deterioration of thrust and increase of voltage. Only at the highest tank pressures of these tests, i.e. around and above  $10^{-1}$  mbar, did the jet plume change its appearance. It became more diffuse, shorter and of larger diameter and the whole thruster face took on a halo of luminous gas. Also, no change in the onset current could be observed.

Calculated and measured pressures at the anode<sup>10</sup> or nozzle exit of our thruster lie in the range of 1 to 3 mbar for typical operating conditions. This pressure is roughly a factor of 100 higher than our tank pressures. Furthermore, since with self-field thrusters magnetic forces are always pointing outwards,

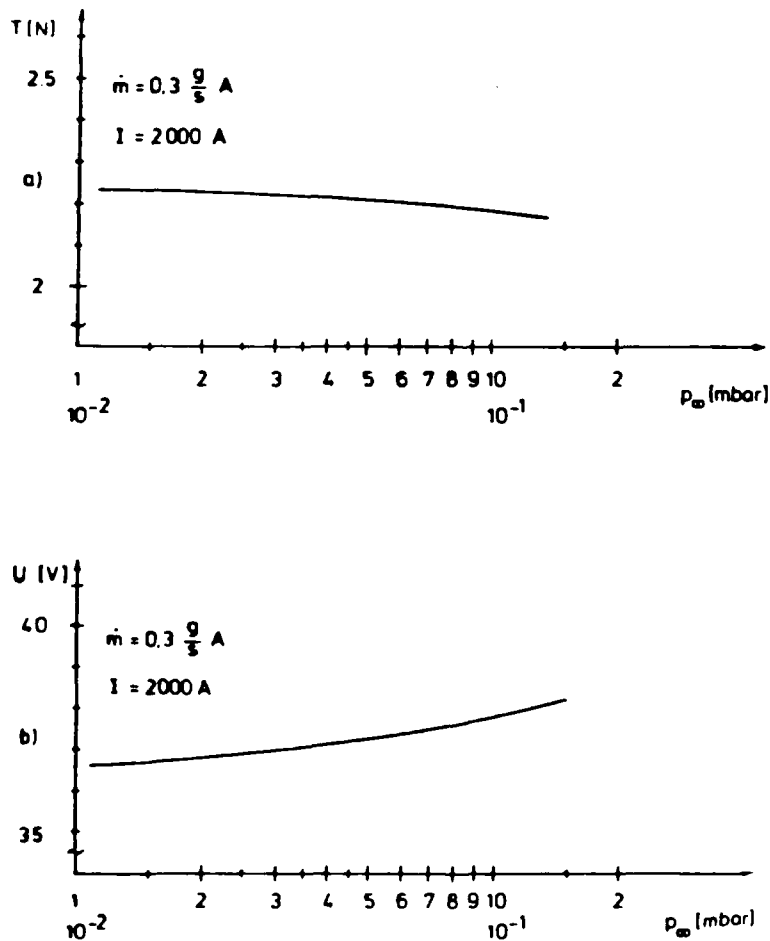


Fig. 5 a) Thrust and b) arc voltage as a function of tank pressure.

there appears to be no possibility that tank gas either gets sucked in or diffuses into that part of the discharge which determines the measured performance. This is particularly valid for steady state thrusters, which are generally operated at higher than the critical mass flow, or at  $I^2/\dot{m}$  well below onset value. Far out in the plume, the tank gas of course mixes with the jet and retards the thruster plasma plume (as Kuriki<sup>11</sup> and others have measured), but this has no influence on the measured performance.

Effect of cathode position (measured with DT1 thruster)

To determine the effect of the cathode position on the thruster performance, several tests with varying cathode positions were made, in the course of which a strong effect on the thrust, the arc voltage and therefore also on the efficiency had been noticed. With the cathode tip closer to the nozzle throat (Fig. 2), a substantial part of the thermal heating of the argon propellant took place in the supersonic part of the nozzle, which reduced the thermal thrust contribution (Fig. 6).

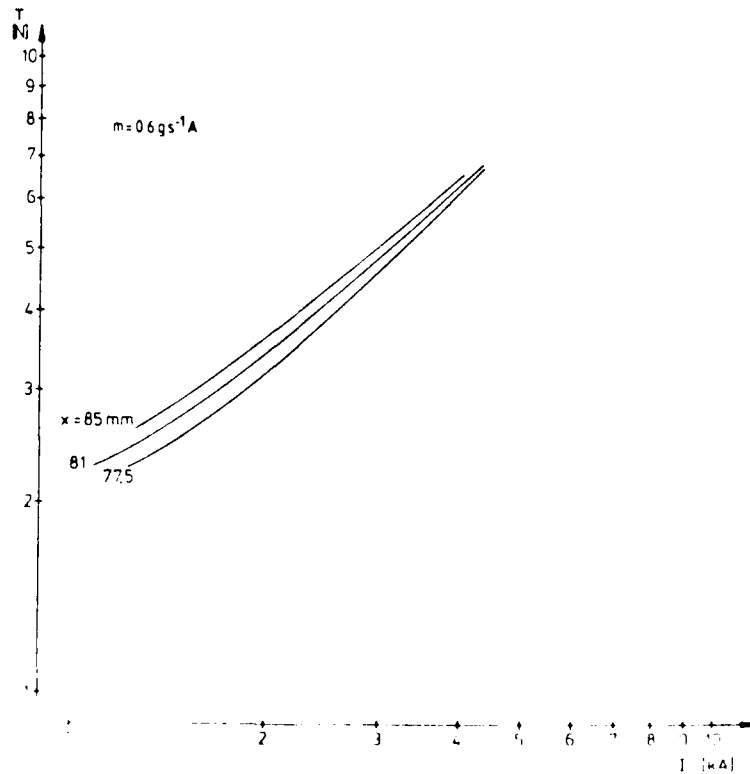


Fig. 6 Thrust as a function of current at different cathode positions.

Because of the shorter current path and therefore minor ohmic voltage drop, the arc voltage became smaller with decreasing electrode distance (Fig. 7). Below onset current, the thrust rises more steeply with increasing electrode distance than the arc voltage, so that the overall efficiency increases (Fig. 8). At currents near the onset point, the electrode distance has no effect on the efficiency, because the slope of the thrust is

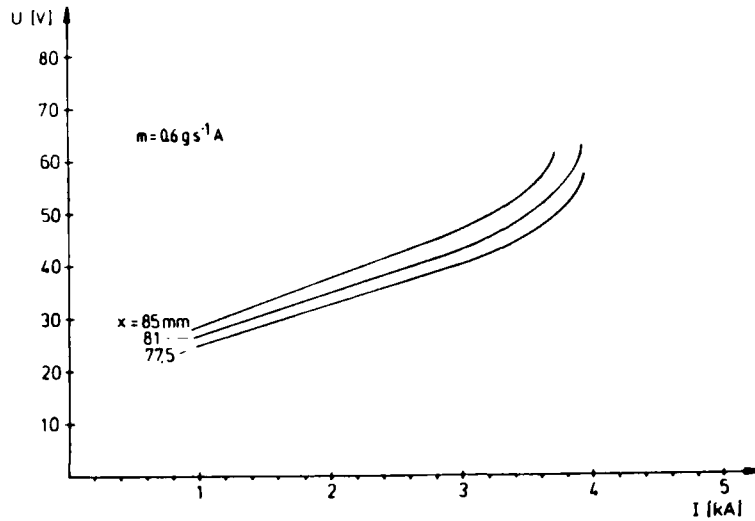


Fig. 7 Arc voltage as a function of current at different cathode positions.

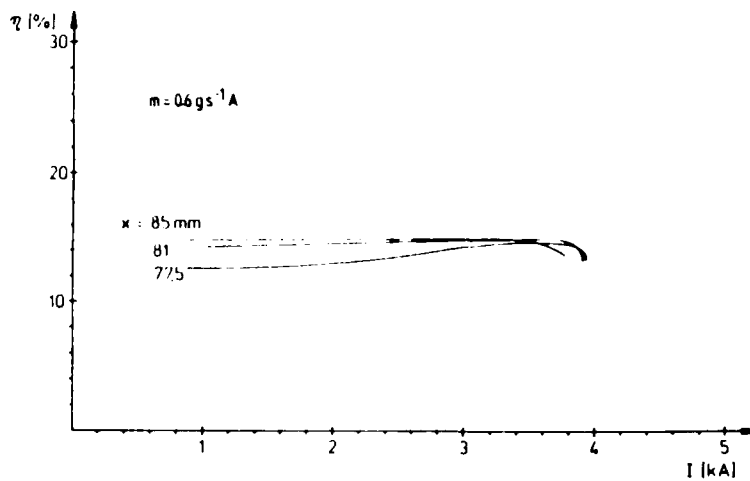


Fig. 8 Thrust efficiency as a function of current at different cathode positions.

compensated by the steeper slope of the voltage. The objections to longer electrode distances are, first, the greater ohmic voltage drop and therefore the possibility of arcing between the neutral segments and, second, the fact that the heat load of the chamber increases with increasing electrode distance (Fig. 9). Considering these facts, for our tests a configuration with the cathode position at  $x = 85$  mm, measured from the anode orifice, was chosen.

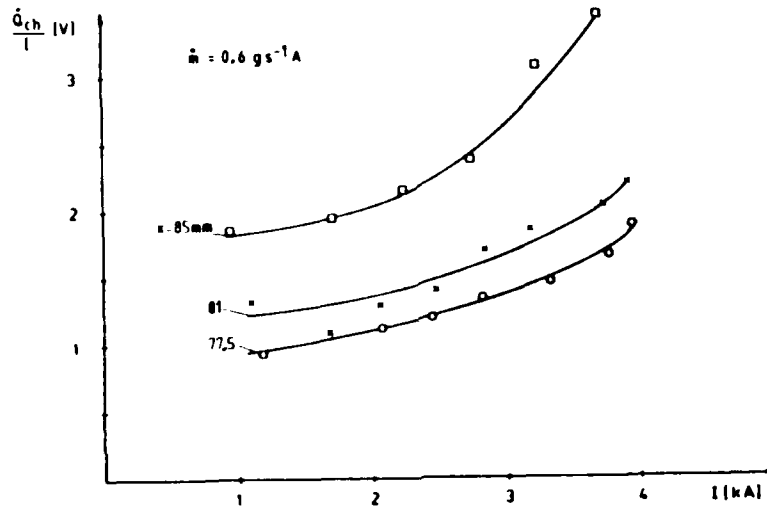


Fig. 9 Chamber loss voltage vs. current at different cathode positions.

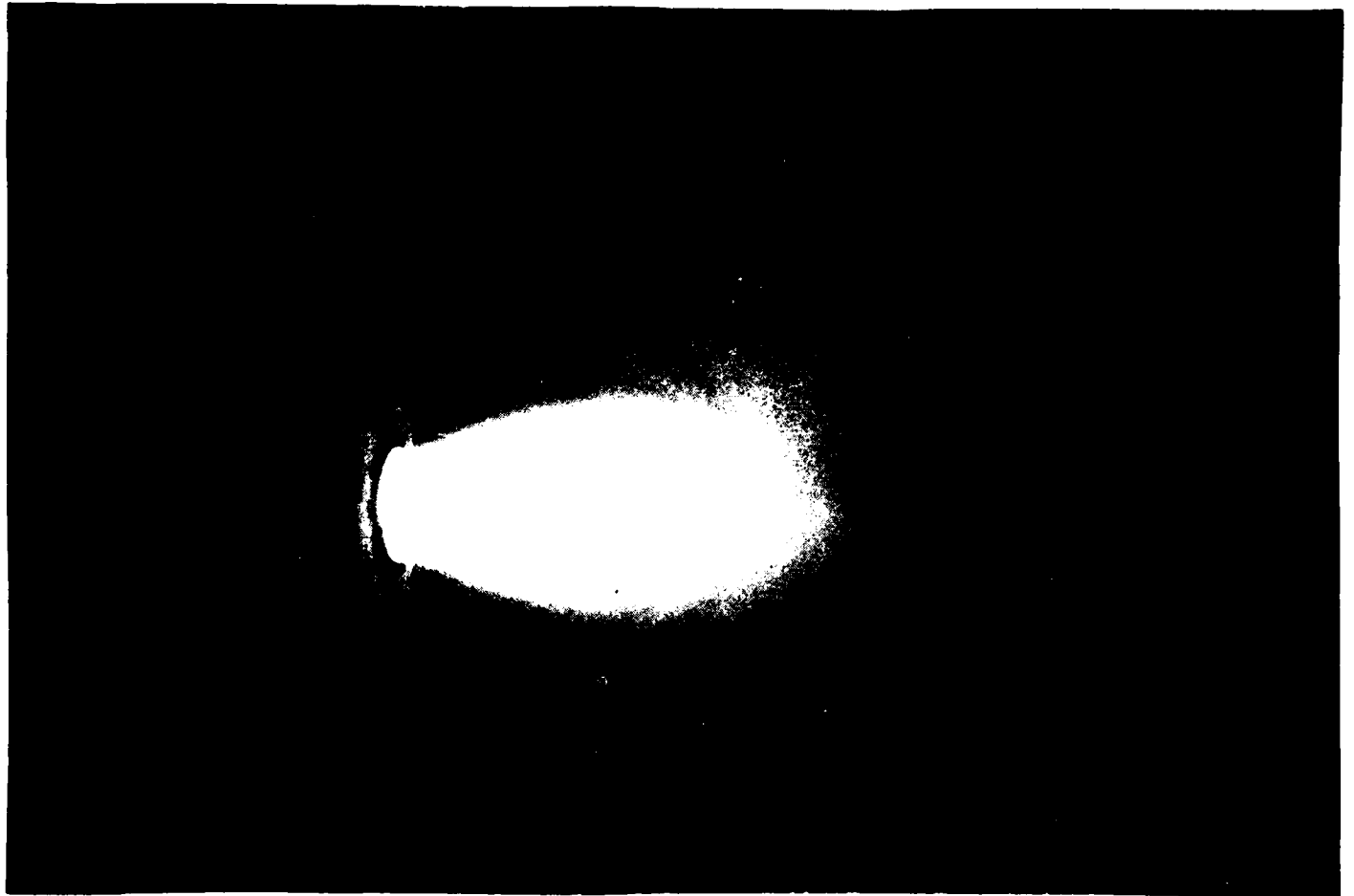


Figure 1. A photograph of a bright, elongated, teardrop-shaped object, possibly a biological specimen or a mineral sample, captured under dramatic lighting.

Performance measurements (with DT1 thruster)

The thrust measurements covered a range from 900-5000 A and are shown in Fig. 11 for several mass flows for argon in a double-log plot. Also plotted in this figure is the electromagnetic thrust, which was calculated with the known thrust formula of Maecker<sup>12</sup>

$$T_m = \frac{\mu_0}{4\pi} I^2 \left( \ln \frac{d_A}{d_C} + \frac{3}{4} \right) \quad (1)$$

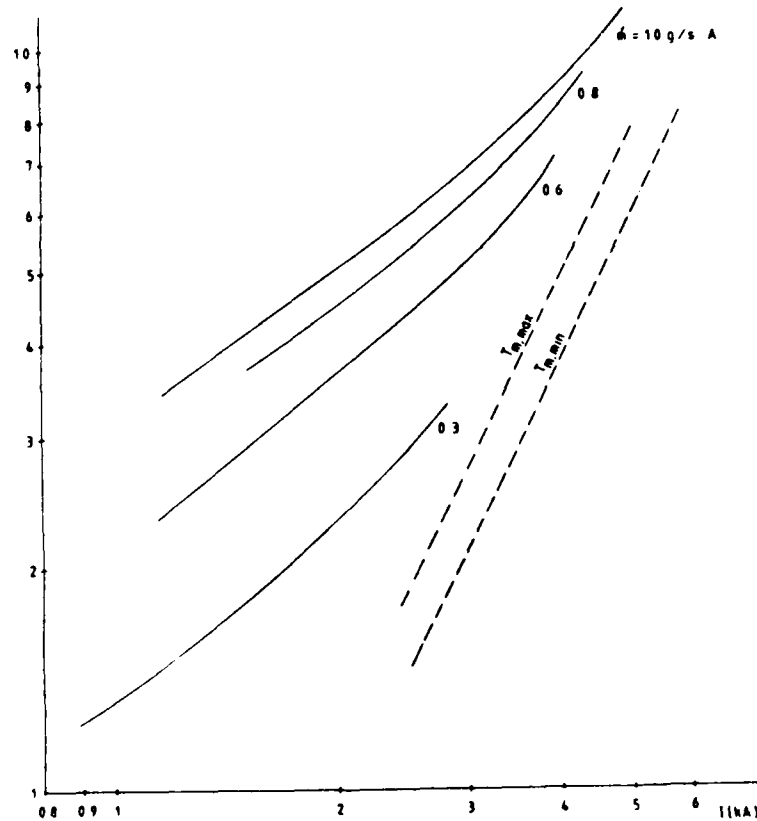


Fig. 11 Directly measured thrust vs. current for several mass flows with argon as propellant.  $T_{m,max}$  and  $T_{m,min}$  are the calculated electromagnetic thrust for maximal and minimal possible anode radius (see Fig. 2).

with  $d_A$  and  $d_C$  as the anode and cathode diameter, respectively. The maximum thrust  $T_{m,max}$  was calculated with the largest possible anode diameter and the minimum thrust  $T_{m,min}$  with the smallest possible  $d_A$  (see Fig. 2). At lower currents, the thrust increases almost linearly with  $I$  and at higher currents attains almost the slope of the  $T_m$  curve. The current and thrust are limited by the onset condition.

Onset is detected visually by the formation of bright hopping spots at the anode. A slight increase in the current at that point leads to a longer attachment of the spots, causing severe melting which destroys the anode. In the experiments, this was avoided.

The specific impulse as a function of the correlation parameter  $I^2/\dot{m}$  is displayed in Fig. 12. It shows almost no dependence on the mass flow and reaches a maximum of about 11,000 m/s at the onset points. The specific impulse is in a wide range almost linear with  $I^2/\dot{m}$  and parallel to a line between  $I_{spm,max}$  and  $I_{spm,min}$ , which means that the thermal part is independent of the correlation parameter.

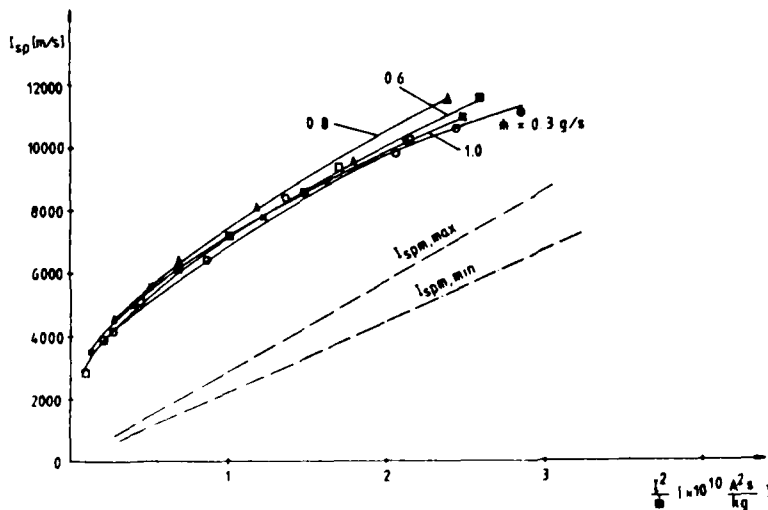


Fig. 12 Specific impulse as a function of the correlation parameter  $I^2/\dot{m}$  for several mass flows with argon as propellant.  $I_{spm,max}$  and  $I_{spm,min}$  are the calculated magnetic impulse for maximal and minimal anode radius (see Fig. 2).

In Fig. 13, the arc voltages are plotted as a function of the discharge current, with the mass flow as parameter. Except near onset, the arc voltages are insensitive to mass flow, and the increase of voltage is nearly linear with the current. The start-up voltage is about 25 to 30 V at 1 kA. The onset voltage of roughly 70 V is nearly the same for all mass flows between 0.3 and 0.8 g/s and in the range of the measurements in Tokyo with the KIII thruster<sup>13</sup> at 0.6 g/s argon.

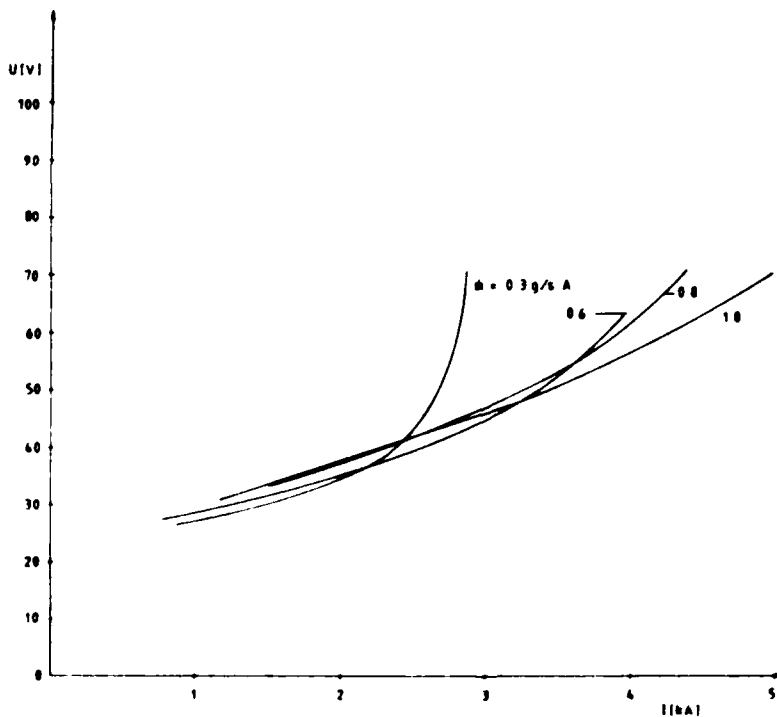


Fig. 13 Arc voltage as a function of discharge current for several mass flows with argon as propellant.

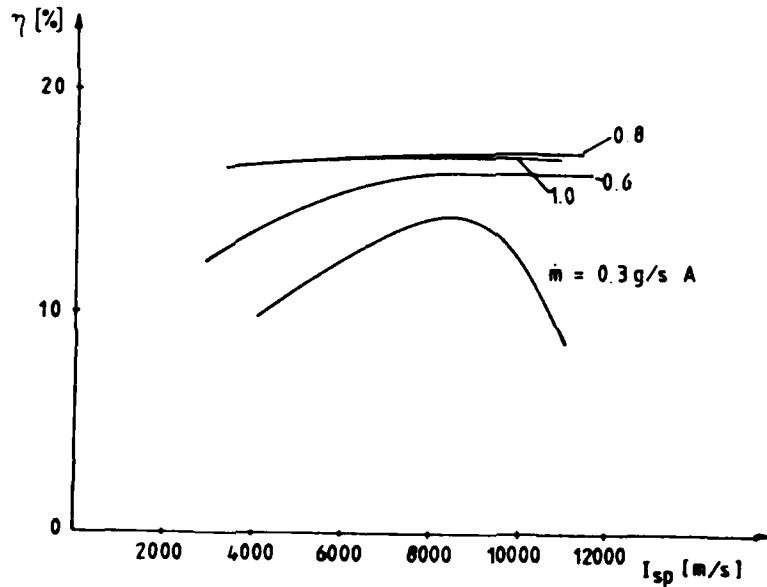


Fig. 14 Thrust efficiency as a function of the specific impulse for several mass flows with argon as propellant.

With the measured data, a thrust efficiency can be calculated as

$$\eta_T = \frac{T^2}{2\dot{m}I \cdot U} \quad (2)$$

This thrust efficiency is displayed as a function of the specific impulse in Fig. 14. Because the Stuttgart thruster works in the predominantly thermal region, the thrust and therefore the efficiency rise with a higher propellant flow.

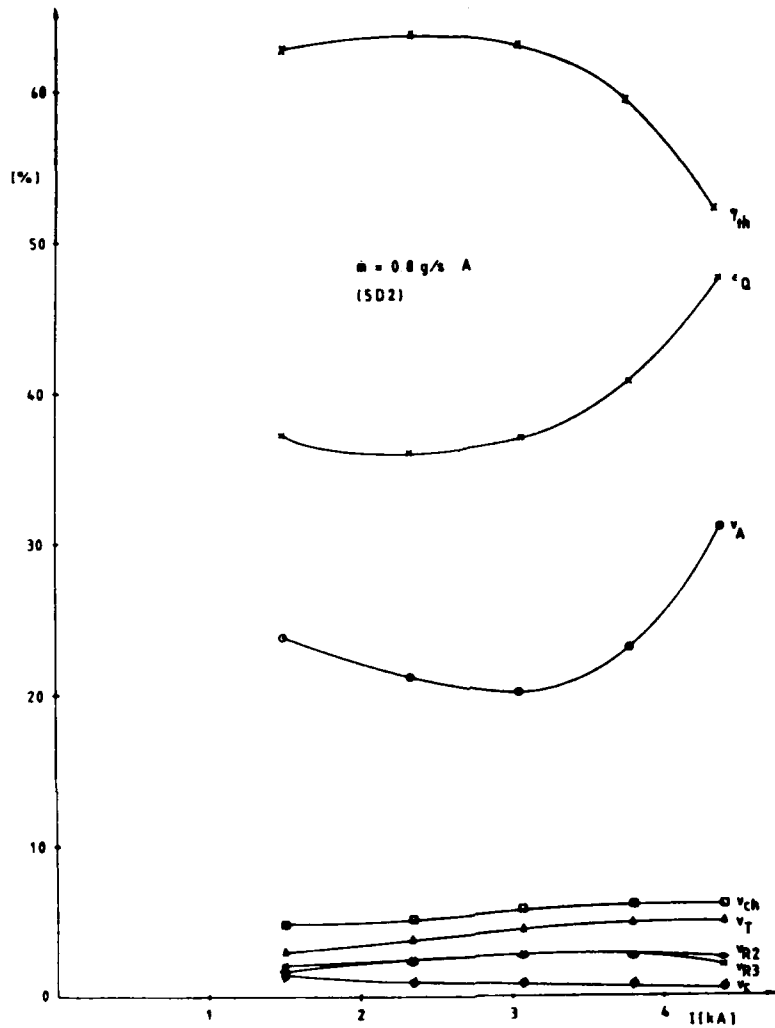


Fig. 15 Loss factors of anode ( $V_A$ ), cathode ( $V_C$ ), neutral segments ( $R_1$ ,  $R_2$ , throat T and chamber ch), sum of loss factors  $\epsilon_Q$  and thermal efficiency  $\eta_{Th}$  as a function of current.

Thermal losses

The heat loss of each neutral segment and of the electrodes was measured separately. Fig. 15 shows the loss factors, defined as heat load per electrical power input times 100, of anode ( $V_A$ ), cathode ( $V_C$ ) and all neutral segments ( $R_2$ ,  $R_3$ , throat and arc chamber).  $\epsilon_Q$  is the sum of all thermal loss factors, and is connected with the thermal efficiency:  $\eta_{Th} = 100 - \epsilon_Q$ ,

which is also plotted in this figure. At low currents, the loss factor of the cathode decreases with increasing current and is almost independent of current near the onset point. The loss factors of the neutral elements show only a small increase with rising current, even near the onset point, which similarly indicates only a small temperature rise of the plasma jet. This means that the severe increasing of the anode loss factor is almost exclusively due to an increasing anode fall voltage  $U_A$ . Neglecting radiation and possible ablation effects, the energy balance of the anode can be expressed as:<sup>10</sup>

$$\frac{\dot{Q}_A}{I} = U_A + \frac{5}{2} \frac{k}{e} T_e + \Phi + U_{\text{conv.}} \quad (3)$$

In order to calculate  $U_A$  from this equation, the anode heat loss  $Q_A$  is measured, the known value for the work function is used, and the convective heat is determined from the measured heat loss of the neutral segment  $R_2$  next to the anode. From investigations by Maisenholder of the electron temperature in the plasma jet<sup>14</sup> for a very similar thruster, we chose an electron temperature near the anode surface of 15,000 K. The anode fall voltage  $U_A$  is shown in Fig. 16, which is in accordance with the theoretical thoughts on anodes by Hugel.<sup>10</sup> The steep rise of

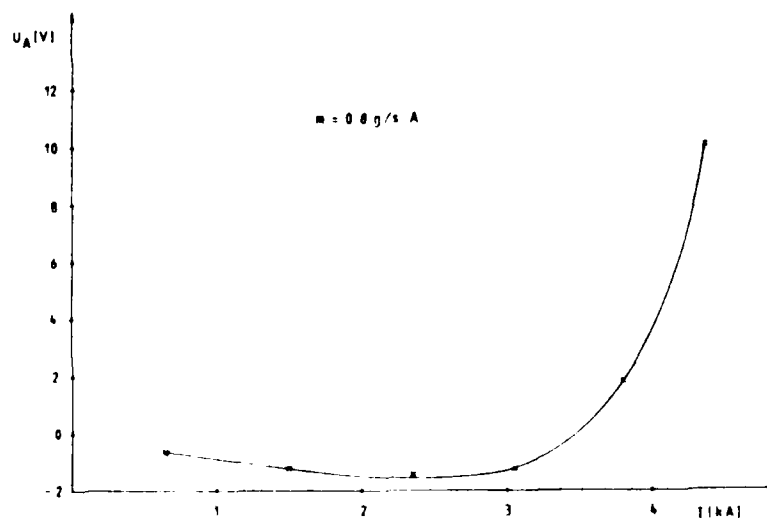


Fig. 16 Calculated anode fall voltage as a function of discharge current for 0.8 g/s argon as propellant.

the anode fall voltage near the onset point, with almost unchanged temperature in the arc jet, points to a changed anode mechanism at onset, which could also be detected visually during our experiments.

In Fig. 17, the anode loss voltage, defined as  $\dot{Q}_{\text{anode}}/I$ , is shown for different mass flows versus the correlation parameter  $I^2/\dot{m}$ . Again the steep rise of the anode losses near the onset point, which is independent of the mass flow, should be noted.

The thermal efficiency  $\eta_{\text{Th}}$  (Fig. 15) of this thruster is about 60% and decreases near the onset point because of increasing anode fall voltage, as discussed before.

#### Anode gas injection (with DT2 thruster)

The increase in the anode fall voltage near onset suggests that this phenomenon is at least partly an anode problem. Baksht<sup>15</sup> and Hgel<sup>10</sup> built their onset theories thereon as an anode starvation process. This theory and experiments at Princeton<sup>16</sup> suggest that gas injection near the anode would increase the critical  $I^2/\dot{m}$  to higher values. The anode gas is injected at the beginning of the anode, tangential to the anode surface.

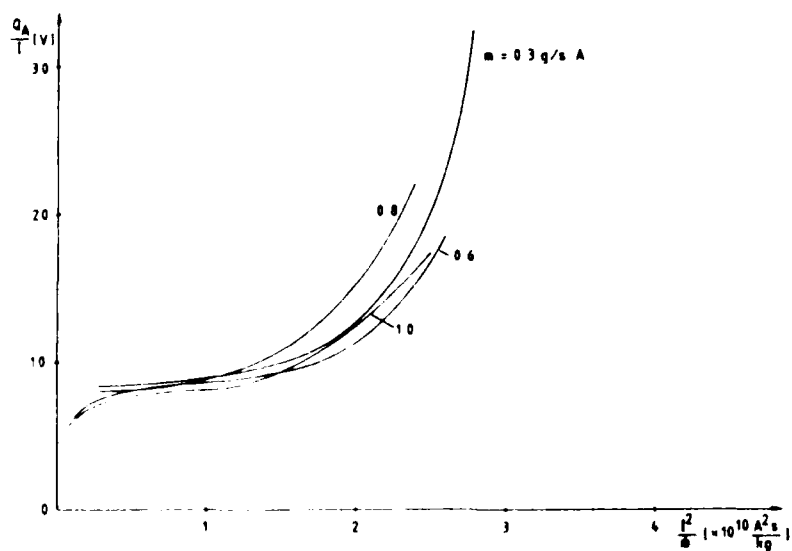


Fig. 17 Anode loss voltage as a function of the correlation parameter  $I^2/\dot{m}$  for several mass flows with argon as propellant.

In Figs. 18 and 19 the results of these experiments with an anode gas fraction between 0 and 20% of the total propellant flow of 0.8 g/s argon are displayed: the critical  $I^2/\dot{m}$  is indeed raised from  $2.45 \cdot 10^{10}$  to  $3.0 \cdot 10^{10}$  A<sup>2</sup>s/kg. An anode fall

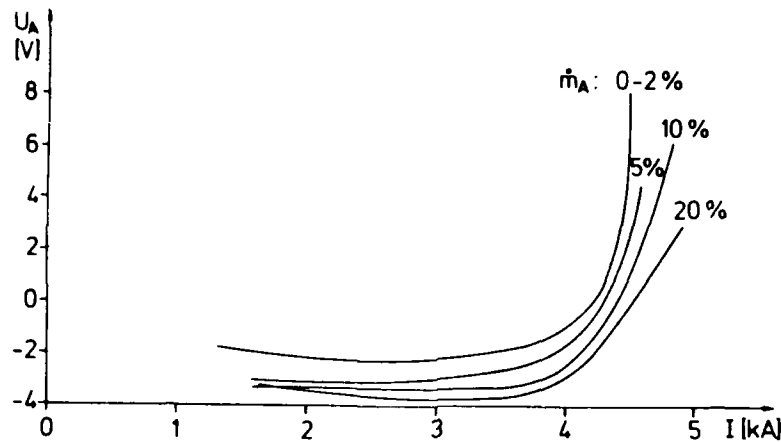


Fig. 18 Calculated anode fall voltage vs. discharge current with different portions of anode gas for a total mass flow of 0.8 g/s argon.

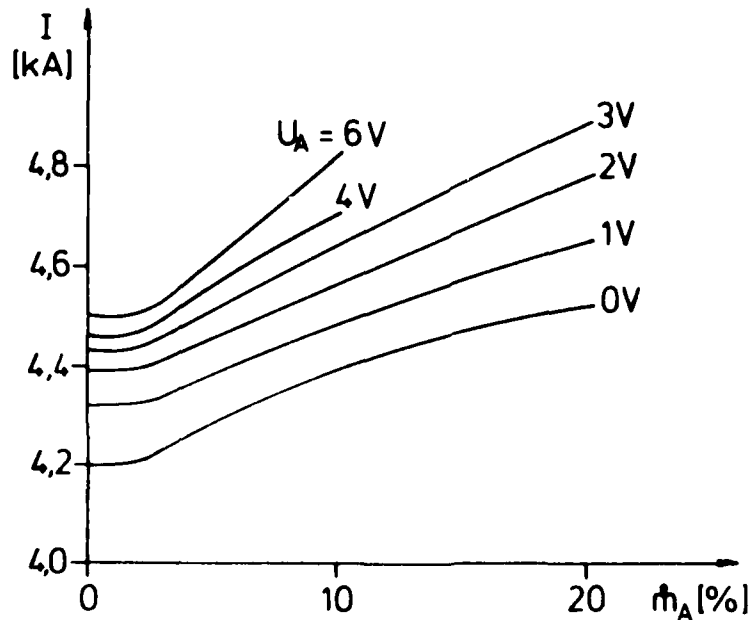


Fig. 19 Current at which a certain anode loss voltage is reached (Fig. 18) vs. anode mass flow with the anode fall voltage as parameter.

voltage of 3 V was taken for defining onset in the continuously running MPD thruster (see Fig. 18).

In order to justify this, the current, at which a certain anode loss voltage is reached, is plotted versus the injected anode mass fraction with the anode fall voltage as parameter (see Fig. 19).

The onset rises steadily with the anode gas fraction. The arc voltage (Fig. 20) is almost the same at lower currents, with somewhat lower values for the higher anode gas fractions. At higher currents, the voltage curves spread, in accordance with the higher anode fall voltages. This increase of the onset current must concede to worse thrust values at higher anode gas fractions (Fig. 21).

To overcome this handicap, experiments were carried out with the lighter hydrogen and nitrogen as anode gas, where the masses were chosen so that the particle number was the same as with argon anode gas. Contrary to the expectations of the anode starvation theories, these anode gases changed neither the voltage nor the onset behavior, and showed results similar to those in

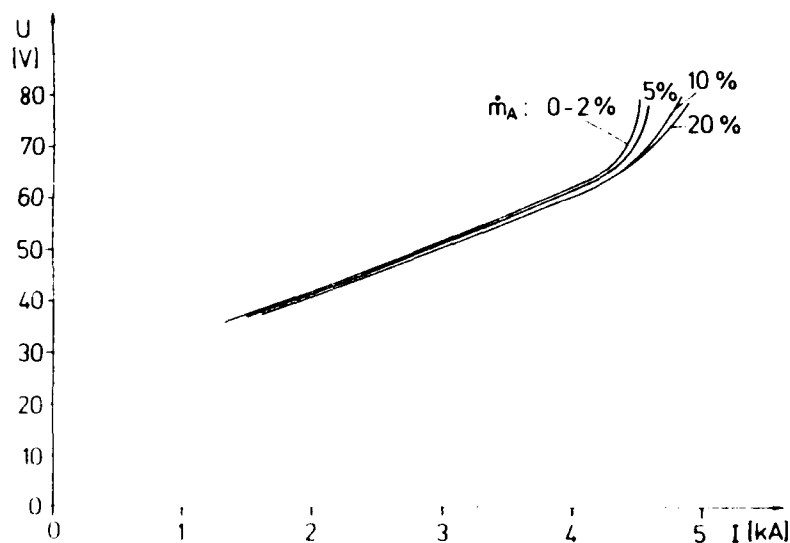


Fig. 20 Arc voltage vs. discharge current with different portions of anode gas for a total mass flow of 0.8 g/s argon.

experiments without any anode gas injection. This phenomenon can only then be explained by Hgel's theory if the injected anode gases are not ionized at all. This requires a very low ionization rate coefficient of the injected gases.

In Figs. 22 through 25 the voltage current characteristics are drawn in a double logarithmic manner for argon as main (cathode) propellant and with different elements as anode gas. The total mass flow in each case is 0.8 g/s. The curves all show a similar behavior--they rise linearly to a certain point of about 4.1 kA, then change abruptly to a steeper, also constant, slope.

The first part up to the angle point, which indicates fully ionized plasma, is practically identical and is independent of the anode gas fraction. The second, steeper part of the voltage characteristics depend on the anode gas--the more anode gas, the less steep is the slope. An explanation may be that the injected cold gas must be ionized and so the voltage rise is smaller than

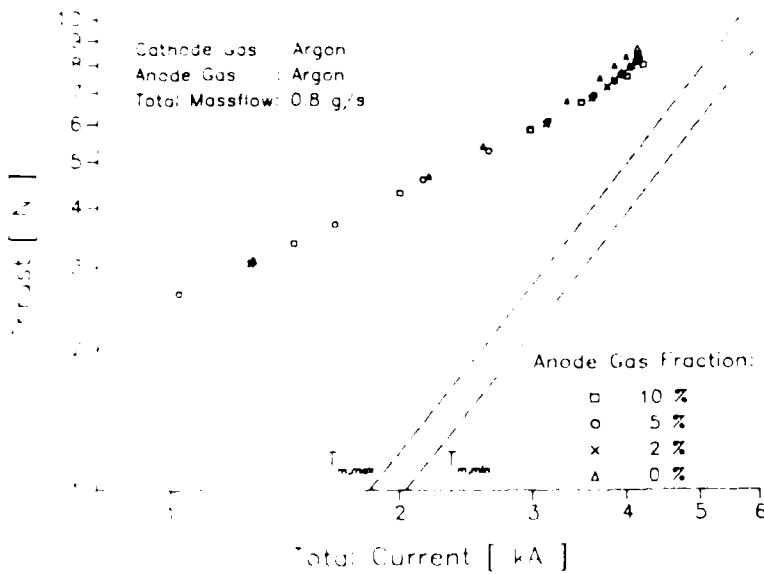


Fig. 21 Thrust vs. discharge current with different portions of anode gas, for a total mass flow of 0.8 g/s argon.

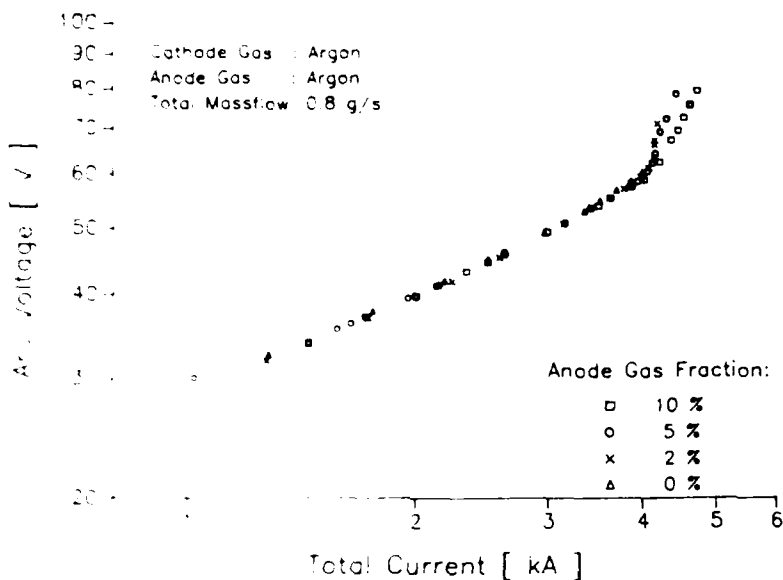


Fig. 22 Arc voltage vs. discharge current with different portions of argon anode gas, for a total mass flow of 0.8 g/s argon.

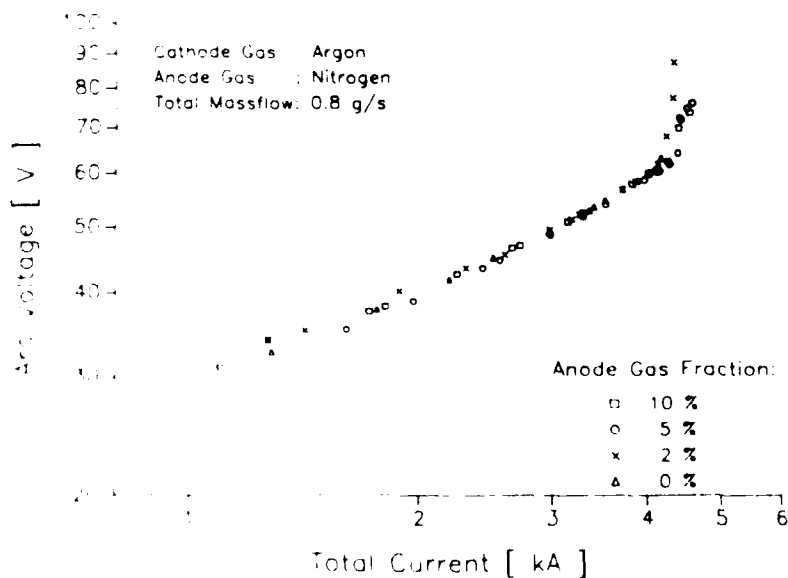


Fig. 23 Arc voltage vs. discharge current with different portions of nitrogen anode gas, for a total mass flow of 0.8 g/s.

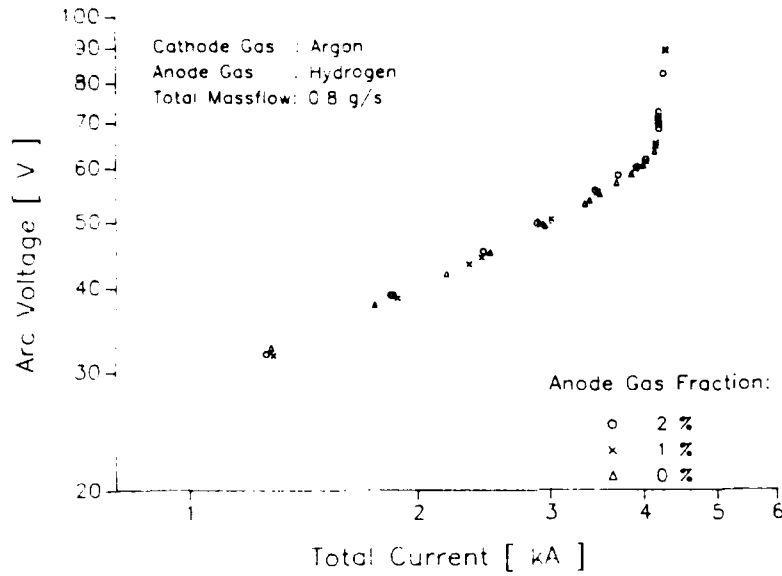


Fig. 24 Arc voltage vs. discharge current with different portions of hydrogen anode gas, for a total mass flow of 0.8 g/s.

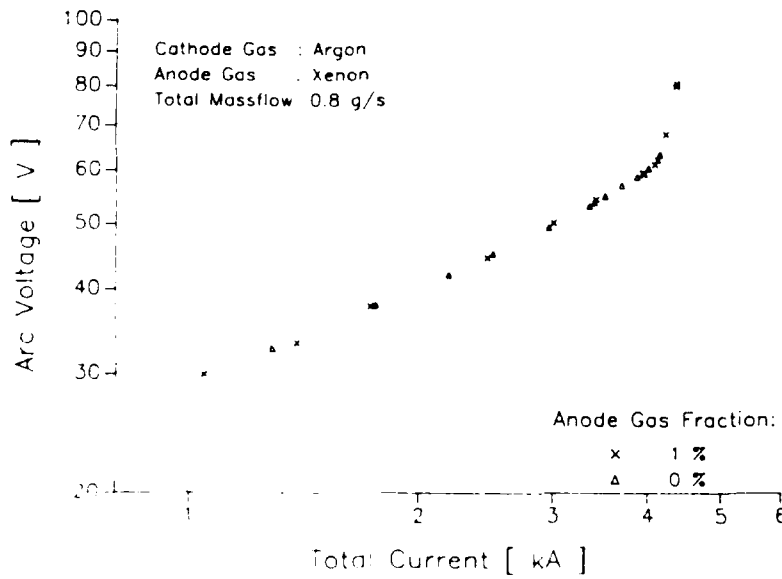


Fig. 25 Arc voltage vs. discharge current with xenon anode gas, for a total mass flow of 0.8 g/s.

without ionization. In contrast to this fact, with smaller atomic masses (that means higher particle numbers must be ionized at constant mass flow) the slope becomes steeper. This eventually can be attributed to the better heat conduction with gases of low atomic mass.

Without anode gas, the onset was observed visually, as described above, by detecting arc attachment spots at the anode. With anode gas injection, the rise of the anode fall voltage is driven to higher currents and the onset is split: before the appearance of the anode spots, the discharge begins to oscillate with a frequency of about 220 kHz. With a further rise in the current, the frequency rises and becomes more stochastic. For example, with a 5% N<sub>2</sub> anode gas fraction:

Begin of oscillations: I = 4350 A, f = 222 kHz  
at I = 4540 A, f = 267 kHz  
and I = 4700 A, f = 310 kHz.

In Fig. 26 an oscillogram of such an instability is shown, taken with a 20 MHz sample rate transient recorder from signals of a floating potential probe in the plasma. This split of the onset (with the pulsed thrusters there even exists another onset point, namely the angle point of the voltage current characteristic as shown in section III) indicates that the onset is not only an anode phenomenon, but also a stability problem, as explained by a theory of Schrade at the IRS.<sup>1'</sup> The beginning of the oscillation is a function of the anode gas fraction as shown for the case Ar/Ar (cathode gas/anode gas),  $m_{tot} = 0.8$  g/s:

100/ 0	4020 A
98/ 2	4090 A
95/ 5	4180 A
90/10	4230 A.

Unfortunately, no performance measurements in the unstable region could be obtained, because the thrust and thermocouple measurements are disturbed by these oscillations, and a remedy has not yet been found.

### Nitrogen Propellant

First experiments with molecular gases were carried out, and the propellant chosen was nitrogen. In Figs. 27 to 32 results are compared with those of argon with the same volume flow, e.g. 0.56 g/s N<sub>2</sub> to 0.8 g/s Ar, first without and second with 10% anode gas.

In Figs. 27 and 28 the voltage/current characteristic and the thrust are shown with no anode gas. The discharge voltage for N<sub>2</sub> is higher roughly by a factor of 1.25. In Refs. 10 and 18 it is shown that the onset occurs at constant values of  $I^2 \cdot \sqrt{M/\dot{m}} = \text{const}$ , with M as the molecular or atomic mass. If M = 28 is taken as the molecular mass for nitrogen and the incidence of the above mentioned oscillations as the onset point, this fits quite well with  $1.3 \cdot 10^{11}$  A<sup>2</sup>s/kg for Ar and  $1.1 \cdot 10^{11}$  A<sup>2</sup>s/kg for N<sub>2</sub>.

For lower currents, the thrust with nitrogen is approximately 30% smaller than with argon. This can be explained by the minor thermal thrust fraction, which depends on the smaller absolute

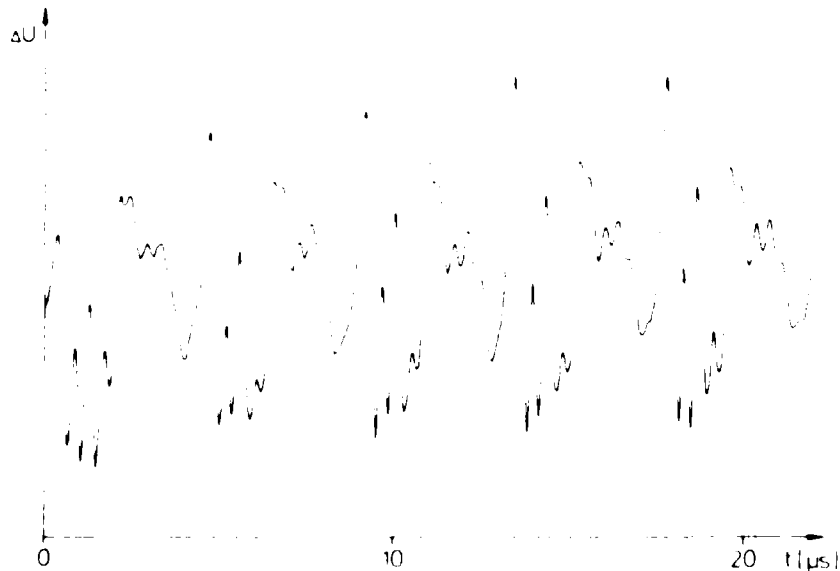


Fig. 26 Periodic oscillations of 230 kHz main frequency occurring after "onset" condition.

$I = 4300$  A,  $U = 72$  V,  $\dot{m}_C = 0.72$  g/s Ar,  $\dot{m}_A = 0.08$  g/s N<sub>2</sub>.

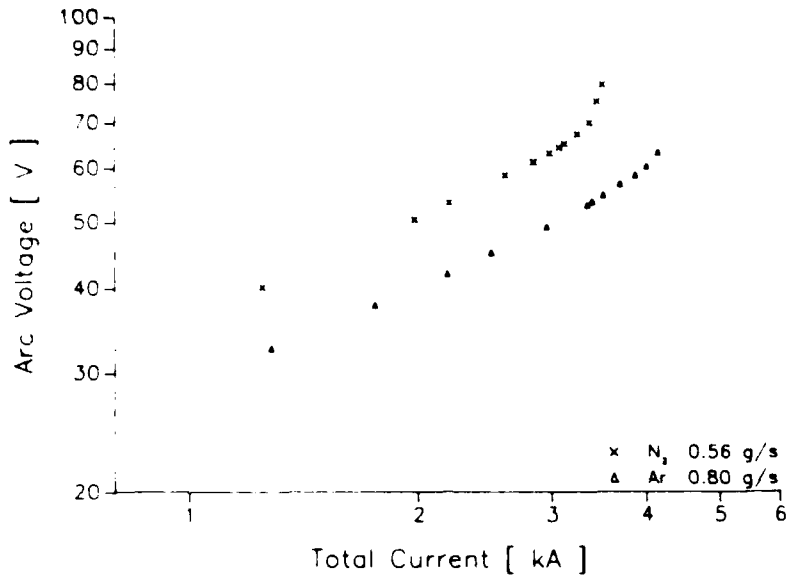


Fig. 27 Arc voltage vs. discharge current for an equal volume flow of argon (0,8 g/s) and nitrogen (0.56 g/s) without anode gas.

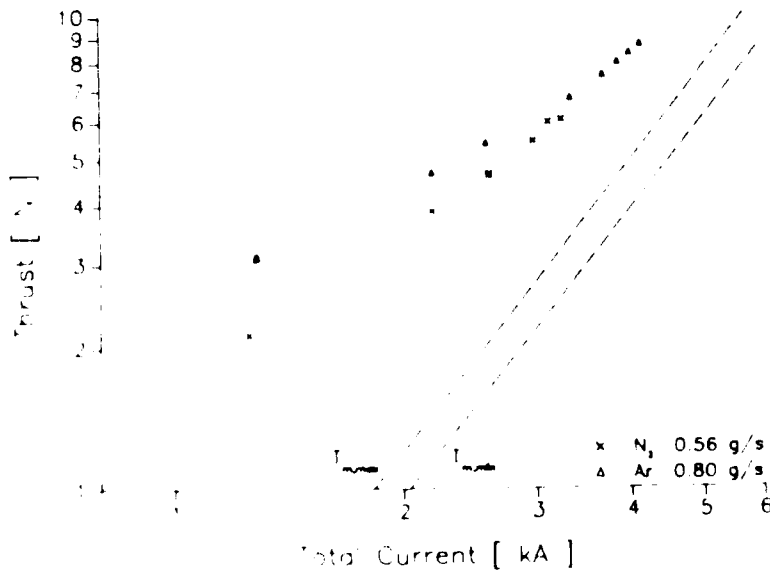


Fig. 28 Measured thrust vs. current for an equal volume flow of argon (0,8 g/s) and nitrogen (0.56 g/s) without anode gas.  $T_{m,max}$  and  $T_{m,min}$  are the calculated electromagnetic thrust for the maximal and minimal possible anode radii.

mass flow. With higher discharge currents, the thrust values approach each other. The efficiencies, shown in Fig. 29, are plotted against the specific impulse. The lower efficiencies of  $N_2$  are due to the higher voltage, and the decline with higher  $I_{sp}$  corresponds to the steep rise of the voltage near onset.

With anode gas, the results are in general similar, as demonstrated in Figs. 30 to 32. Again the shifting of the onset to higher current values can be observed, where it is interesting to note that the slope after the angle point with  $N_2/N_2$  is remarkably smaller than with  $Ar/Ar$  or with the combination  $Ar/N_2$  in Fig. 23.

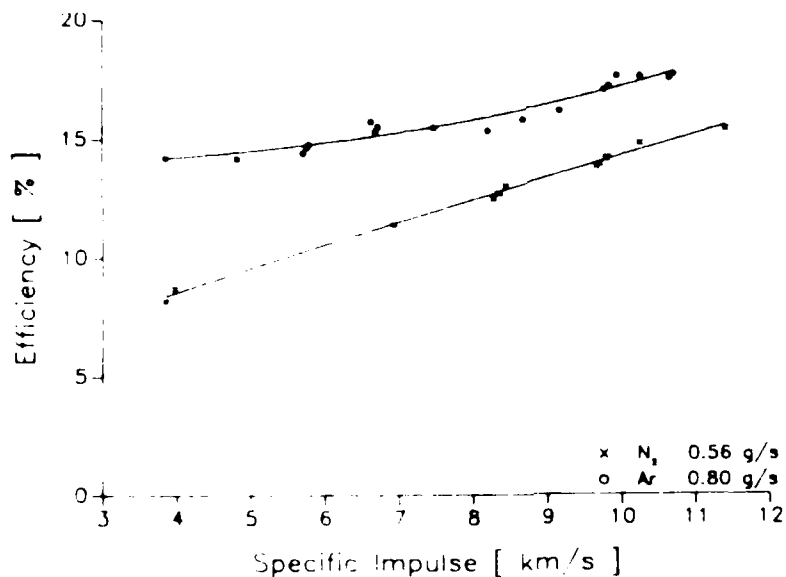


Fig. 29 Thrust efficiency as a function of the specific impulse for an equal volume flow of argon (0.8 g/s) and nitrogen (0.56 g/s) as propellant, without anode gas.

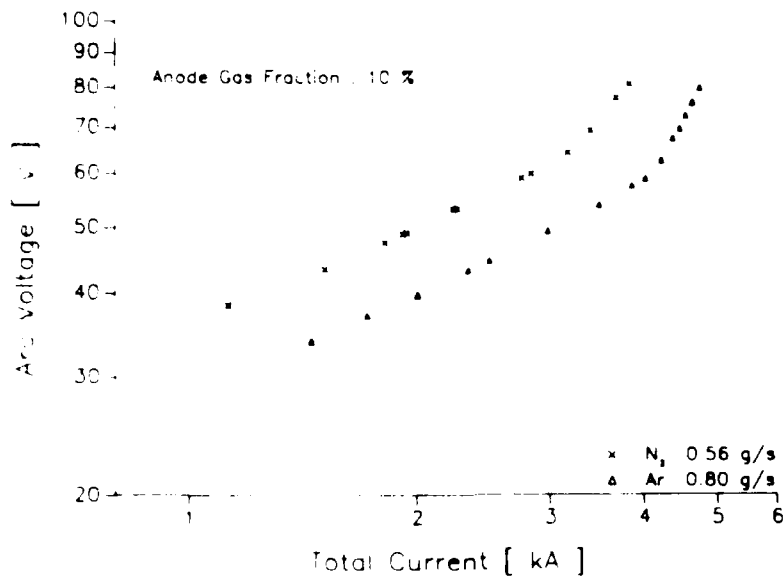


Fig. 30 Arc voltage vs. discharge current for an equal volume flow of argon (0,8 g/s) and nitrogen (0.56 g/s) with an anode gas mass fraction of 10%.

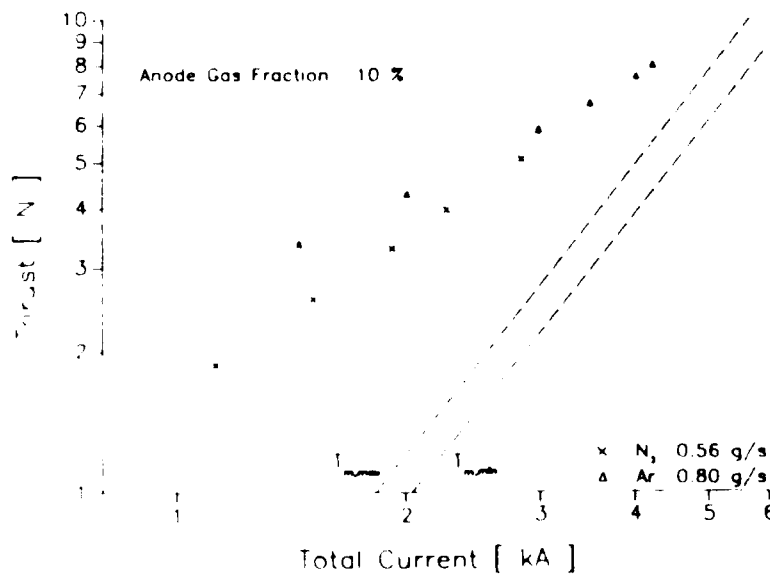


Fig. 31 Measured thrust vs. current for an equal volume flow of argon (0.8 g/s) and nitrogen (0.56 g/s) with an anode gas mass fraction of 10%. T<sub>m,max</sub> and T<sub>m,min</sub> are the calculated electromagnetic thrust for the maximal and minimal possible anode radii.

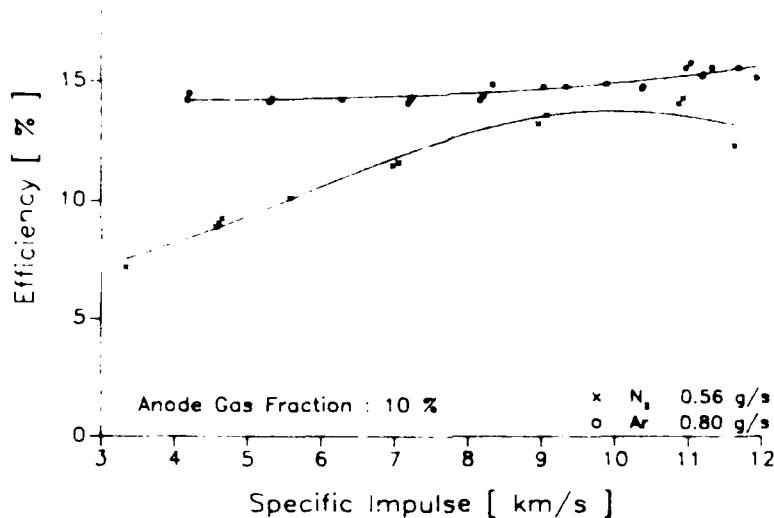


Fig. 32 Thrust efficiency as a function of the specific impulse for an equal volume flow of argon (0.8 g/s) and nitrogen (0.56 g/s) as propellant, with an anode gas mass fraction of 10%.

## 2.2 Cylindrical MPD Thruster with Elongated Electrodes

In contrast to the nozzle-type MPD thrusters, which are in effect hybrids of pure MPD and thermal arcjets, cylindrical thrusters are predominantly MPD devices. Further, the elongated electrodes are hoped to reduce the pinch effect found to be an essential factor affecting the anode mass starvation, according to the calculations of Hügel<sup>16</sup> and the Princeton experiments.<sup>17</sup> These cathodes will be mostly radiation-cooled and may be more limited in current-carrying capability. The thruster has been designed based on available information from previous experiments (including Princeton data) and calculations for maximum I<sub>sp</sub> and specific impulse. In this first version of a continuously running cylindrical thruster with a long cathode, the anode and all neutral segments will be water-cooled (Fig. 33). A second, non-cooled version with the same electrodes will be built and tested in a quasi-steady mode, in the same way as described below for the nozzle-type thruster.

It is not yet evident whether the full length cathode will operate smoothly in a steady-state mode. Therefore, the cathode is being built as a displaceable one, where the discharge will be ignited in a retracted position. When the cathode tip begins to glow, the cathode will be protruded to the foreseen position.

The anode is divided into three parts to give some insight into the current density distribution on the anode and to compare it with the theoretically evaluated values.

Since the anode rings can be switched separately, this thruster with displaceable cathode will allow a wide range of geometric variations to be tested. Experiments at Princeton<sup>20</sup> showed strong dependencies of the onset  $I^2/\dot{m}$  values on the place where the propellant was fed. With this thruster design, therefore, two propellant ports are anticipated in a slit around the cathode and in a slit at the anode radius, both at the backplate. A variation of the propellant fractions at these ports should show whether the observed onset variations with quasi-steady pulsed configurations can be reproduced with a steady-state device.

In Figs. 34 and 35 first results of the influence of the cathode position variation on the current distribution are shown. The propellant flow was a total of 2 g/s argon, divided 3:1 respectively between the cathode and the outer (anode) injection

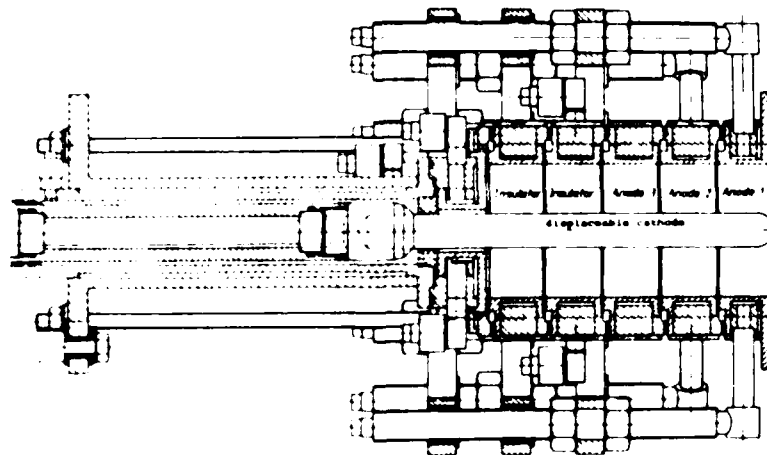


Fig. 33 Cylindrical MPD thruster head schematic.

port. In both cases, the arc was ignited at a position of ca. -5 mm (0 = backplate) with about 1200 A; the cathode was shifted to ca. +5 mm and there the current was increased to the planned current level, 2000 and 3000 A. Then the cathode was fed by motor with a velocity of  $\approx 1$  mm/s downwards. Both cases show similar behavior--first the rearmost anode ring took almost all the current, the middle and front ring only very little. When the cathode tip reached the region of the rear anode ring, the anode current distribution changed dramatically--the main current part switched from the back ring to the front ring, while the middle anode ring was almost passed over. Both tests had to be stopped when the cathode tip reached the beginning of the first anode ring ca. 30 mm behind the front plate, and relatively weak anode attachment spots occurred at the outer edge of anode ring 1. The voltage first decreased slightly with the protruding of the cathode and remained then practically constant. With the lower current (2000 A) at 15 mm a rearrangement of the discharge was observed, accompanied by a voltage increase. During ignition, some backward flashing of the arc into the chamber in front of the throat occurred, which caused some damage. As these first experiments should only verify the working of a continuously running cylindrical MPD arc, no thrust was measured.

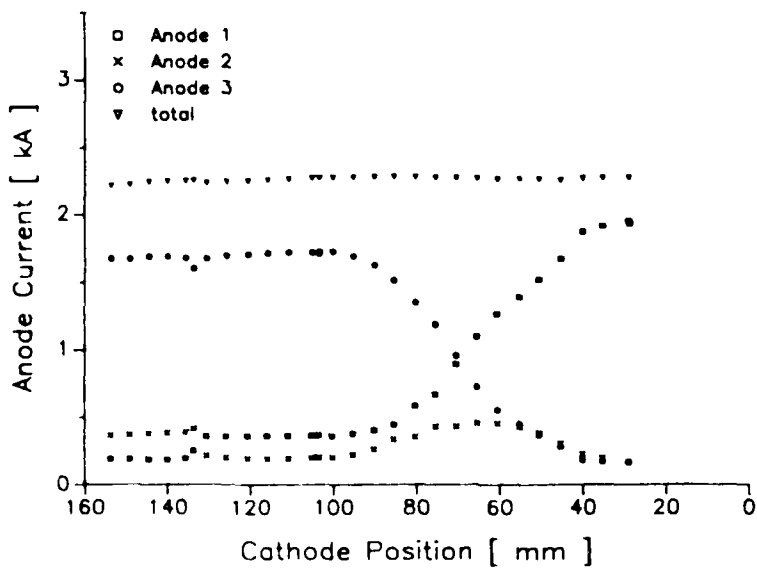
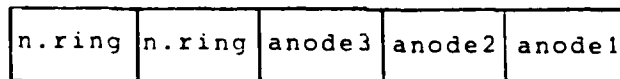
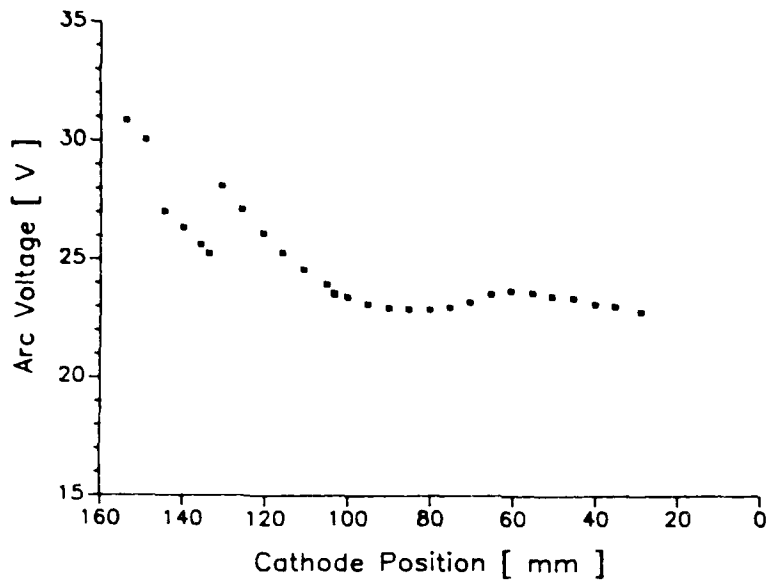


Fig. 34 The a) voltage and b) anode current portions as a function of the cathode tip position for the cylindrical MPD thruster, with 2.0 g/s argon propellant divided 3:1 between cathode and anode injection ports. Discharge current 2000 A.

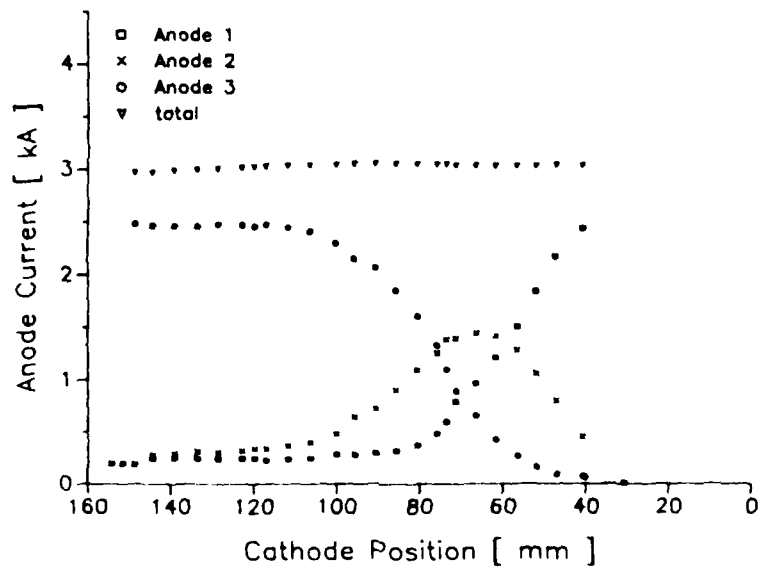
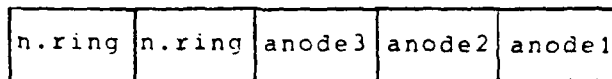
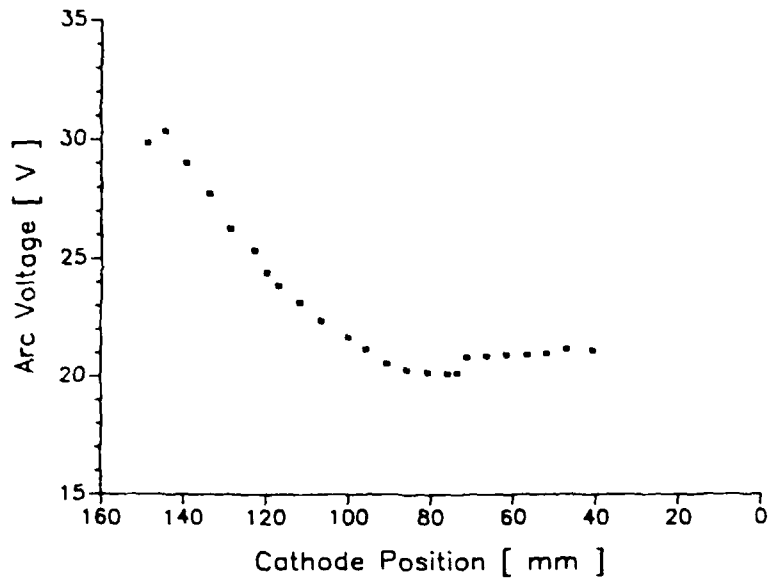


Fig. 35 The a) voltage and b) anode current portions as a function of the cathode tip position for the cylindrical MPD thruster, with 2.0 g/s argon propellant divided 3:1 between cathode and anode injection ports. Discharge current 3000 A.

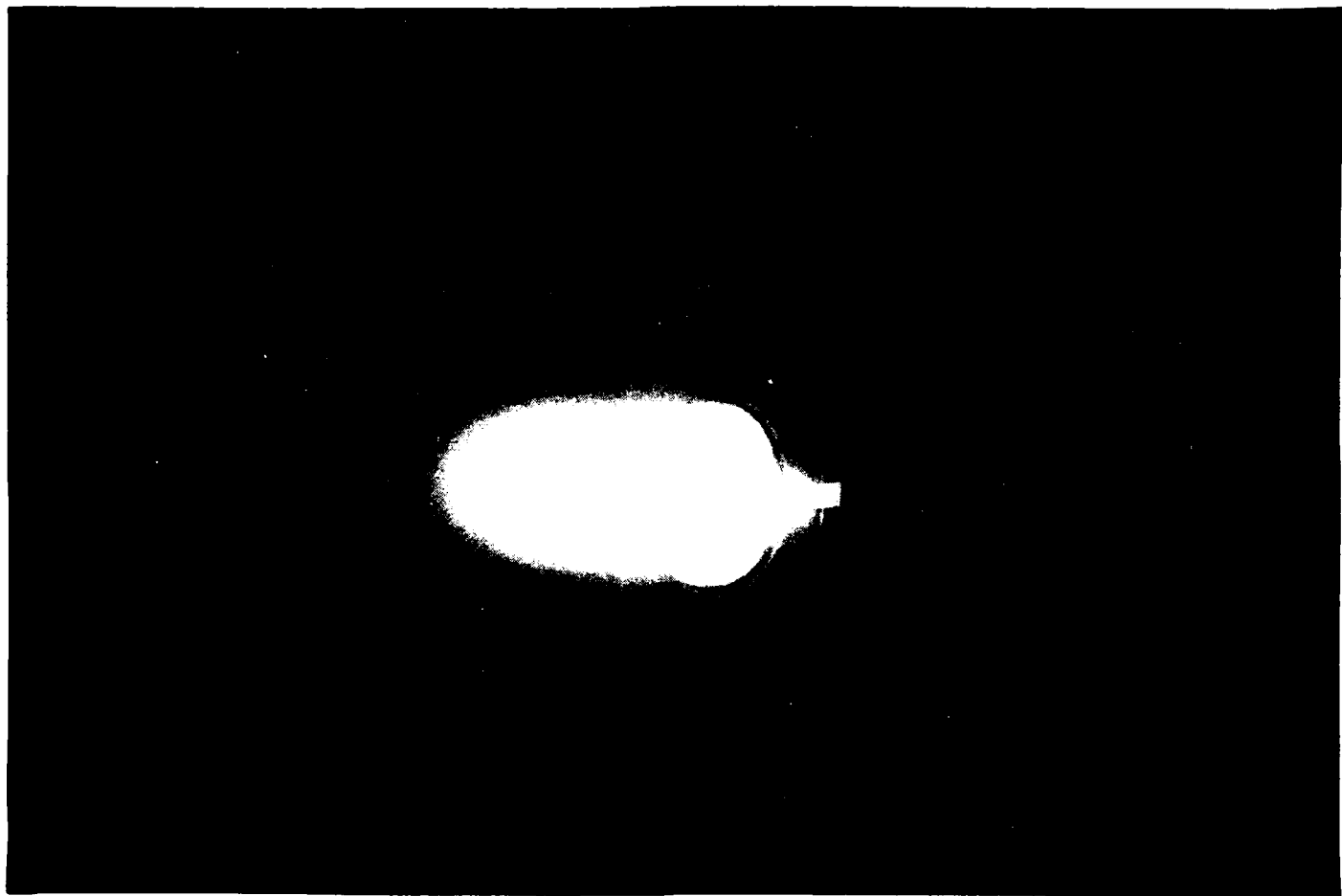


Fig. 36 Jet plume of cylindrical MPD thruster in air.  
 $I = 3000 \text{ A}$ ,  $m_c = 1.5 \text{ g/s Ar}$ ,  $\dot{m}_a = 0.5 \text{ g/s air}$

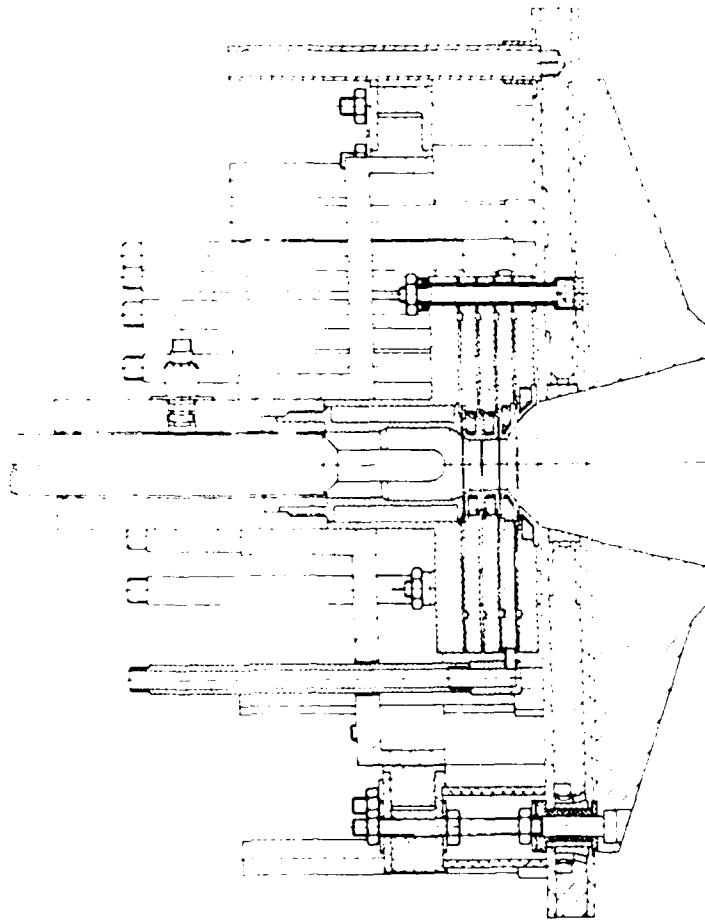


Fig. 37 Nozzle-type MPD thruster with radiation-cooled tungsten anode (HAT).

### 2.3 Hot Anode Thruster

A substantial part ( $\approx 30\%$ ) of the input power of an MPD thruster is consumed in the anode. Thus, a decrease in these anode losses would heighten the performance of these devices.

MPD thrusters with radiation-cooled anodes show higher thermal efficiencies than those with water-cooled ones, but they were used only with thrusters of a much lower power level and mainly of the applied magnetic field type.<sup>6, 21</sup>

The "Hot Anode Thruster" (HAT) is an attempt to use these advantages of radiation-cooled anodes for thrusters in the power

class of 200 kW. Its schematic is shown in Fig. 37. In order to provide a sufficiently large area to radiate the anode input power, the anode flange has a diameter of roughly 40 cm. It is made out of tungsten; the areas not intended to be loaded by the current are covered by tantalum carbide, which is a relatively weak insulator. This coating insulates the radiating anode areas and at the same time increases the coefficient of emissivity by about a factor of 2 to 3 versus pure tungsten.

In a first prototype, the hot anode is shielded from the other parts of the thruster by a water-cooled copper plate, which is diffusion welded and forms one of the neutral rings of the nozzle.

In order to compare these experimental results with those of a water-cooled one, the thruster is designed as closely as possible in the form of the "normal" Stuttgart nozzle-type thruster. The current is fed to the anode by 16 screws made of TZM, a molybdenum alloy, which at the same time act as a mounting support for the heavy anode flange.

In Fig. 38, the result of a thermal analysis is shown for the case of 60 kW power input, which is assumed to load the anode in a linear manner. The analysis was performed using a finite element procedure,<sup>22,23</sup> which utilizes the SMART temperature calculation code, developed at the Institut für Statik und Dynamik (ISD) of the University of Stuttgart. As a result, it is shown here that even at such a high power input (which corresponds to roughly 200 kW electrical power input to the thruster) the temperature would not at any place exceed 2600° C.

The initial tests with the HAT are intended to be carried out in a newly installed stainless steel vacuum tank of 2 m in diameter and 6 m in length. It is double walled to provide cooling capability.

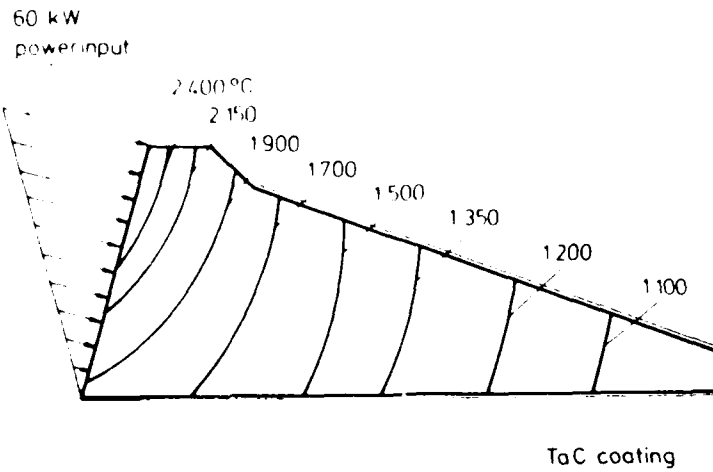


Fig. 38 Radiation-cooled tungsten anode, coated with tantalum carbide; calculated temperature distribution in degrees C with a non-uniform heat load of 60 kW.

### 3. Quasi-Steady Operated MPD Thrusters

In Fig. 39, specific impulse data from our experiments (stationary mode) and from some Princeton<sup>24</sup> and Tokyo<sup>13</sup> quasi-steady experiments were plotted against the correlation coefficient  $I^2/\dot{m}$ . The main differences that are striking are the substantially smaller  $I^2/\dot{m}$  values and therefore the smaller specific impulses which are reached in the continuous mode.

To check whether these great differences between these pulsed thrusters and our continuous thrusters are a function of the design configuration or of the operation mode, thrusters identical in geometry and electrode material were built (Figs. 40 and 41) and investigated in the quasi-steady mode.<sup>25</sup> The neutral segments which form the nozzle (Figs. 2 and 3) were replaced by ceramic insulators (Macor). The power source was a capacitor bank with electrolytic capacitors<sup>26</sup> of approximately 6 kJ, which provides a quasi-stationary discharge period for about 2 ms. Since the vacuum system was sufficiently large, the gas flow did

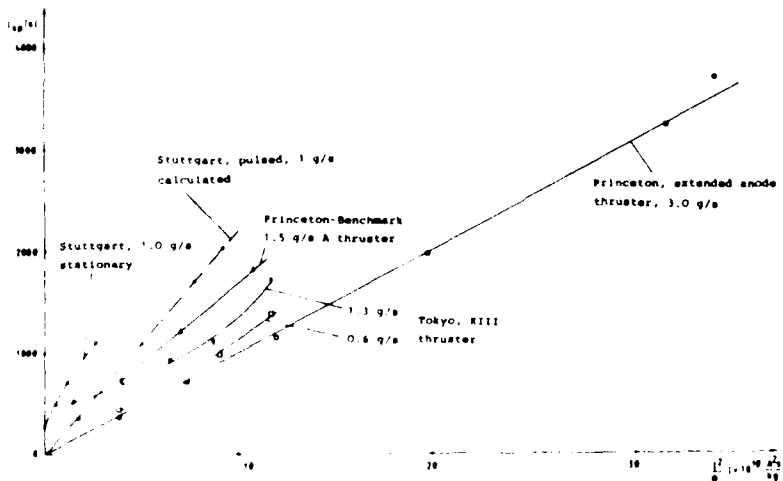


Fig. 39 Specific impulse as a function of the correlation parameter  $I^2/\dot{m}$  for different thrusters, stationary and pulsed ones: Stuttgart thruster, stationary (measured thrust) and pulsed (calculated thrust), Tokyo K III thruster, Princeton benchmark and extended anode thruster. Propellant is in all cases argon.

not have to be switched; that means that the electrical pulse was "switched into" a stationary gas flow. The main discharge was triggered by a high voltage spark, which was ignited between the cathode and the copper arc chamber wall. The discharge current was measured by a Pearson current transformer (301X) and the discharge voltage at the thruster terminals with a fast isolation amplifier. Both signals were stored on transient recorders. The main and the ignition power supply potentials were floating.

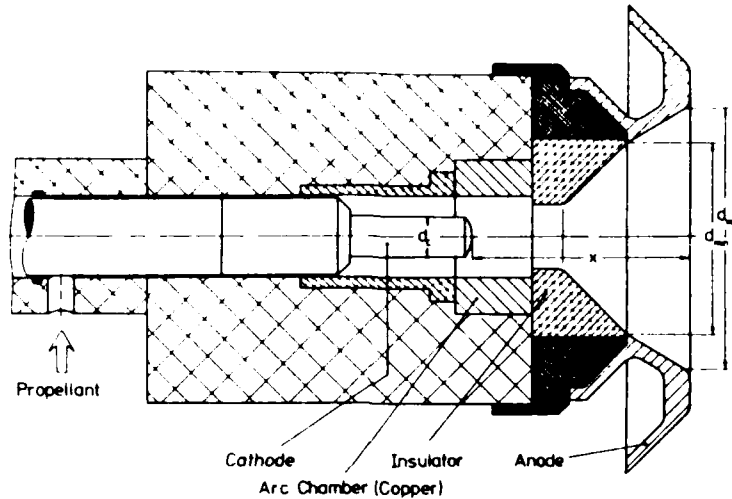


Fig. 40 Thruster head configuration for quasi-steady operation, corresponding to thruster DT1.

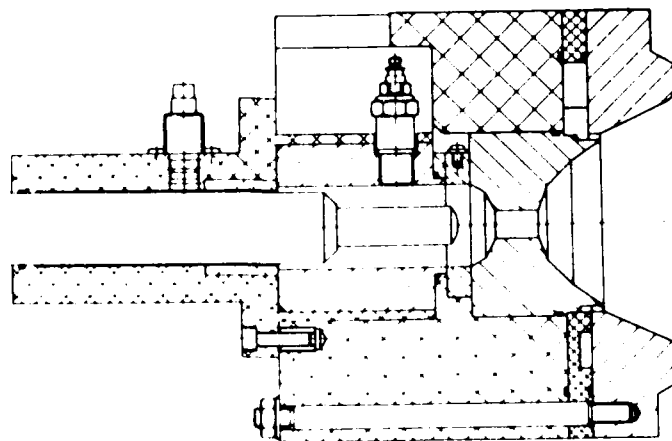


Fig. 41 Thruster head configuration for quasi-steady operation, corresponding to steady-state thruster DT3.

As onset criterion, the appearance of high voltage oscillations on the voltage traces, which happen to coincide with the usual 10% fluctuation, was taken. In Fig. 42, the result of the measured relative voltage fluctuations for different mass flows are plotted versus the correlation parameter  $I^2/\dot{m}$ . For  $I^2/\dot{m} < 1 \cdot 10^{10}$  A<sup>2</sup>/kg, no voltage oscillations could be observed, but they start almost instantaneously above this "critical" value with a magnitude of 10% and above, so that for this thruster and an ambient pressure of ca.  $2 \cdot 10^{-2}$  mbar, the critical or onset point proved to be  $1 \cdot 10^{10}$  A<sup>2</sup>/kg, a factor of 2.5 smaller than within the continuous operation mode!

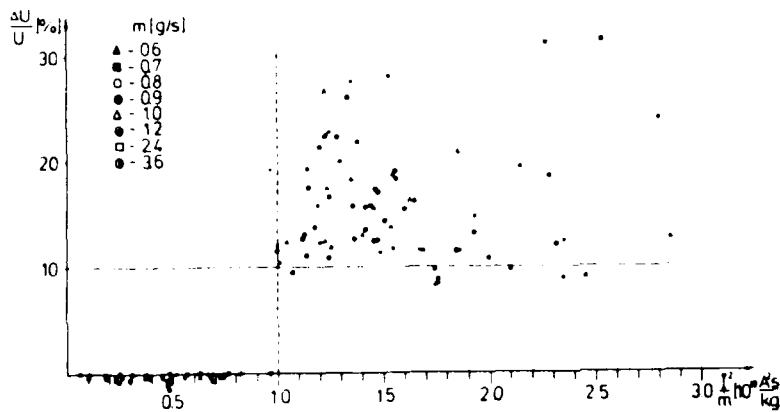


Fig. 42 Relative voltage fluctuations for different mass flows vs. correlation parameter  $I^2/\dot{m}$ , with argon as propellant.

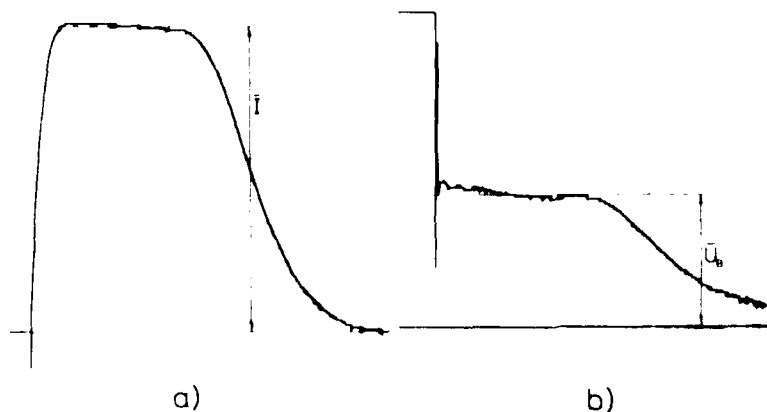


Fig. 43 Typical a) current and b) voltage wave forms below onset ( $I^2/\dot{m} = 5 \cdot 10^9$  A<sup>2</sup>/kg).

In Figs. 43 to 45, typical current and voltage wave forms are plotted from the transient recorder. Fig. 43 shows the traces for a typical discharge under the critical region ( $I^2/\dot{m} \approx 0.5 \cdot 10^{10}$  A<sup>2</sup>s/kg): the current pulse is almost rectangular and the voltage pulse is also smooth and over a long period constant.

Fig. 44 shows the current pulse and two voltage pulses for the region just above the onset ( $1.0 \cdot 10^{10} < I^2/\dot{m} < 1.5 \cdot 10^{10}$  A<sup>2</sup>s/kg): the current pulse deforms and the constant part gets smaller. In Fig. 45, the case high above onset is plotted: the current shows a distinct peak at the beginning which corresponds to the depression in the voltage trace. The whole pulse period is prolonged.

Current voltage characteristics with the mass flow as parameter are shown in Fig. 26 in a double-log plot. They show the familiar kinked form<sup>13, 27</sup> with a constant slope up to a certain current value and then an abrupt jump to a steeper, also constant

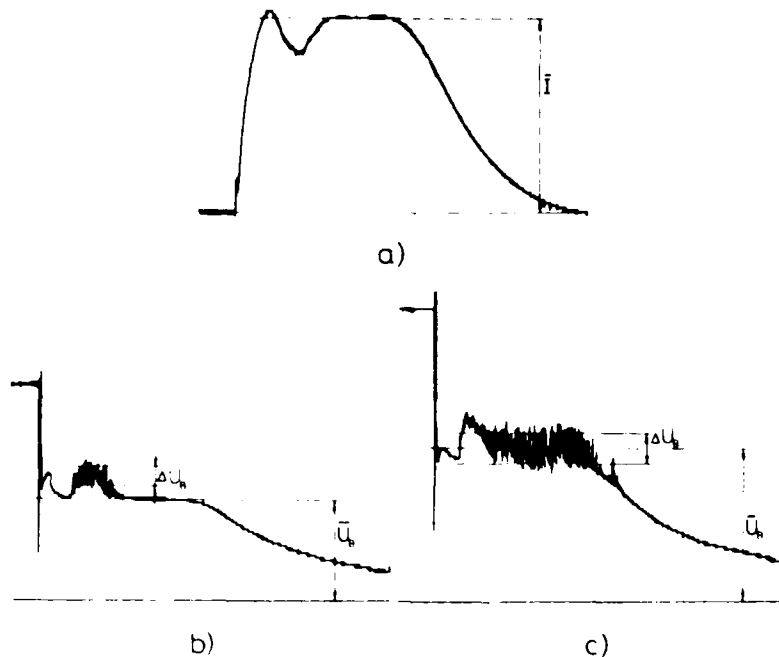


Fig. 44 Typical a) current and b), c) voltage wave forms just above onset. b)  $I^2/\dot{m} = 1.1 \cdot 10^{10}$  A<sup>2</sup>s/kg, c)  $I^2/\dot{m} = 1.4 \cdot 10^{10}$  A<sup>2</sup>s/kg).

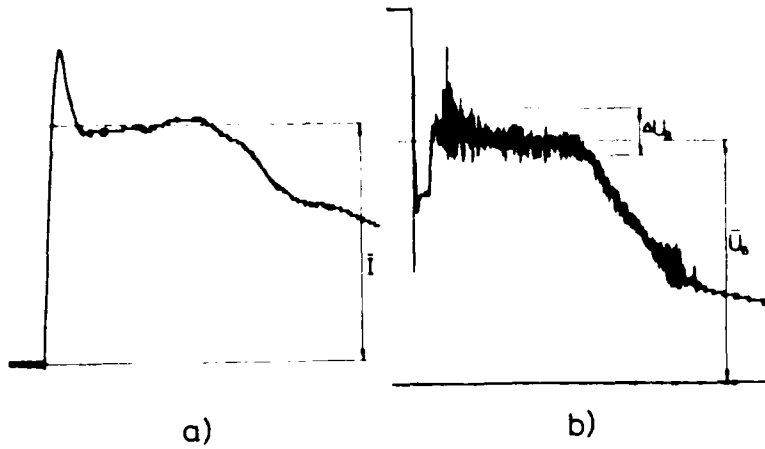


Fig. 45 Typical a) current and b) voltage wave forms well above onset ( $I^2/\dot{m} = 2.9 \cdot 10^{10} \text{ A}^2\text{s/kg}$ ).

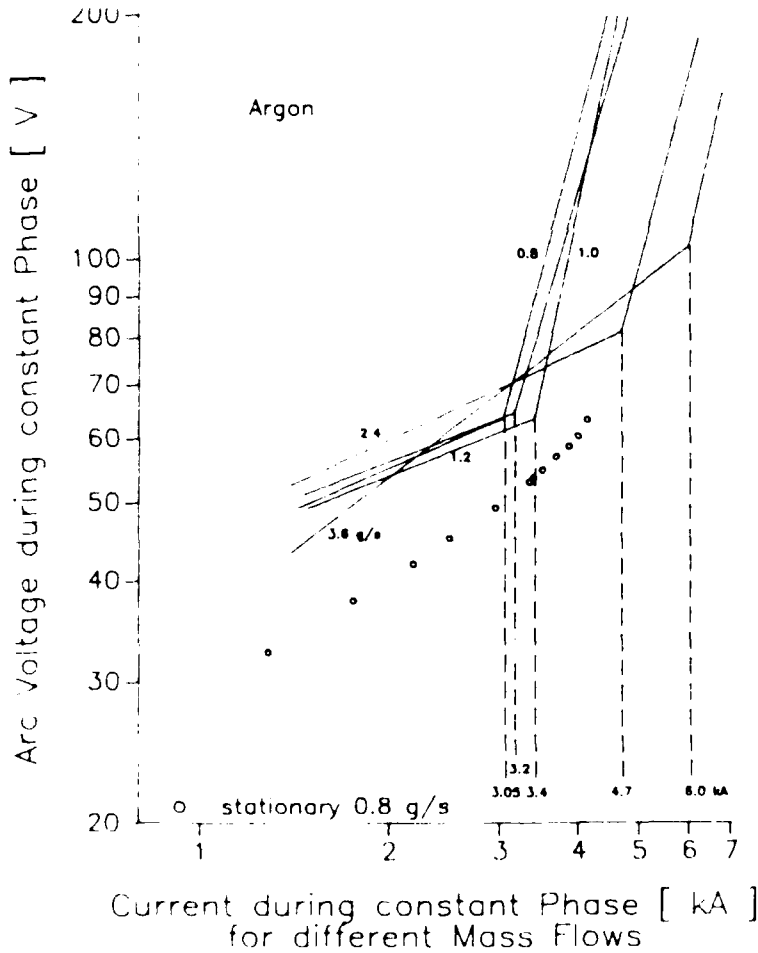


Fig. 46 Current-voltage characteristics with the argon mass flow as parameter. Dotted line represents the continuous thrust as comparison.

- 46 -

slope. In these experiments, this "knee" coincides with the onset current, which seems reasonable, since the "onset" marks another physical behavior of the arc with higher anode losses and voltages. Kuriki<sup>11</sup> called this knee "critical current", but defined as onset a "limiting current" which is located somewhere on the steep branch of the characteristic. Choueiri<sup>12</sup> found in the "knee" the beginning of an instability which is related to the transition to a fully ionized plasma, and which is damped away at higher currents still well below onset point. As in the case with steady state thrusters, our experiments with these pulsed devices showed that currents above onset point are always connected with melted spots at the anode, because the former diffuse anode attachment of the arc probably constricts to overcome a so-called "anode starvation".<sup>13</sup> We have noticed such melting spots with all currents above the "knee", so that setting this "knee current" as onset current seems meaningful.

In the same figure (46), a dotted line is used to plot the voltage characteristic of the continuous mode; this dotted line has lower values and the oscillations appear after this angle point. This indicates that these two instabilities may be of different origin. The lower voltages are probably caused by the lower cathode fall with a glowing tungsten cathode compared to a cold one. A further indication that the onset point is a change in the physical behavior is shown in Fig. 47. The current output of the PFN for a given charging voltage  $U_c$  as a function of the mass flow shows a distinct kink at a current, which coincides with the onset.

In a series of experiments, the dependence of onset with the ambient pressure was investigated, which showed that with increasing ambient pressure the onset current rises substantially (Fig. 48). This result contradicts the findings with steady state thrusters, which indicates that both operation modes, quasi-steady pulsed and continuous, are not only distinguished by different cathode conditions, i.e. cold and hot, but also by other still unknown effects.

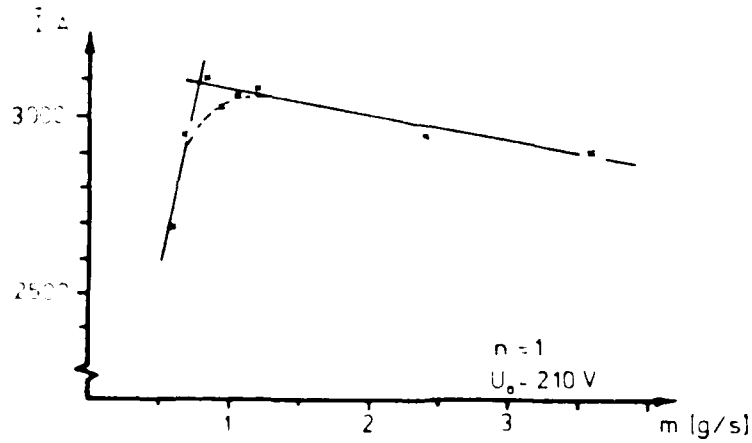


Fig. 47 Discharge current as a function of mass flow for a given charging condition of the PFN.

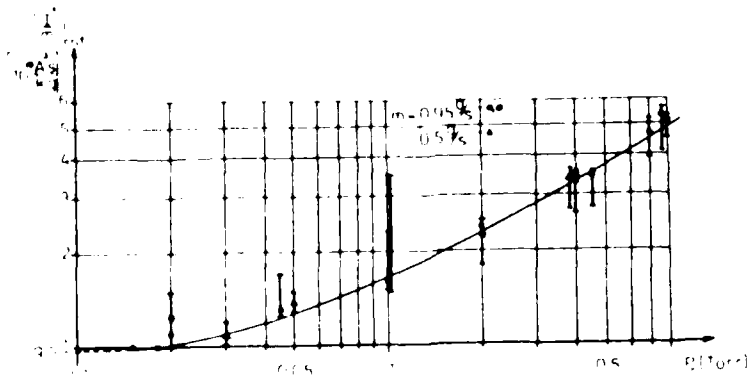


Fig. 48 Onset of the quasi-steady thruster as a function of ambient pressure.

### Thrust

Thrust is measured in an indirect manner. The thruster is mounted on a pendulum thrust balance and the total impulse of the discharge is measured by the pendulum displacement. The thrust is then calculated by assuming a rectangular discharge pulse.<sup>40</sup> The balance is calibrated by applying a known impulse.

Measurements of thrust were taken with argon (Fig. 49) and nitrogen (Fig. 50) as propellant for several mass flow rates and currents. In both figures the thrust of the continuously running thruster is displayed for comparison as dashed lines for one mass flow, along with the possible minimal and maximal magnetic thrust. The thrust of the pulsed experiments is smaller, especially at lower currents. A possible explanation could be that the thermal heating of the propellant is incomplete because of turbulences caused by jumping cathode attachment spots of the arc. This is confirmed by high speed films (20000 frames/s)--no stabilization of the jet plume could be observed during the 2 ms pulse. The specific impulse as a function of the parameter  $I^2/\dot{m}$  is plotted in Fig. 51 with mass flows as parameter for nitrogen. The specific impulse runs almost linear to  $I^2/\dot{m}$  over a wide range and runs parallel to the magnetic specific impulse.

The efficiencies, shown in Figs. 52 and 53, are lower than in the continuous case because of the lower thrust and the higher discharge voltages.

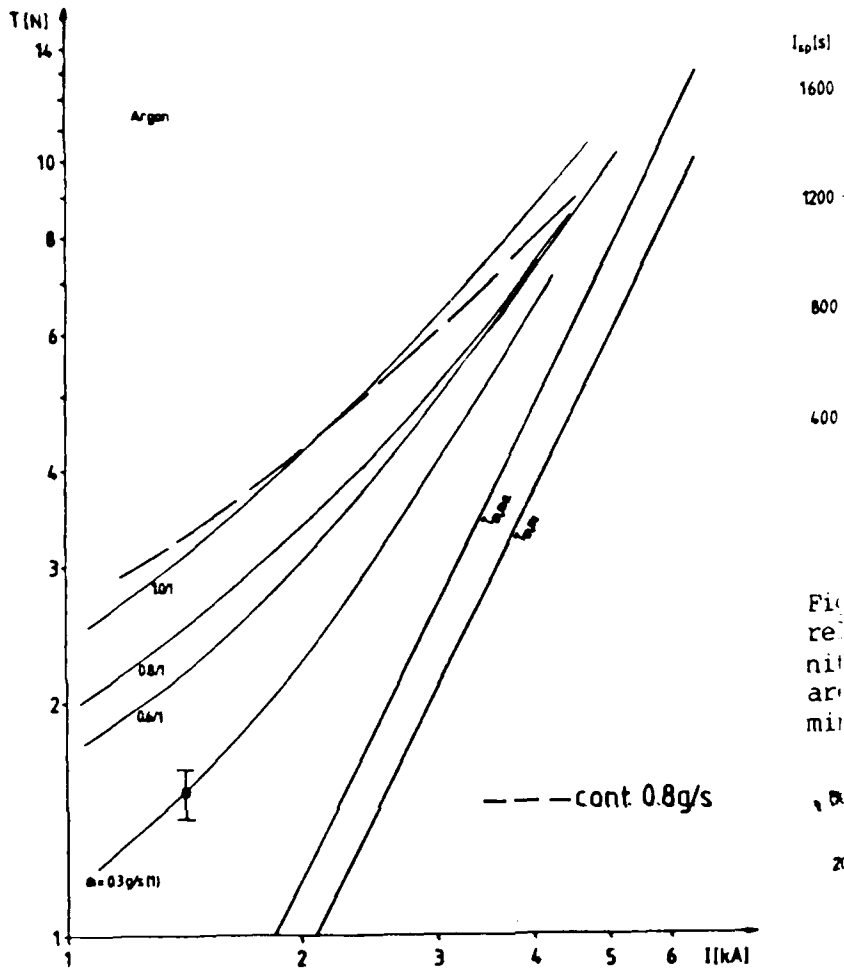


Fig. 49 Thrust as a function of current with argon mass flow as parameter. Dotted line represents the continuous thruster as comparison.  $T_{m,min}$  and  $T_{m,max}$  are the calculated electromagnetic thrust.

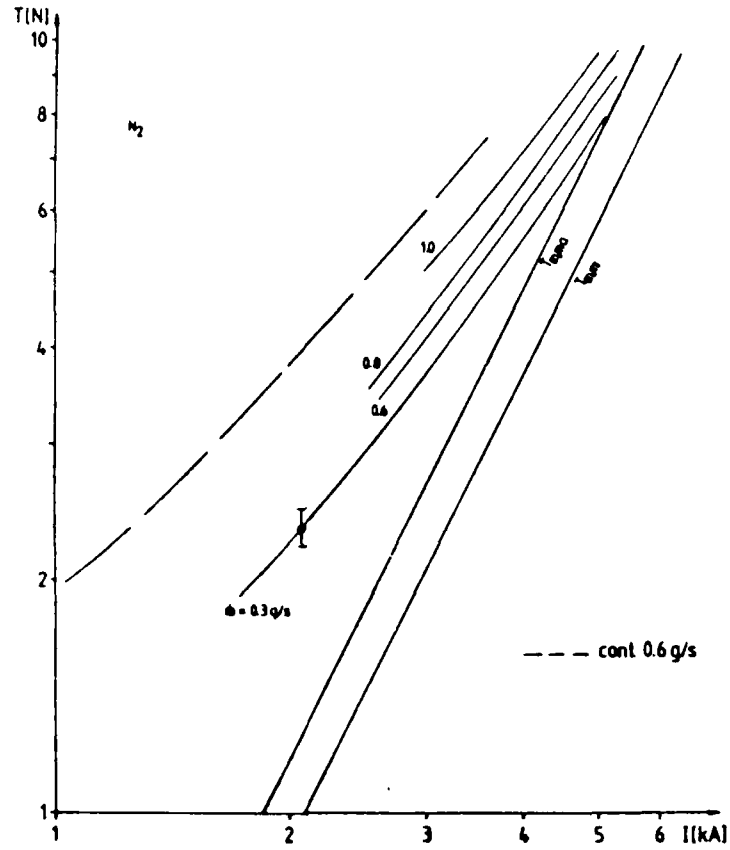


Fig. 50 Thrust as a function of current with nitrogen mass flow as parameter. Dotted line represents the continuous thruster as comparison.  $T_{m,min}$  and  $T_{m,max}$  are the calculated electromagnetic thrust.

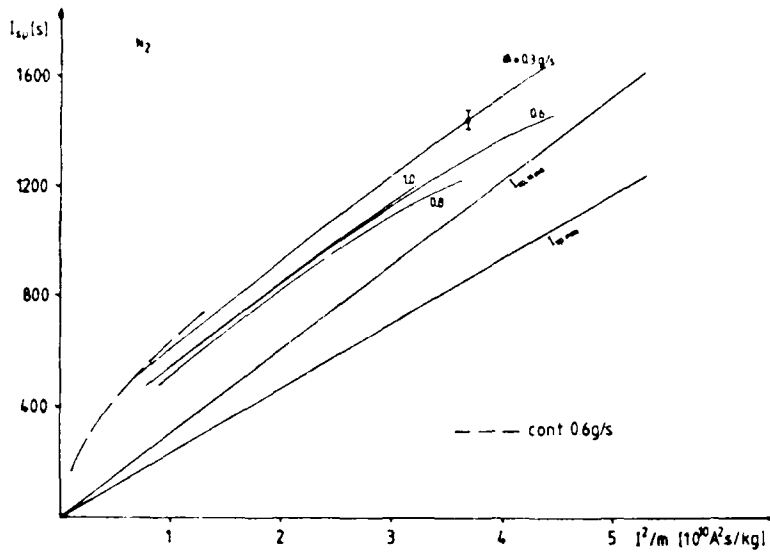


Fig. 51 Specific impulse as a function of the correlation parameter  $I^2/m$  for several mass flows with nitrogen as propellant.  $I_{sp,max}$  and  $I_{sp,min}$  are the calculated magnetic impulse for maximal and minimal anode radius.

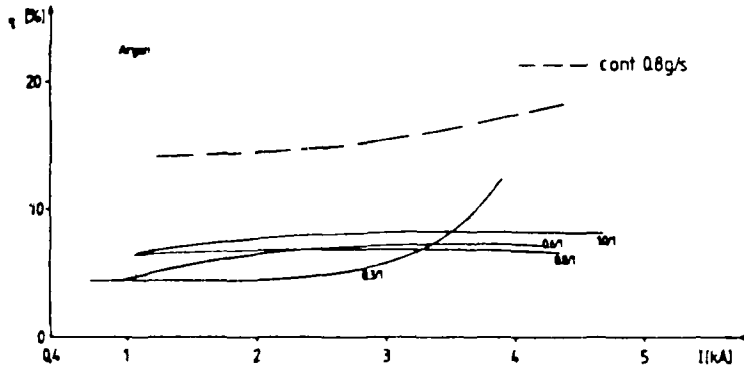


Fig. 52 Thrust efficiency vs. discharge current for different mass flows of argon. Dotted line represents the continuous thruster as comparison.

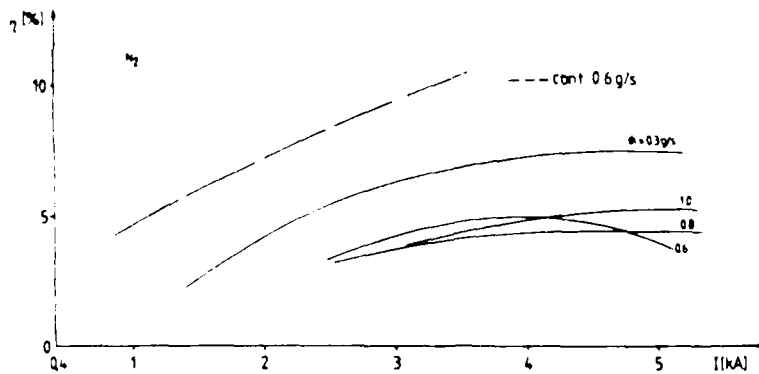


Fig. 53 Thrust efficiency vs. discharge current for different mass flows of nitrogen. Dotted line represents the continuous thruster as comparison.

### Magnetic Probe Measurements

Magnetic probe measurements are not possible on a continuous plasma jet because of the high heat loads on the probe. These, however, are of minor influence with pulsed jets. With an isolated magnetic probe, the current contour lines were measured<sup>29</sup> and are compared with calculated lines in Fig. 54. They coincide fairly well for the 10% and 20% current contour line. The fact that in the measured case the anode attachment is more concentrated downstream of the nozzle end than in the calculated case may be attributed to the theoretical model which neglects the boundary layer along the nozzle and anode walls and takes a uniform conductivity over the cross section. The theoretical model is described in detail in chapter 5.

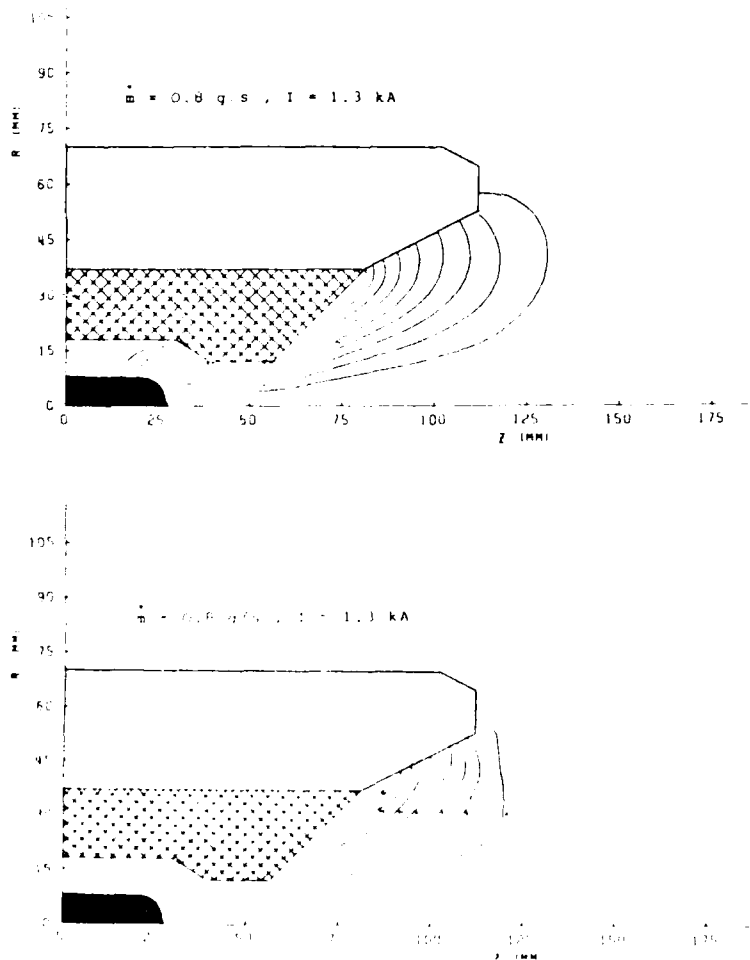


Fig. 54 a) Calculated and b) measured current contour lines of an MPD discharge in the nozzle-type plasma thruster D2 for 0.8 g/s argon and 1300 A discharge current.

With the measured current contour lines and a calculated electrical conductivity, taken as constant, the Joule's heat source distribution was determined in Fig. 30 a) for 1300 A and in b) for 3150 A. With higher current, the heating zone constricts to the middle axes.

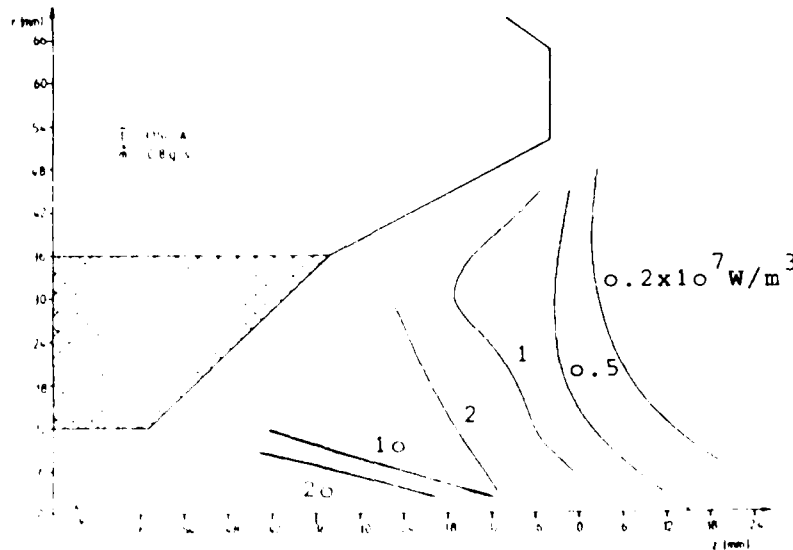
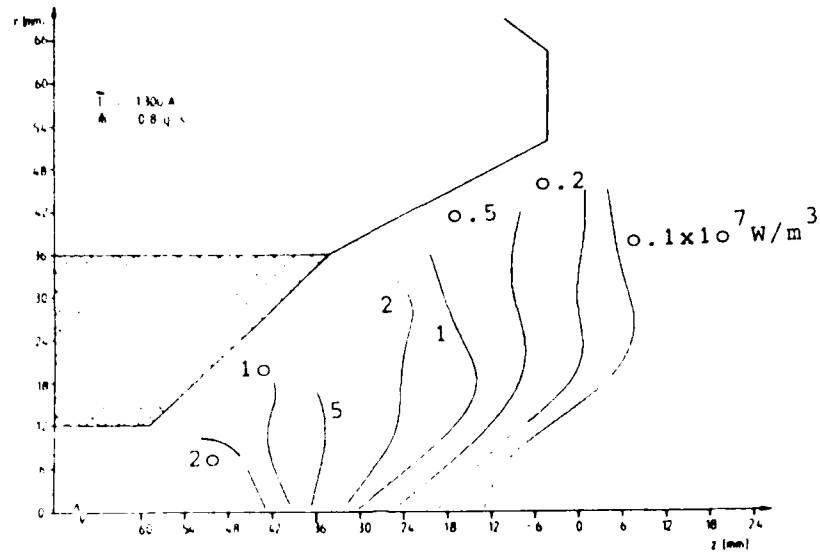


Fig. 55 Isolines for the Ohmic heat source term for a) 1300 A and b) 3150 A discharge current.

### Concluding Remarks

The experimental results presented are part of a greater effort to understand MPD propulsion and the related phenomena, which include theoretical investigations, both of the midstream flow field and electrodes and of erosion. The goal of the experiments is twofold: first to give a basis of data for the theories and second to come up with better and more efficient thruster designs, since the performances of self-field MPD thrusters, at least in the investigated power field  $< 500$  kW, are quite modest. With regard to this second goal, the experiments presented here can be summarized:

1. The acceleration mechanism of nozzle-type MPD thrusters in the tested performance regime is not only determined by the self magnetic forces but also to a great extent by thermal expansion.
2. The influence of cathode position on the thruster performance is a further proof of the important role of the thermal acceleration.
3. A variation of the ambient tank pressure up to 0.5 mbar hardly influences the thruster performance. Also, the onset point is not shifted with steady operation mode. Thus, the evaluation of specific impulse and efficiency with direct thrust measurement are valid; no entrainment of ambient gas is to be expected at operation below onset.
4. The performance improvement hoped for in nozzle-type thrusters with anode gas injection due to shifting of the onset to higher currents was not realized.
5. With anode gas injection, the onset phenomena were split: at least two onset effects with steady state MPD thrusters could be observed:
  - a) anode spot attachment due to particle starvation
  - b) high frequency current oscillations.This indicates that the onset limitations are caused by several different physical reasons.
6. At these low power ranges, the lighter propellant nitrogen shows no advantages over argon.

7. First experiments with a cylindrical thruster proved the feasibility of a cathode protruding from the backplate. The current distribution on the anode depends to a large extent on the cathode position.
8. Quasi-steady, pulsed, nozzle-type thrusters showed worse performances in the power range considered than steady-state operated thrusters:
  - a) higher voltages, due to the cold cathode
  - b) lower thrust, perhaps due to the worse input of the ohmic heat because of turbulent flow in the thruster
  - c) lower onset values, which occur at the "knee" of the voltage current characteristics.

#### 4. Cathode Erosion Studies on MPD Thrusters

##### 4.1 Introduction

It is a known phenomenon that in a pulsed MPD thruster<sup>13, 30, 31</sup> and during the starting phase in a continuous MPD thruster<sup>32, 33</sup> the arc cathode attachment resembles many hot spots of high current density. These spots are usually highly nonstationary and jump across the cathode surface. Such a spotty attachment is indeed the most common one on cold metal cathodes of low pressure arcs<sup>34, 35</sup> and seems to be an intrinsic feature of those discharges. Despite the growing literature on this phenomenon, it is still not fully understood. However, since the time resolution of electrical and optical measuring techniques went up into the  $\mu$ s and even beyond the nanosecond range, and since scanning electron microscopy became a widespread technique of investigating the arc traces left on cathode surfaces, one has learned much more on the mechanisms of this spotty attachment. Today one distinguishes between a) microspots with diameters of several  $\mu$ m (maybe even less) and with current densities of the order of  $10^{12}$  A/m<sup>2</sup> (maybe even higher) and displacement velocities of several hundred meters per second and b) spots which are much more stationary (velocities of the order of several m/s) with diameters of up to 100  $\mu$ m.<sup>36</sup> These latter, larger spots appear to be the result of spot clustering; i.e., due to favorable emission conditions, the microspots do not spread over a larger area but rather stick to a smaller area, and by locally overheating this area cause larger molten zones and relatively heavy damage to the cathode. If such a clustering does not occur, the microspot damage is less severe because of the rapid spot motion, and because consequently there is more widespread averaged heatload on the cathode surface.

Another quite interesting feature is the fact that the average number of spots is proportional to the arc current, and that a single spot can carry only a limited current, the quantity of which depends on the cathode material.<sup>37, 38</sup>

Within a transverse magnetic field, these spots jump preferably into the retrograde direction, i.e. they move oppositely to Ampere's law as long as the ambient pressure is small enough.<sup>39, 40</sup>

These are only some of the most striking known and established effects observed on spotty cathodes. Many more detailed spot features have been observed and put forward, but they cannot be dealt with in the framework of this paper. Reference shall therefore be made to the literature.<sup>35</sup>

Nevertheless, since a variety of these effects are obviously involved at the cathode-arc interphase of MPD thrusters, it is mandatory that this spot behavior be investigated in order to understand and predict the discharge and erosion effects during the starting phase of a continuous or during the pulse phase of a quasi-steady MPD-arc thruster.

After the starting phase of a continuously running thruster, which lasts about a fraction of a second or a few seconds depending on the arc current, the cathode, which usually consists of a thoriated tungsten rod--so far the only successfully used in continuous thrusters--starts to glow, and the original spotty attachment becomes a quiet, more diffuse one. The current densities of these diffuse attachments on bright glowing tungsten cathodes are of the order of  $10^7$  A/m<sup>2</sup> and are commonly explained by thermionic emission,<sup>32</sup> while the high current densities of the spots can only be interpreted by means of field or enhanced thermal field emission.<sup>41, 42</sup>

The following section reports about erosion measurements on pulsed and continuous MPD thrusters and consequently on spotty and diffuse cathode attachments, while the subsequent sections give a partially quantitative theoretical interpretation and discussion of the experimental findings.

## 4.2 Experiment

The cathode erosion tests have been conducted on the nozzle-type MPD thruster DT1, shown in Fig. 2. For the pulsed thruster experiments, the water-cooled segments up to the anode ring have been replaced by a heat resistant glass ceramic (MACOR) and the water cooling in anode and cathode not applied. The eroded mass is determined by weighing the cathode before and after the experiment with a precision balance having an accuracy of 1 mg at a weighing range of 1 kg.

### Steady State MPD Thruster

With steady state operating MPD thrusters, two different modes of erosion must be distinguished:

a) Starting with a cold cathode, heavy erosion takes place, which can usually be detected as a sort of "spitting" of glowing particles or droplets. Some tenth of a second to several seconds later, the cathode tip becomes hot and glowing so that thermionic or enhanced thermal field emission can occur and the discharge becomes stable and quiet.

b) During the steady state operation phase, the arc attachment is confined to the bright glowing area of the cathode tip. The erosion effect is much smaller, and no glowing particles are ejected.

To measure these different erosion rates, two series of tests were performed: long duration and start-only runs.

Erosion during starting phase. During the "start-up phase", the arc attachment consists of many highly unstationary hot spots which jump over the cathode surface and which cause a relatively high evaporation and even splashing of cathode material.

A current voltage plot of this initial starting phase ( $0 < t < t_1$ ) is shown in Fig. 56. To determine the average eroded mass during this starting phase, experiments with 30 to 50 runs with different preset ignition currents were performed. In each case, the arc was extinguished after stabilization. To exclude eventual thermal effects in the starting phase, a waiting period of

about 10 minutes was taken between the tests to cool down the cathode. Depending now on the ignition current  $I_I$  set by the power supply, the time duration  $t_I$  of the starting phase, i.e. the time to heat up the cathode, varies between about a fraction of a second and several seconds, as shown in Fig. 57.

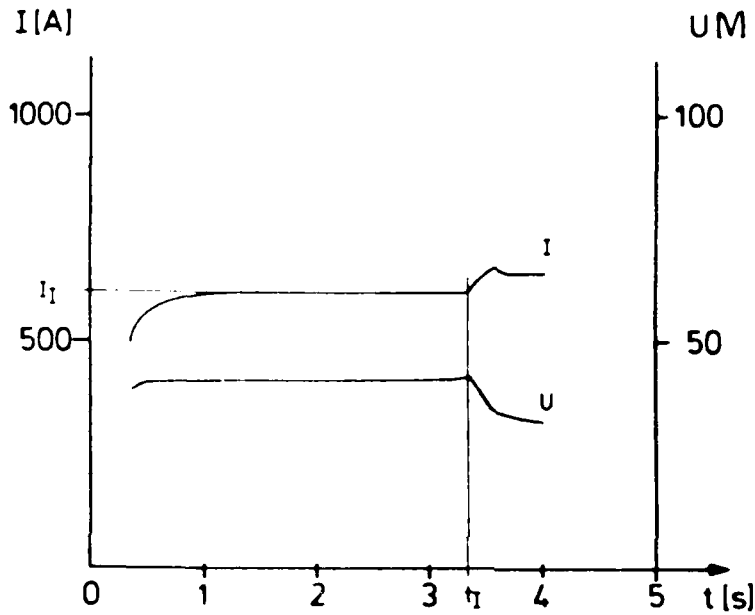


Fig. 56 Typical current and voltage traces during starting phase.

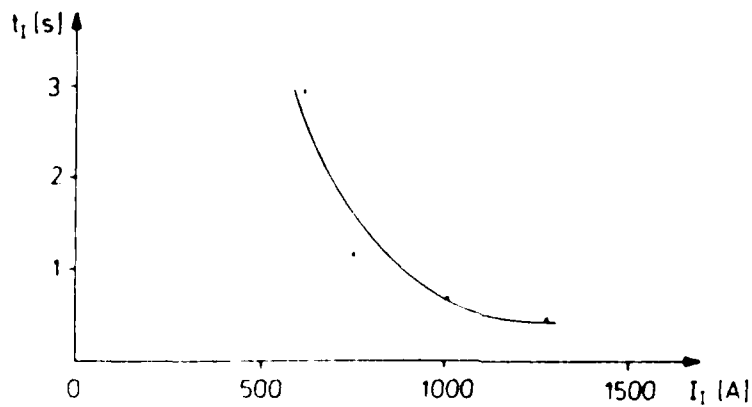


Fig. 57 Starting phase duration as a function of ignition current  $I_I$ .

Based on these experiments, it became clear that by far the major erosion takes place during the starting phase when the cathode is still fairly cold and a spotty discharge exists.

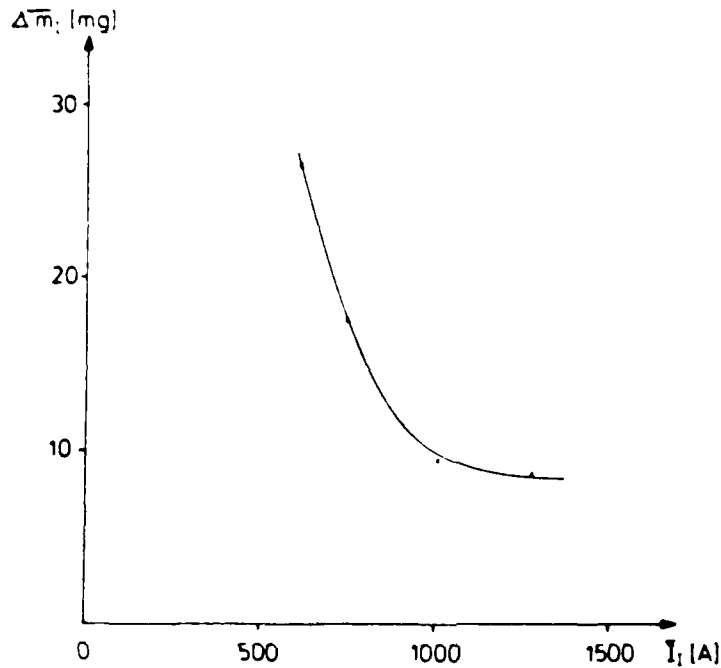


Fig. 58 Average mass loss during starting phase as a function of the ignition current  $I_1$ .

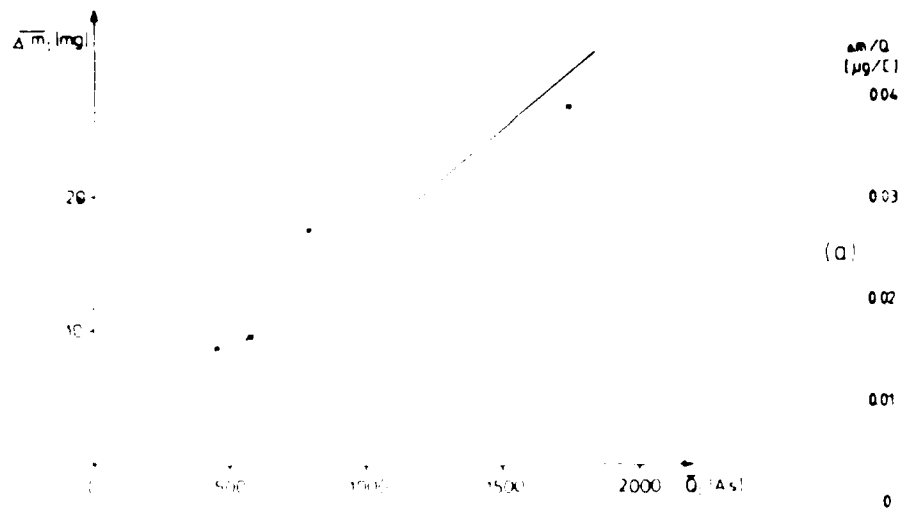


Fig. 59 Average mass loss during starting phase as a function of the accumulated charge  $Q_1$ .

In Figs. 58 and 59, the average mass loss is plotted after about 30 to 50 runs as a function of the ignition current and the corresponding accumulated charge during the starting phases, respectively. The total average mass loss per arc ignition amounts to about 25 mg for a preset arc ignition current of 600 A and decreases to about 10 mg and to a little less if the ignition current is 1000 A and more. Since with increasing current  $I_1$  the cathode heats up faster, and therefore the time elapsed during the starting phase becomes smaller, the total mass loss decreases with increasing ignition current. As a function of the accumulated electric charge  $Q_1$ , however, the mass loss increases with  $Q_1$  almost linearly. By taking the least square fit slope we obtain an average erosion rate for the starting or initial phase of 16.7  $\mu\text{g}/\text{As}$ .

Erosion during steady state operation. During the long duration tests, lasting about 240 to 60 minutes at steady state currents between 1500 and about 4000 A, respectively, i.e. below onset conditions (since steady state MPD thrusters must be run below onset to avoid destruction), the measured total mass loss is about 400 mg. The erosion rate--not counting the losses of the starting phase--amounts to about 0.03  $\mu\text{g}/\text{As}$ , which is three orders of magnitude below that of the ignition phase. The measured erosion rates, given by the cathode mass loss  $\Delta m$  divided by the accumulated electric charge  $Q$  in  $\mu\text{g}/\text{C}$ , for the continuously running steady state arc are plotted as a function of arc power, arc current and as a function of the correlation factor  $I^2/\dot{m}$  in Figs. 60a,b,c, respectively, where  $\dot{m}$  is the propellant mass flow. In all three cases the erosion rate may be considered a constant and is independent of  $P$ ,  $I$  and  $I^2/\dot{m}$ , i.e. one may conclude that the mass loss per unit time,  $\dot{m}_v = \Delta m/\Delta t$ , is proportional to the current. Since  $Q = I\Delta t$ , one obtains a mass loss rate of about

$$\dot{m}_v = \frac{\Delta m}{\Delta t} = 0.03 \cdot I \quad \text{mg/s} \quad (4)$$

for the continuous running steady state thruster.

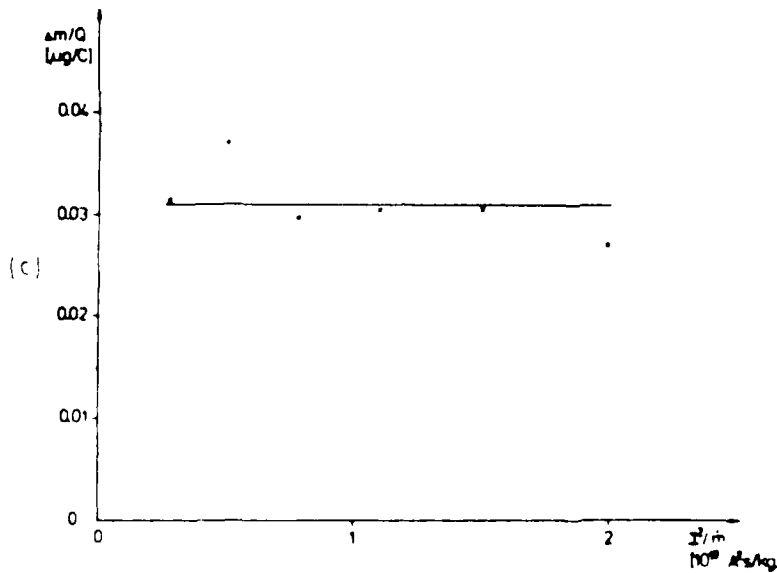
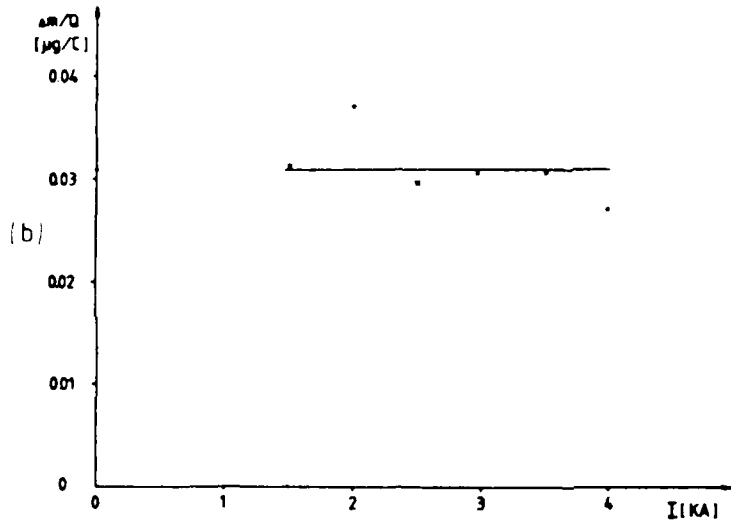
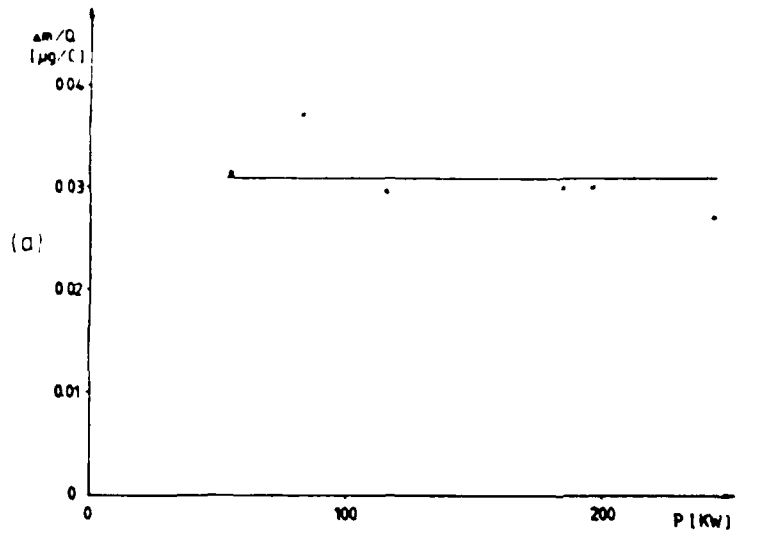


Fig. 60 Steady state erosion rates versus a) arc power, b) arc current, c) correlation parameter  $I^2/m$ .

### quasi-steady MPD Thruster

Measurements on a pulsed thruster with the same electrode material and geometry<sup>22</sup> show an average erosion rate of about 14 ( $\pm$  3.5)  $\mu\text{g}/\text{C}$  with argon as propellant and 16 ( $\pm$  3.5)  $\mu\text{g}/\text{C}$  with nitrogen as propellant (see Fig. 61). These latter results were obtained by weighing the cathode before and after about 420 shots at the same operation conditions. The pulsed thruster was energized by a pulse-forming network with electrolytic capacitors<sup>23</sup> which produces rectangular current pulses of up to  $I_{\text{Max}} = 8000 \text{ A}$  lasting about 2 ms. It is interesting to note that the erosion rate measured for the pulsed thruster is about the same as that for the initial phase of the continuous thruster, but also is a factor 3 to 5 greater than the erosion measured in Japan with quasi-steady thrusters.<sup>13, 30</sup>

In the following section, an explanation of a) the spotty "cold cathode attachment" with a fairly high erosion rate and b) the more diffuse "hot cathode attachment" of much lower erosion will be presented.

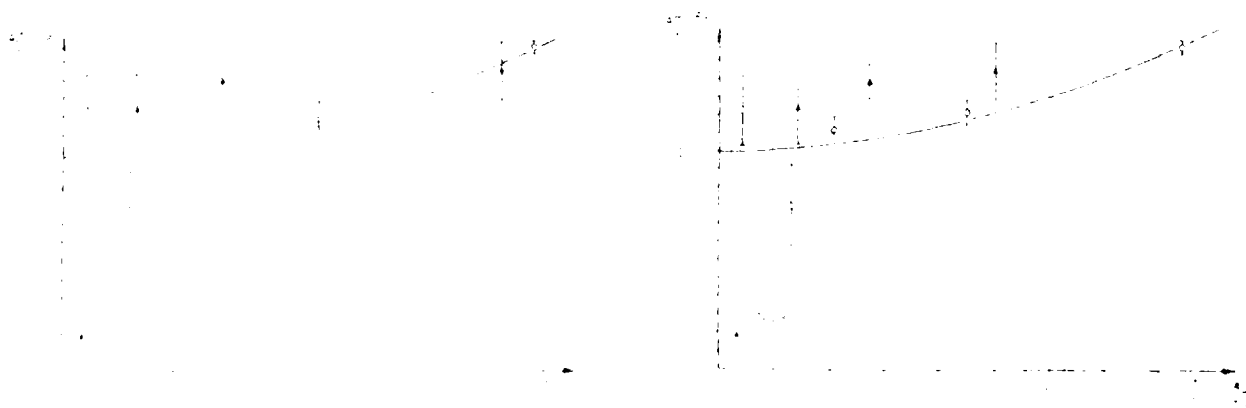


FIG. 61. Erosion rate in quasi-steady operation versus a) arc power, b) correlation parameter,  $I, \text{m}$ .

### 4.3 Theory

Based on the experimental findings, one distinguishes between (a) a spotty, more or less highly erosive and (b) a bright glowing diffuse, low erosive cathode attachment within an MPD-arc thruster. First, let us consider the spotty arc cathode.

#### Cold Spotty Arc Cathode

The starting phase of an MPD-arc may be described by the following: at any favored spot (microprotusion and/or dielectric impurity) on the cathode surface, the electric field becomes strong enough to start a breakdown. This breakdown causes a local overheating of the emitting, microscopic spot site, thus leading to evaporation and a plasma cloud which expands from the spot site on the cathode surface into the gaseous half space. After this first ignition phase, which according to Guile and Jüttner<sup>34</sup> may last about  $10^{-9}$  s, a small crater with a diameter of a few microns is formed (see Fig. 62). A few typical, but more developed craters left on the surface of a thoriated tungsten cathode are shown in the photomicrograph of Fig. 63.

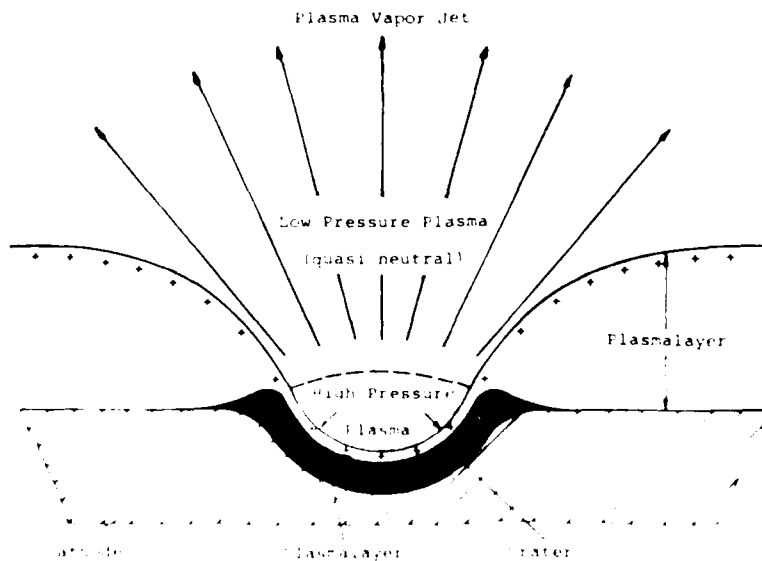


Fig. 62 Configuration of the plasma layer within and around a crater of a cathode spot,

The plasma is now interconnected with the inner crater surface by a space charge layer of several Debye length. The electric field in the space charge layer on the surface can now be calculated as a function of the temperatures  $T_e$  and  $T_i$  (Kelvin) and the Debye length  $\lambda_D$ ; it is

$$E = \frac{2kT_e}{e\lambda_D} \left( \frac{M_i}{M_e} \right)^{1/2} \quad (5)$$

where  $M_e$  is the mass of the electron gas, and  $M_i$  is the mass of the metal atoms within the space charge layer. This relation is also valid for the thickness within the crater is of the order of the crater size, or as long as

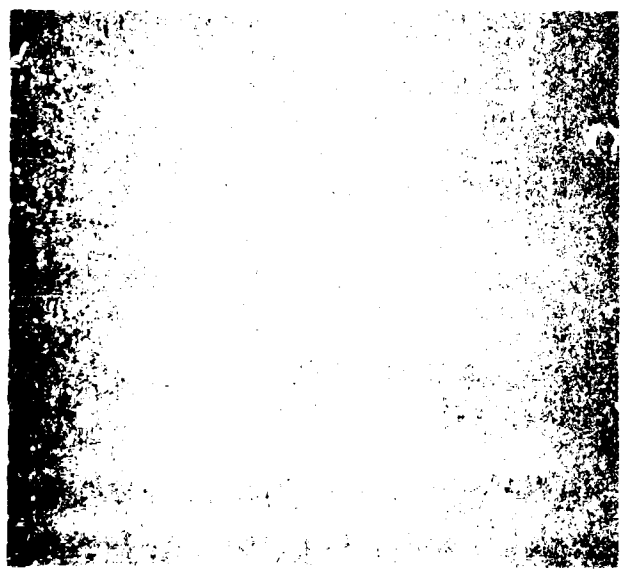


Fig. 1. Tungsten cathode surface (magnification 1000).

the Debye length given by

$$\lambda_D = \sqrt{\frac{\epsilon_0 k T_e}{2e^2 n_e}} = \frac{k T_e}{e} \sqrt{\frac{\epsilon_0}{e p_e}} = 1.813 \cdot 10^{-10} \frac{T_e}{\sqrt{p_e}} \quad [\text{m}] \quad (6)$$

is much smaller than the crater radius  $r_0$ . Indeed, within the crater the plasma pressure and hence the partial pressure of the electron gas can be considered as much higher than outside<sup>18</sup>; therefore,  $\lambda_D$  and the thickness of the plasma layer above the inner crater surface is thin ( $\ll r_0$ ) while outside of the crater the plasma layer is relatively thick. As a consequence of this plasma boundary configuration, the electric field strength  $E_0$  on the concave crater surface is much larger than outside and therefore strong enough to maintain a high current density, due to field emission or thermal field emission on the inner crater surface. The following quantitative discussion shall corroborate this explanation.

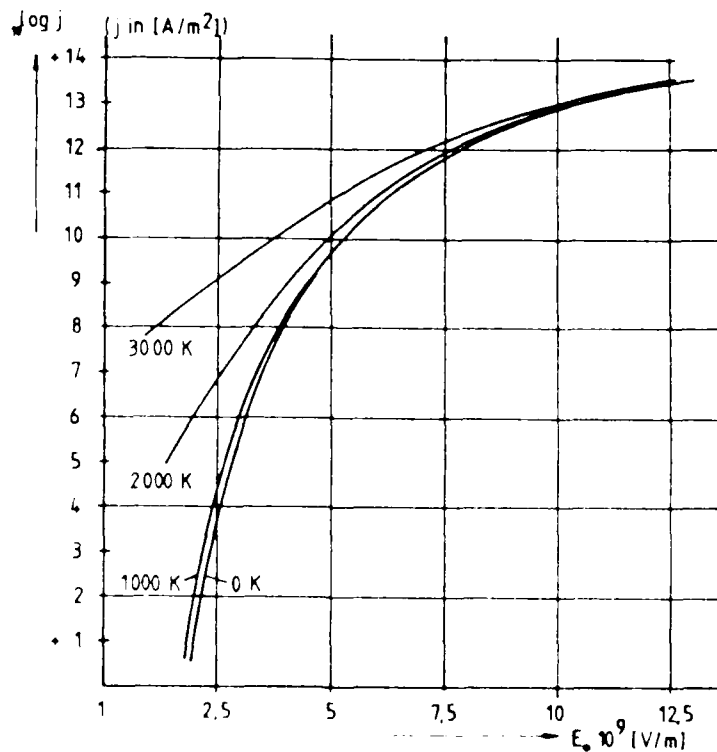


Fig. 64 Current density due to thermal field emission for an electrode work function  $\phi = 4.5 \text{ eV}$  (tungsten).

In Fig. 64, the critical field strength for thermal field emission is plotted as a function of the electric field strength  $E$ , for a tungsten cathode with a surface work function of  $\phi = 4.5$  eV. In order to obtain current densities of the order of  $10^{10}$  to  $10^{11}$  A/m<sup>2</sup> (and correspondingly,  $E$  should be about  $5$  to  $8 \cdot 10^7$  V/m). Accordingly, a space charge field of this strength requires a partial pressure of the electron gas of  $p_e = 4.6 \cdot 10^3$  to  $1.2 \cdot 10^4$  V/m, which is the high pressure tungsten vapor plasma. Since the plasma temperature must be taken larger than  $10,000$  K, this electron pressure corresponds to a plasma pressure of about  $0.1$  to  $1$  bar. This temperature of the spot plasma exceeds by far one bar, so that the electric field is strong enough to explain the high current densities of  $10^{11}$  A/m<sup>2</sup> (and may be even higher on certain spots located within an active crater); it moreover shows that the spot radius is smaller than  $\lambda_D < 0.1$   $\mu\text{m}$ , i.e. much smaller than the crater radius of about  $1$   $\mu\text{m}$ .

The structure of the active spot may therefore be described by a high pressure plasma spot region, from which a strong jet expands into the whole space of lower pressure. This plasma jet is directed upwards, i.e. it contains a current channel which is directed towards the high pressure spot plasma with the cathode surface and the anode (see Fig. 65a).

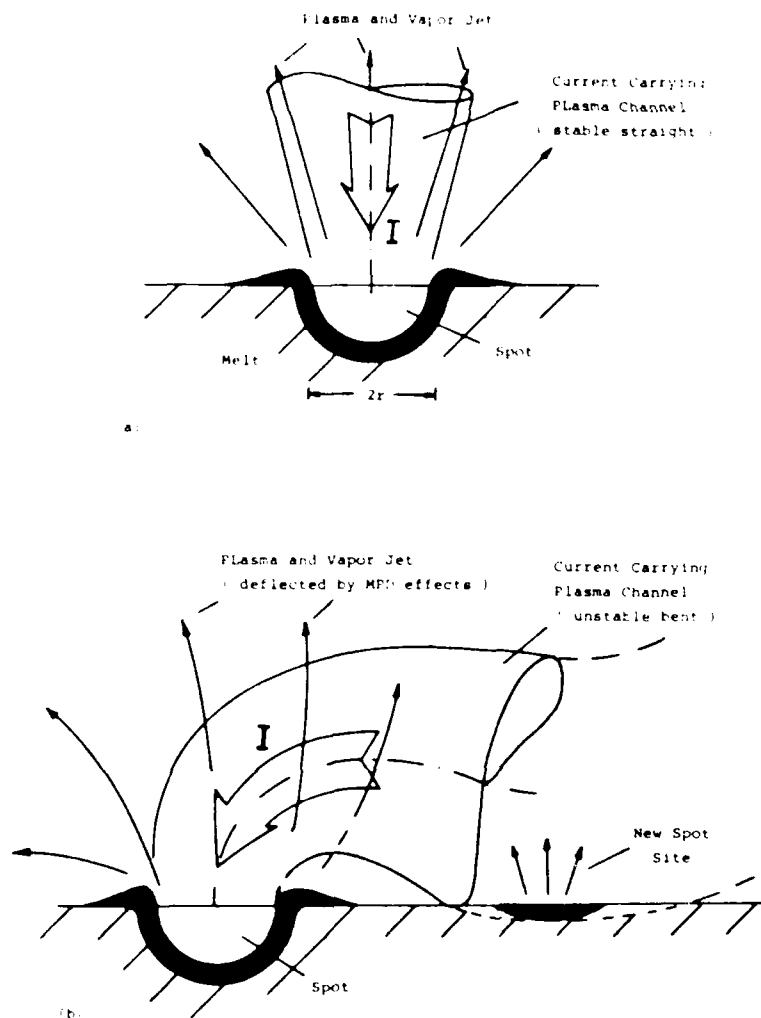


Fig. 65 Straight stable (a) and bent unstable (b) current-carrying plasma channel which emanates from a cathode spot.

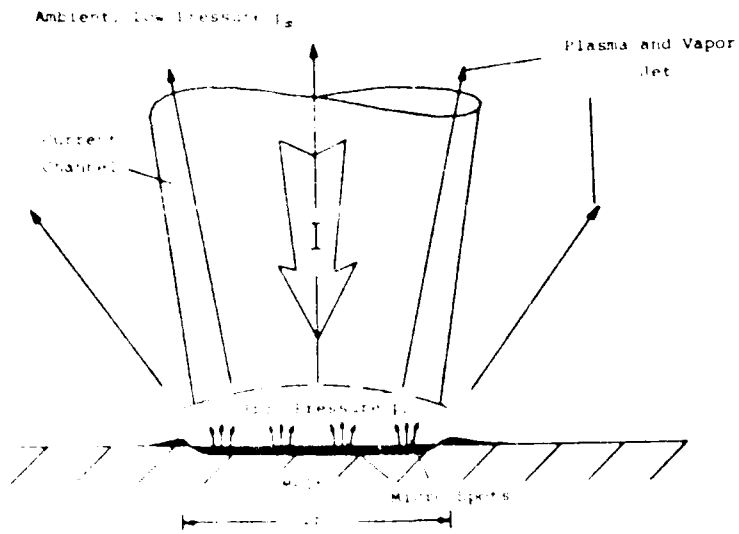


Fig. 66 Clustered spot.

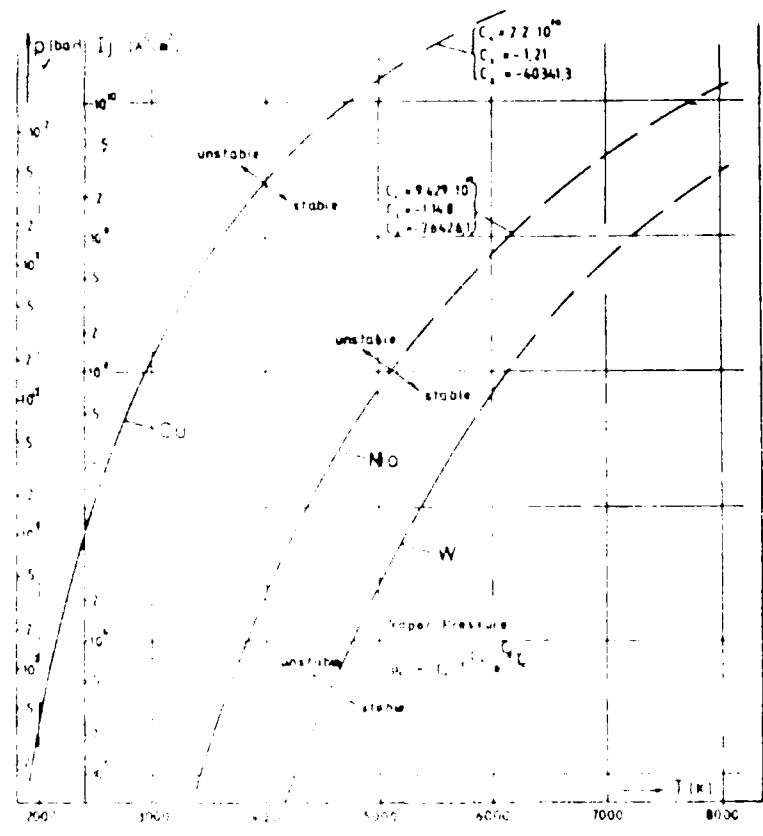


Fig. 67 Dependence of critical quantity  $I_c$  which can be carried by one spot on different electrode materials.

The current density within this channel is, as we have seen, quite high so that electromagnetic forces cannot be neglected. As it has been shown elsewhere<sup>43, 44</sup> such a current-carrying plasma channel with an axial flow is only straight and stable if the pressure difference between the plasma and vapor pressure  $p_v$  at the inner crater surface and the ambient pressure  $p_\infty$  is larger than (about) three times the average magnetic pressure. A more detailed investigation shows that this factor is about 3.0 for an almost flat crater (Fig. 66); for a hemispherical crater (Fig. 65a) it is about 3.3. The mathematical criterion for a stable straight discharge channel emanating from an active cathode spot follows therefore by

$$p_v - p_\infty > k \frac{\mu_0}{8\pi} I_s j_s \quad (7)$$

where  $3 \leq k \leq 3.3$ ,  $\mu_0 = 4\pi \cdot 10^{-7}$  Vs/Am (the magnetic permeability),  $I_s$  is the spot current and  $j_s$  is the average current density across the spot orifice. Since for any arc spot the ambient pressure  $p_\infty$  can be assumed small compared to the spot pressure  $p_v$  above the melt, the value of the product spot current times current density, at which a spot discharge goes from stable to unstable, can be directly related to  $p_v$ .

In Fig. 67, the vapor pressure curves or the spot conditions  $p_v$  and  $T_s$  for stable and unstable behavior on pure metal cathodes like copper molybdenum and tungsten are illustrated. Below these curves, a spot discharge is stable; above these curves it is unstable and cannot exist.

If the above criterion (7) is not fulfilled, any small disturbance leading to a minute curvature causes the current-carrying plasma channel to kink, i.e. the channel axis bends more and more and eventually the channel will come in contact with the cathode surface at a nearby site off the original spot (Fig. 65b). The new site will be heated up and a new current-carrying spot will be initiated. Again, for this new spot the stability requirement (7) must be fulfilled in order to maintain a stable and active discharge.

Thus, by increasing the arc current  $I$  higher and higher, one has to expect that more and more microspots are created, which now spread over the cathode surface and/or cluster together as larger spots. The clustered or larger spots can now have features similar to the microspots. Again, a plasma and vapor jet will propagate from a clustered spot (Fig. 66), and for the main current-carrying channel which emanates from this larger spot site, the same stability criteria (7) as derived for the microspot is now applicable. One therefore may state that the requirement (7) is valid very generally for any stable type of cathode spot. For the clustered or larger spots, however, their total spot current,  $I_S$ , will be larger, while the average current density,  $j_S$ , becomes smaller than in the case of a microspot.

The vapor pressure above the melt  $p_v$  in requirement (7) can now be related to the evaporation rate and to the average surface temperature  $T_S$  of the spot. Hence, the stability criteria (7) can also be written in the form

$$\dot{m}_{vS} \geq \frac{M}{4\pi \sqrt{2} k R T_S} I_S^2 g k \left( 1 + \frac{p_v}{p_0} \right) \quad (8)$$

$$k \frac{M}{8\pi} I_S j_S$$

where  $\dot{m}_{vS}$  is the amount of material, evaporated per second, of the spot,  $M$  is the molecular or atomic weight of the vapor,  $R$  is the universal gas constant and  $g$ , like  $k$ , is a geometric factor which now reads  $g = k_1 \sqrt{2}$  and  $g = 2$  depending on the presence of a flat surface. The value of  $k_1$  is given by eq. (65) for a spot profile. Since the minimum vapor pressure  $p_v$  is not as large as the ambient pressure  $p_0$ ,  $p_v/p_0$  is small. We practically by definition of a stable spot  $p_v/p_0$  is essentially constant, one can neglect  $p_v/p_0$  in eq. (8) and obtain  $\dot{m}_{vS} \geq \frac{M}{4\pi \sqrt{2} k R T_S} I_S^2 g k$  and can obtain  $\dot{m}_{vS} \geq \frac{M}{4\pi \sqrt{2} k R T_S} I_S^2 g k$ .

$$\dot{m}_{vS} \geq \frac{M}{4\pi \sqrt{2} k R T_S} I_S^2 g k \quad (9)$$

where  $\dot{m}_{vS}$  is the amount of material, evaporated per second, of the spot,  $M$  is the molecular or atomic weight of the vapor,  $R$  is the universal gas constant and  $g$ , like  $k$ , is a geometric factor which now reads  $g = k_1 \sqrt{2}$  and  $g = 2$  depending on the presence of a flat surface. The value of  $k_1$  is given by eq. (65) for a spot profile.

one. A spot discharge therefore always requires a minimum evaporation rate  $\dot{m}_{vS,\min}$ , which is proportional to the square root of the molecular or atomic weight  $M$  of the evaporated cathode material and inversely proportional to the square root of the melted spot surface temperature,  $T_S$ . If the cathode attachment consists of  $n$  individual spots identified by the indices  $1, 2, \dots, i, \dots, n$ , the overall minimum evaporation rate follows by

$$\dot{m}_{v,\min} = \sum_{i=1}^n \dot{m}_{vi,\min} = c \sum_{i=1}^n \sqrt{\frac{M}{T_{Si}}} I_{Si}^2 \quad (10)$$

and since the total current  $I$  is given by the sum over all spot currents  $I_{Si}$ , the overall minimum erosion rate due to evaporation,  $\epsilon_{v,\min}$ , is by definition

$$\epsilon_{v,\min} = \frac{\dot{m}_{v,\min}}{I} = c \frac{\sum_{i=1}^n \sqrt{\frac{M}{T_{Si}}} I_{Si}^2}{\sum_{i=1}^n I_{Si}} \quad [\text{kg/C}]. \quad (11)$$

It is of interest to note that according to eq. 11 the spots with relatively high individual current rates ( $I_{Si}$  large), i.e. the clustered spots, contribute the major amount of erosion, and that the erosion rate is about proportional to the spot current of those spots. If the cathode attachment consists only of many identical microspots with the same average spot current,  $I_{Si} = I_S = \text{const}$ , and the same average surface temperature  $T_{Si} = T_S = \text{const}$ , the overall erosion rate becomes independent of the number of spots and reduces to

$$\epsilon_{v,\min} = c \sqrt{\frac{M}{T_S}} I_S \quad [\text{kg/C}]. \quad (12)$$

The smaller therefore the spot current, the smaller the erosion rate. This does not mean that the overall arc current must be small, but rather that the number of spots are large.



Similar conditions must exist now on the tungsten cathodes of pulsed thrusters, since during the short discharge the cathode does not heat up to thermionic temperatures. Again, spots are present, and since the measured erosion rate is of about the same amount (14  $\mu\text{g}/\text{C}$ ) and the spot temperature,  $T_s$ , must be taken about the same (since the dissipation mechanisms within spots of the same erosion rate are the same), the spot current amounts again to about 135 A or to 27 A with a droplet loss factor of 5. At the current maximum of 8000 A, the number of spots are therefore between 60 and 300. Since the conditions in all these spots vary slightly, they are not stable but should rather jump according to the following explanation. If for instance the plasma pressure within a spot increases slightly, the Debye length and therefore the electric resistance of the spot decreases. According to Kirchhoff's distribution law, the current will be concentrated through that circuit of lowest resistance-- in our case through the spot of lowest resistance. That means, however, that for this spot the right side of the stability requirement (7), (8) or (9) increases faster than the left side. The consequence will be that the discharge channel above the spot will become unstable and, hence, causes a splitting or a jump to a new spot site. The spots are therefore distributed and may jump over the cathode surface, but according to inhomogeneities of the cathode surface and of the surface cooling, as well as the entire arc shape, they will prefer to appear on certain favorable, still hard to predict areas.

Today the interdependence of all these effects and also that about spots are still not well understood. Therefore a sound prediction of spot clustering and the erosion effects on cold cathodes are still not possible and need to be further investigated. The fact that in the Japanese experiments<sup>1,2</sup> the erosion rate is smaller than in ours, can be explained by a smaller average spot current and a larger number of spots.

The cathode tip is first attached to the jet when the thoriated tip is in the jet and is heated in and the tip begins to glow red. The cathode is then heated and krille,<sup>11</sup> who experimentally investigated the cathode type at cathode attachment under similar conditions, has shown that for the MPI thruster, the maximum temperature of the cathode tip is about 3200 K in argon and the maximum current density varies between about  $2.5 \cdot 10^7$  A/m<sup>2</sup> and  $10^8$  A/m<sup>2</sup> in ambient argon pressure of 20 Torr ( $2.67 \cdot 10^{-2}$  bar) and  $10^{-2}$  Torr ( $1.33 \cdot 10^{-3}$  bar), respectively. Since the maximum temperature does not change very much with the current density, we can estimate the evaporation rate by

$$j = \frac{M}{4\pi r^2} \sqrt{\frac{2\pi}{m}} \exp\left(-\frac{W}{kT}\right) \quad (13)$$

where  $j$  is the current density,  $M$  is the atomic weight of the cathode material,  $r$  is the radius of the cathode tip,  $W$  is the work function,  $m$  is the mass of the cathode material,  $k$  is Boltzmann's constant, and  $T$  is the temperature of the cathode tip. The evaporation rate of the cathode tip is then given by  $j = 4\pi r^2 j$ .

$$j = \frac{M}{4\pi r^2} \sqrt{\frac{2\pi}{m}} \exp\left(-\frac{W}{kT}\right) \quad (14)$$

where  $j$  is the current density,  $M$  is the atomic weight of the cathode material,  $r$  is the radius of the cathode tip,  $W$  is the work function,  $m$  is the mass of the cathode material,  $k$  is Boltzmann's constant, and  $T$  is the temperature of the cathode tip. The evaporation rate of the cathode tip is then given by  $j = 4\pi r^2 j$ .

The current density on a thermionically emitting cathode surface is governed by the Richardson equation

$$j = A_0 T^2 e^{-\phi/kT} \quad [A/m^2] \quad (15)$$

where  $A_0$  is the Richardson constant,  $\phi$  is the electron work function and  $k$  is the Boltzmann constant. Hence, with increasing surface temperature, the current density increases rapidly. Assuming now that within the diffuse attachment area, due to small fluctuations, the temperature on one spot would increase only slightly above the proper value, the current density would increase in this spot, and along with the current density, due to ohmic heating, the temperature would also increase, and so on. According to Kirchhoff's distribution law, the current would be more and more concentrated until field emission sets in and self-magnetic field effects play a role. In that case, however, the above spot theory becomes applicable.

Erosion rate ( $\mu g/cm^2$ )	Erosion rate		Erosion rate (spot)	
	$j_s$ (A/cm <sup>2</sup> )	$p_s$ (AT)	$j_s$ (A/cm <sup>2</sup> )	$p_s$ (AT)
0.031	1.4	1.4	1.4	1.4
0.031	1.4	1.4	1.4	1.4
0.031	1.4	1.4	1.4	1.4
0.031	1.4	1.4	1.4	1.4
0.031	1.4	1.4	1.4	1.4
0.031	1.4	1.4	1.4	1.4

Table 1. Listings of pertinent quantities such as spot temperature  $T_s$ , spot pressure  $p_s$ , spot current  $I_s$  and spot current densities  $j_s$ , which yield the same erosion rate of 0.031  $\mu g/cm^2$ .

It is obvious that the current flowing, seemingly continuous attachment, and erosion of the cathode, and a lot of spots of high current density, can still explain the measured erosion rate. According to eq. (11), for such a spotty attachment the overall erosion rate depends only on the individual spot current and the spot temperature. In Table I for typical hemispherical and flat spots, several pertinent spot currents,  $I_s$ , and spot temperatures,  $T_s$ , together with the vapor pressure and current density values, are listed, which all yield the same erosion rate of  $0.3 \text{ g/hr}$ .

As previously shown, these extremely high current densities of up to  $10^7 \text{ amp/cm}^2$  and even  $10^8 \text{ A/cm}^2$  can be explained by field emission but not by thermionic emission. The spot current amounts to between 1.5 and about 0.3 A; therefore the number of spots for a 100 A arc lies between 1000 and 10,000 spots. Despite their relatively large number, these spots cover only about a thousandth or 0.1% and even less of the entire glowing cathode area.

#### Summary

The results of the present study of the general method of erosion measurement are summarized in Table II. The present method of erosion measurement is based on the assumption that the erosion rate is proportional to the square of the spot current, the erosion rate is proportional to the square of the spot current, the time interval between two successive erosion measurements is constant, and the erosion rate is proportional to the square of the spot current. However, the present method is based on the assumption that the erosion rate is proportional to the square of the spot current, the erosion rate is proportional to the square of the spot current, the time interval between two successive erosion measurements is constant, and the erosion rate is proportional to the square of the spot current.

As a result of the present study, it is concluded that the erosion rate is proportional to the square of the spot current, the erosion rate is proportional to the square of the spot current, the time interval between two successive erosion measurements is constant, and the erosion rate is proportional to the square of the spot current.

channel to touch the cathode in the vicinity of the spot and eventually leads to a new spot site. This effect causes the spot to split and/or to move discontinuously over the surface. These spots can now cluster together to form more stationary larger ones, which leads to an enhanced erosion. It is shown that the smallest possible overall erosion rate is directly proportional to the spot current and that it is not necessarily a function of the arc current. Therefore, in order to avoid a high erosion rate, the number of spots should be high, while the average spot current should be small. The relatively high cathode erosion rates measured with the pulsed and during the starting phase of the continuous MPD-arc thruster are explained by spots which carry a current of about 30 to 160 A.

The processes occurring on a glowing cathode surface of a steady state continuous MPD-arc device are discussed and, based on data in the literature, the expected erosion rate determined. Since such a seemingly diffuse thermionic attachment is obviously unstable, it is suggested that this so-called thermionically emitting cathode also consists of many tiny hot spots in which field emission is predominant.

## 5. Numerical Modeling of the Flow Discharge in MPD Thrusters

### 5.1 Introduction

The increase in onboard electrical power in the near future is again raising interest in self-field MPD thrusters. Despite their simplicity in design and power conditioning, they are handicapped even today by the shortcomings of low efficiency and a performance limit known as "onset" which restricts the flow rate at a given current value. Therefore, since the beginning of the design and investigation of self-field MPD thrusters at the end of the sixties, effort has been made to understand the physics of the MPD discharge and the development of appropriate codes. But the MPD problems cannot be solved easily, because in contrast to the hardware simplicity of these devices, the physics involved are of extreme complexity. To mention only a few: real gas effects, i.e. cold propellant is heated up in an arc and the gas has to be dissociated and ionized; the problems related with the electrodes are only partly known or solved; the plasma is in a thermal non-equilibrium; because of the low densities and high temperatures the Reynold's numbers are low and the friction cannot be neglected; the magnetic Reynold's number is too high to separate flow and discharge; etc. This list is by no means a complete one. Added to these physical complexities are numerical difficulties: the necessary coupling of different partial differential equation systems, namely elliptical and hyperbolic ones; non-linearities; steep gradients; and so on. And let us not forget difficult geometries. Therefore, due to the great complexity of the physical conditions, for all codes established to solve at least parts of these problems, many and great simplifications must be made. The resulting codes include for example one-dimensional,<sup>13, 47</sup> quasi-two-dimensional and simplified two-dimensional ones.<sup>13, 48-51</sup>

In this chapter, further approaches are presented: first, the approach of Hügel<sup>10</sup> has been modified and used for different nozzle angles for nozzle-type thrusters. Second, a partly two-dimensional, more refined code has been developed. The simplified two-dimensional electromagnetic calculation follows from

Ohm's law, similar to Ref. 49, and the flow is modeled by a one-dimensional, non-equilibrium expansion. The equations are solved only for the steady phase. The third approach uses comparable electromagnetic equations, but models the flow actually two-dimensionally with a modified MacCormack code. All three approaches neglect electrode effects and friction.

### 5.2 Adaptation of the Semi-Empirical Hgel Calculation Method to Include Different Geometries

In Ref. 10 Hgel developed a magnetofluiddynamic model which he used to explain the nature of the discharge instabilities setting in at the so-called critical value of  $I^2/m$ . In this model (Fig. 68), the similarity between the measured flow field with a spatial source flow field is used to establish a computational code to resolve the midstream flow in a quasi-two-dimensional manner. As a further assumption, the magnetic Reynolds number is taken as low, i.e.  $Rm < 1$ . In such a case, it is possible to determine the electromagnetic field separately from the flow field, whereas its effect upon the latter is still explicitly taken into account via force and heating terms in the momentum and energy equations. As a first step, then, the distribution of



Fig. 68 Model geometry for the theoretical description in comparison with experimental device.

current density and magnetic field is calculated by using potential theory and Maxwell's equations and by introducing a stream function  $\psi$ . The electrode geometry and the current distributions on the electrodes, needed as boundary conditions for the solution of the partial differential equation for  $\psi$ , are taken from the experiments. Good agreement between calculated and measured current distributions justifies this procedure.

Hence, from the usual set of basic equations, i.e. state, continuity, momentum, energy, and Ohm's law, a system of partial differential equations for the flow properties is obtained. Joule heating and electromagnetic forces are included, whereas heat conduction, radiation, and viscous effects are neglected. In particular, the results of that model indicated a reduction of the pressure at the anode wall with increasing  $I/\dot{m}$ . The value at which the pressure approached zero agreed well with the experimentally observed value. Although a wide variety of parameters had been investigated, both experimentally and theoretically, the geometry of the thruster had never been altered. Hence, it appeared necessary to also cover this aspect in the research work.

Along this line, then, a study was made to prove whether this magnetofluiddynamic model could be used as an appropriate tool for parametric and predictive calculations.<sup>12</sup> Thereby, the main goal was to investigate the effect of the opening angle of the thruster's cone nozzle upon the critical conditions and the achievable thrust.

The original model was changed to omit some simplifications applied in the mathematic treatment of the cone geometry. In particular, when calculating volume elements, stream functions and electromagnetic forces small-angle-approximations when using goniometric functions were replaced by the exact expressions. In Fig. 69, computed values of the pressure at the anode are plotted as a function of the correlation parameter  $I/\dot{m}$  for different mass flows and opening angles. The pressure at the anode decreases with increasing  $I/\dot{m}$  until it reaches zero at some

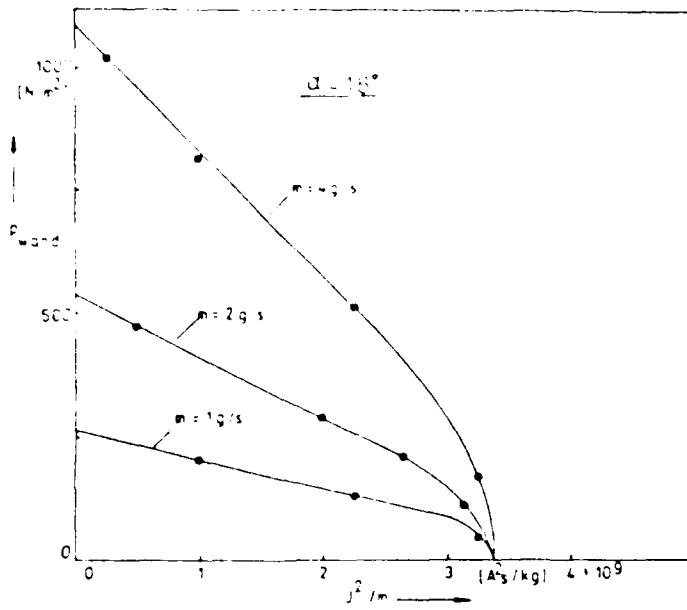
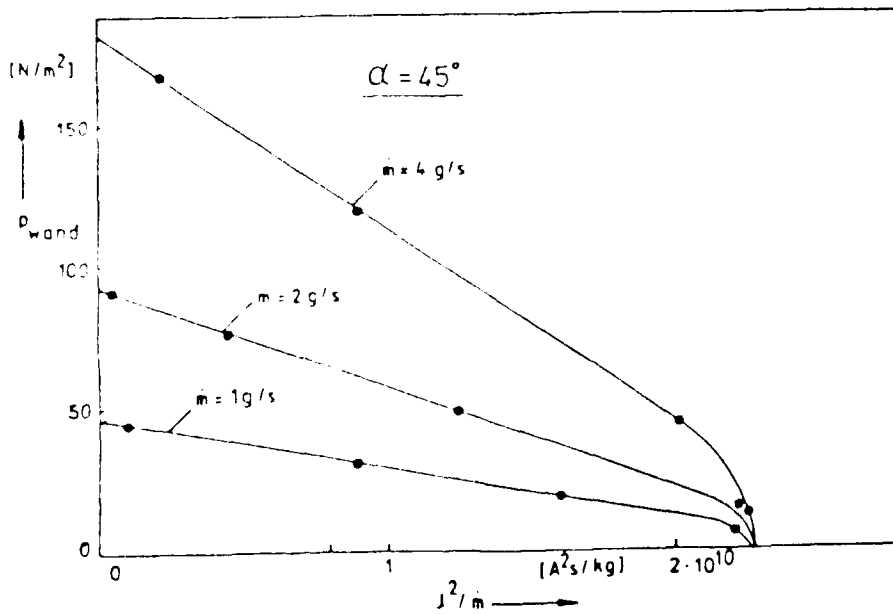
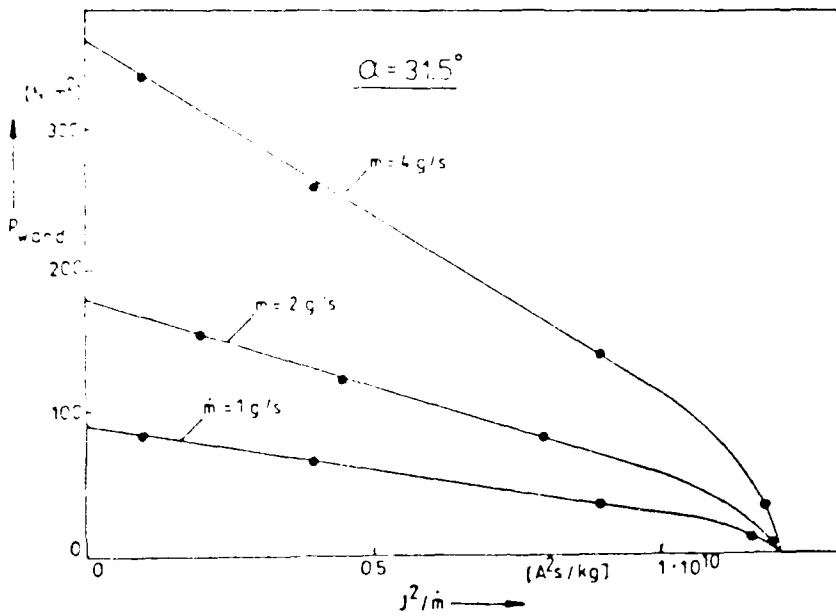


Fig. 69 Pressure at the anode tip as a function of  $I^2/\dot{m}$  for several mass flows and opening angles  $\alpha$ .



"critical" condition. Clearly, this appears as a consequence of the fact, that with increasing  $I/\dot{m}$  the self-magnetic forces lead to a steepening pressure profile over the cross section. Note that  $(I^2/\dot{m})_{crit}$  is the same for all values of  $m$ .

The effect of the opening angle upon the critical value  $(I^2/\dot{m})_{crit}$  is summarized in Fig. 70. It appears that some asymptotic value of about  $4 \cdot 10^{10} \text{ As}^2/\text{kg}$  is reached. From these results, it should be advantageous to use thrusters with large opening angles.

However, of much more interest is the thrust that can be achieved at the corresponding conditions. Or more precisely, can one expect an increase in specific impulse? In Fig. 71, the calculated thrust at constant mass flow rate is shown as a function of current and opening angle. The dashed curve represents the limits imposed by reaching the critical values of  $I^2/\dot{m}$ . The dashed curve "36° exp" show the experimental results for the case of an opening angle of 36° (Stuttgart thruster) which coincide quite well with the calculated values. There is strong evidence that the specific impulse rather decreases than rises with increasing angle.

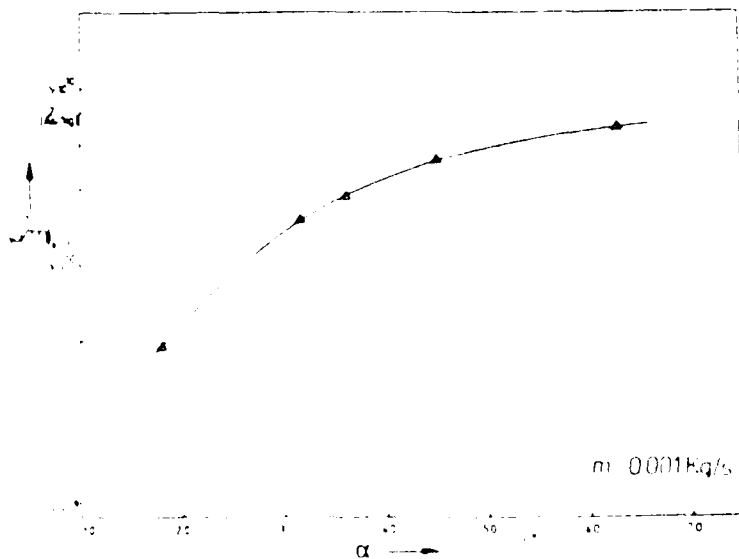


Fig. 70. Critical criterion as a function of the opening angle.

However, before drawing final conclusions, one must recall the many assumptions that had to be made in order to obtain the analytical model of Ref. 10. For example, according to the original procedure, the attainable thrust for  $63^\circ$  would be slightly below the electromagnetic component  $S_M$ . This fact might be an indication of inherent limitations of the model itself or its validity for describing extreme geometries. Hence, the question as to the optimum opening angle for a nozzle-type thruster appears not to be answered yet.

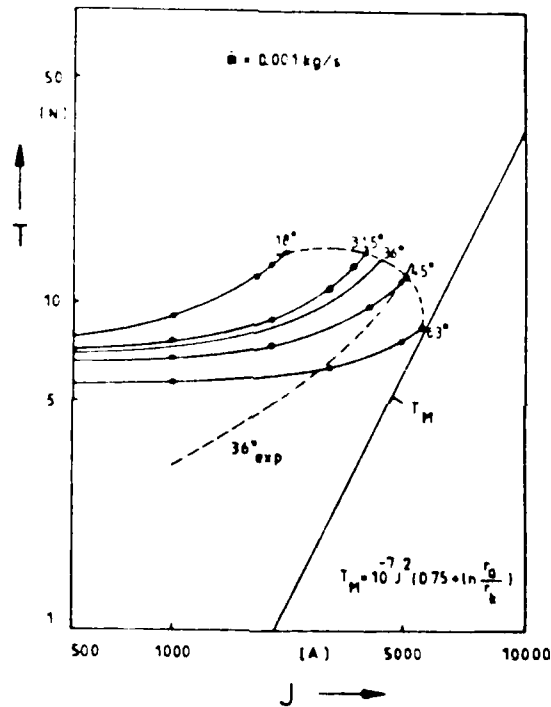


Fig. 71 Calculated thrust as a function of current with the opening angle  $\alpha$  as parameter and with the experimental results for  $\alpha = 36^\circ$  as comparison.

### 5.3 Steady-State MPD Thruster Investigations

In order to predict the overall performance of continuously running, self-field MPD thrusters, a semi-two-dimensional model calculation and computer program has been developed.<sup>3</sup> In a first step this program has been used to investigate the current contour lines and the thrust within the nozzle-type thruster DT2 (Fig. 3).

#### Current Contour Lines

In this approach, the current contour lines are calculated in  $r$ - and  $z$ - dependence while the flow field is taken as a one-dimensional, frictionless expansion flow, assuming isothermal behavior for the electron component and isentropic expansion for the heavy particles like ions and neutrals. This assumption is justified, since primarily the electron component is heated by Ohmic energy input, and since within the nozzle expansion flow the energy exchange between the lightweight electrons and the heavy particles like ions and neutrals is fairly weak. Therefore, reaction collisions (ionization and recombination processes, etc.) are neglected. Hence, the model approach distinguishes between electron and heavy particle temperatures and assumes a frozen flow from the nozzle throat on downstream.

Within the nozzle throat, one assumes a "fully developed" arc flow regime, i.e. the gas and plasma velocity and the current density vector have only an axial component and the arc column is defined by only radial heat transfer (and possibly by radial radiation) losses. Moreover, from the nozzle throat on upstream, one no longer distinguishes between electron and heavy particle temperatures, since within this higher pressure regime a tight coupling between all components is more likely to be established than in the low pressure downstream nozzle regime. In spite of the neglect of the radial dependency of the flow and species temperatures, however, this model approach turns out to be an effective tool for predicting the current contour lines within and the thrust and specific impulse of a nozzle-type self-field MPD thruster.

Assumptions:

- steady state conditions
- rotational symmetry
- no azimuthal current
- singly ionized, quasi-neutral plasma
- electric current density normal to electrode surfaces
- from cathode to nozzle throat: thermal equilibrium
- within the nozzle: frozen flow, ambipolar expansion flow without friction, electrons: isothermal, ions: adiabatic
- outside the nozzle: hyperbolic expansion flow, electrons and ions adiabatic

Basic Equations:

Maxwell's eqs.:

$$\vec{\nabla} \times \vec{B} = \mu_0 \vec{j} \quad (16)$$

$$\vec{\nabla} \times \vec{E} = - \frac{\partial \vec{B}}{\partial t} = 0 \quad (17)$$

$$\vec{\nabla} \cdot \vec{B} = 0 \quad (18)$$

$$\vec{\nabla} \cdot \vec{E} = 0 \quad (19)$$

Ohm's Law:

$$\vec{j} = \sigma \{ \vec{E} + \vec{v} \times \vec{B} \} - \frac{\omega \tau}{B} [ \vec{j} \times \vec{B} ] \quad (20)$$

Equation of State:

$$p = \rho \frac{k}{m_0} T_t \left\{ 1 + \left( \frac{\rho}{\rho_0} \right)^{\kappa-1} \right\} \quad (21)$$

Continuity Equation:

$$\rho v A = \rho_t A_t v_t = \dot{m} \quad (22)$$

Expansion Relation:

$$\left(\frac{v}{v_t}\right)^2 = 1 + \ln \left| \frac{A}{A_t} \frac{v}{v_t} \right| + \frac{\kappa}{\kappa-1} \left[ 1 - \left( \frac{A_t}{A} \frac{v_t}{v} \right)^{\kappa-1} \right] + \frac{2}{\dot{m} v_t} \int_{z_t}^z \left( \frac{v}{v_t} \right) (\vec{j} \times \vec{B})_z A dz \quad (23)$$

Nozzle Throat Conditions:

$$v_t^2 = \left( \frac{\partial p}{\partial \rho} \right)_{t, \text{isoth}} = 2 \frac{\kappa}{m_0} T_t \quad (24)$$

$$T_t = T_e = f \cdot \left( \frac{I}{r_t} \right)^{2/5} \quad (25)$$

where  $f$  is a slowly varying function depending on current distribution.

The last three equations are derived in detail under the above assumptions in Ref. 4.

Rewriting Ohm's Law by means of Maxwell's equations, one obtains a vector equation for the magnetic induction vector  $\vec{B}$  in the form

$$-\frac{\partial \vec{B}}{\partial t} = \frac{1}{\mu_0} \text{rot} \left( \frac{1}{\sigma} \text{rot} \vec{B} \right) - \text{rot} [\vec{v} \times \vec{B}] + \frac{1}{\mu_0} \text{rot} [\beta (\text{rot} \vec{B}) \times \vec{B}] = 0 \quad (26)$$

with  $\beta = \frac{\partial t}{B_0} = \frac{1}{en_e} \quad (27)$

For a stream function

$$\Psi = rB_\theta$$

with respect to the rotational symmetry and the zero azimuthal current, the elliptic, partial differential equation of 2nd order follows from eq. (26) in the form

$$\begin{aligned} \frac{d^2 \psi}{dr^2} + \frac{d^2 \psi}{dz^2} - \frac{d\psi}{dr} \left( \frac{1}{r} + \frac{1}{\sigma} \frac{d\sigma}{dr} - \frac{\sigma \psi}{r^2} \frac{dB}{dz} + \sigma \mu_0 v_r \right) \\ - \frac{d\psi}{dz} \left( \frac{1}{\sigma} \frac{d\sigma}{dz} + \frac{\sigma \psi}{r} \frac{d\delta}{dr} - \frac{2\sigma r \Psi}{r^2} + \sigma \mu_0 v_z \right) \\ - \mu_0 \left( \frac{dv_r}{dr} r + \frac{dv_z}{dz} z - \frac{v_r}{r} \right) = 0 \end{aligned} \quad (28)$$

The function  $\psi(r, z) = \text{const.}$  represents now a current contour line, since  $B = B_0 \sim I(r)/r$  and  $I(r)$  is the electric current carried through a cross sectional area of  $\pi r^2$ . The proper boundary conditions for  $\psi$  follow from the geometry of the thruster walls and electrodes.

A solution of the equation system (16) - (28) requires as input data:

- Geometry of Thruster  $A(z)$
- Mass Flow Rate  $\dot{m}$
- Electric Current  $I$

and yields the following results:

- Current Contour Lines
- Thrust  $\hat{F}$
- Specific Impulse  $I_{sp}$

Step 1: By setting the integral

$$\int_{z_t}^z \frac{v}{v_t} \mathbf{j} \times \mathbf{B} \Big|_z A dz$$

in the expansion relation eq. (23) to zero, one obtains together with the nozzle throat conditions (24) and (25) a first approximation of  $v(z)$ ,  $p(z)$ ,  $\rho(z)$  and  $n_1(z) = n_0(z)$  within the nozzle. Outside the nozzle one assumes a hyperbolic expansion flow, which means  $v_r \neq 0$  (Fig. 72).

with the knowledge of the flow and plasma properties (in first approximation),  $\rho$ ,  $\beta$  and  $v$  are also known, as well as their derivatives. With these quantities one now solves the differential equation 28 by means of a finite differential method (Gauss-Seidel) for the current contour lines in first approximation. In Fig. 73 the current contour lines are shown for different currents between 1.3 and 4 kA. According to Maxwell's equation, one also obtains from  $\beta$  the current density and the  $\mathbf{j} \times \mathbf{B}$  force configuration within the discharge.

Step 2: One solves the expansion relation (eq. 23) numerically by taking  $(\mathbf{j} \times \mathbf{B})_z$  within the integral from Step 1. With that the velocity  $v(z)$  and the quantities  $p(z)$ ,  $\rho(z)$ ,  $n_p(z)$  are calculated in second order approximation and from that the new quantities for  $\rho$ ,  $\beta$  and  $v$  with their derivatives.

With these new quantities, one now solves the differential equation (28) for the current contour lines by means of the same numerical method as in Step 1. Repeating Step 2 yields an iterative solution of the equation system (16) - (25).

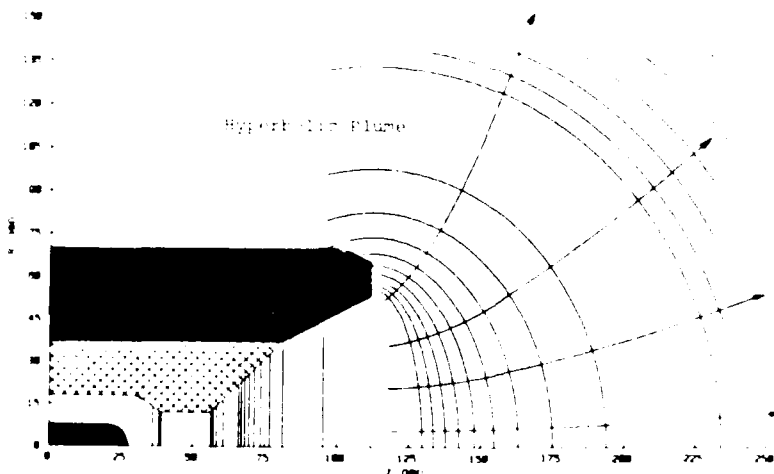


Fig. 72 Scheme of the density model. Inside the nozzle: one-dimensional. Outside the nozzle: elliptical.

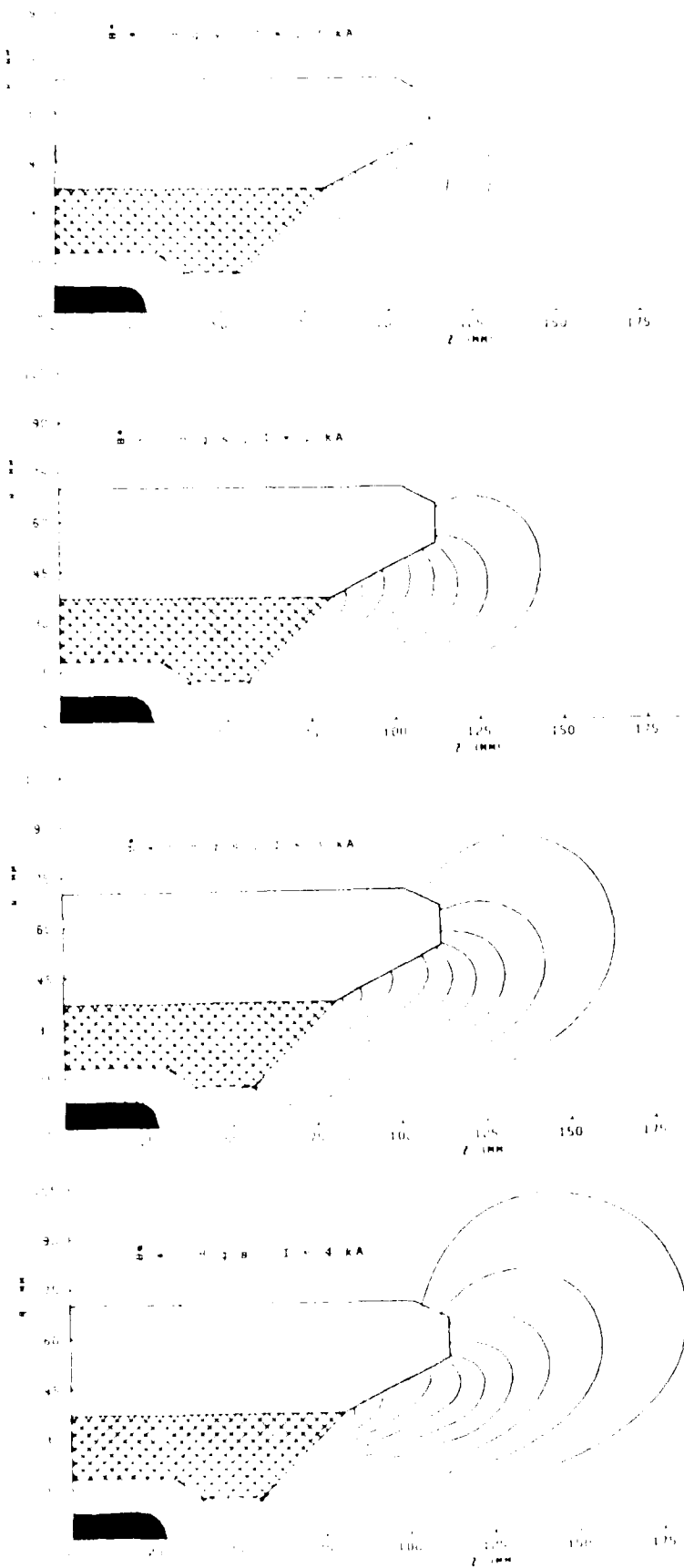


Fig. 73 Current contour lines for different currents with a mass flow of 0.8 g/s argon.

The calculation shows that after two steps the current contour lines with  $I = 4$  kA do not change anymore and even a first step approach gives good results. For lower current rates the deviation is even smaller.

A comparison between calculated and measured current pattern (Fig. 74) shows a fairly good agreement. The fact that in the measured case the anode attachment is more concentrated downstream of the nozzle end than in the calculated case may be attributed to the theoretical model which neglects the boundary layer along the nozzle and anode walls.

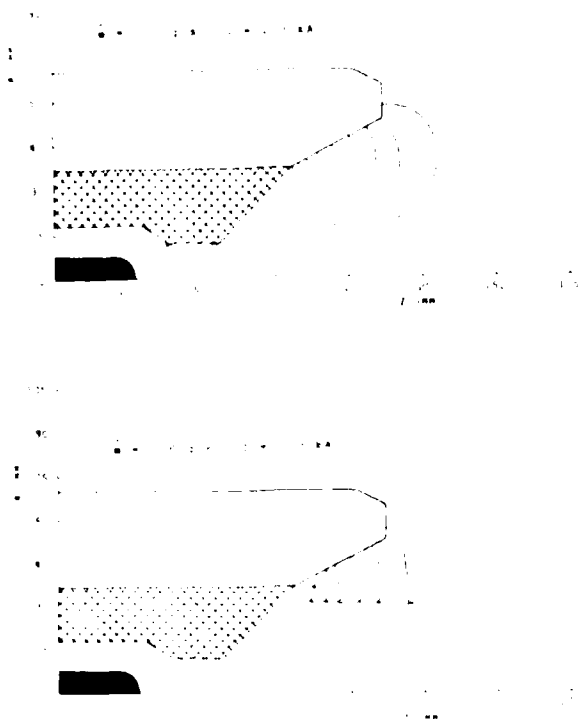


Fig. 74 a) calculated and b) measured current contour lines of the MPD discharge in the nozzle-type DT2-IRS thruster for  $I = 1.3$  kA and  $m = 0.8$  g/s argon.

Thrust

According to the known  $\vec{j} \times \vec{B}$  force configuration and the flow conditions, one can now calculate the thrust.

The thrust of a self-field MPD accelerator is composed of two effects; first the sum of all gas-dynamic surface forces on the inner plenum chamber and on the inner nozzle wall, and second the sum of all volume effects given by the magnetic field forces which act between the current-carrying plasma and the entire power circuit, including the coaxial electrodes. Hence it is

$$\vec{F} = \int_{A_S} (\rho \vec{v}\vec{v} + \vec{P}) \cdot d\vec{A} - \int_V \vec{j} \times \vec{B} \, dV \quad (29a)$$

$$= c_T p_0 A_t - \int_V \vec{j} \times \vec{B} \, dV \quad (29b)$$

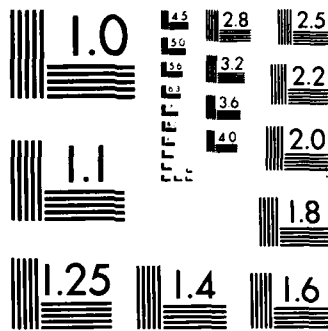
where  $\rho \vec{v}\vec{v} + \vec{P}$  is the gas dynamic force per unit area;  $A_S$  represents the surface of all internal walls like plenum chamber with the gas inlet cross sections, the cathode surface and the inner solid wall of the nozzle;  $V$  is the current-carrying volume. The second term is the sum over all  $\vec{j} \times \vec{B}$  forces which act between the current-carrying solid leads of the electric power circuit and the current-carrying plasma; in the second equation  $p_0$  is the chamber pressure,  $A_t$  the nozzle throat area and  $c_{Tn}$  the thrust coefficient matching the gas dynamic effects. It is by definition

$$c_T = \frac{1}{p_0 A_t} \int_{A_S} (\rho \vec{v}\vec{v} + \vec{P}) \cdot d\vec{A} \quad (30)$$

The calculated thrust, based on the current density and magnetic field determined with the procedure as described in the section "Current Contour Lines", is now compared with the experimental results in Fig. 75.

They show excellent agreement for  $c_T$  with the experimental measurements in the upper current range. For currents going down to 1300 A the deviation is less than 10%. The magnetic thrust is given by the lower curve. It can be seen that the electromagnetic thrust is about 1/3 of the total thrust at a current of about 1400 A.





MICROCOPY RESOLUTION TEST CHART  
NATIONAL BUREAU OF STANDARDS-1963-A

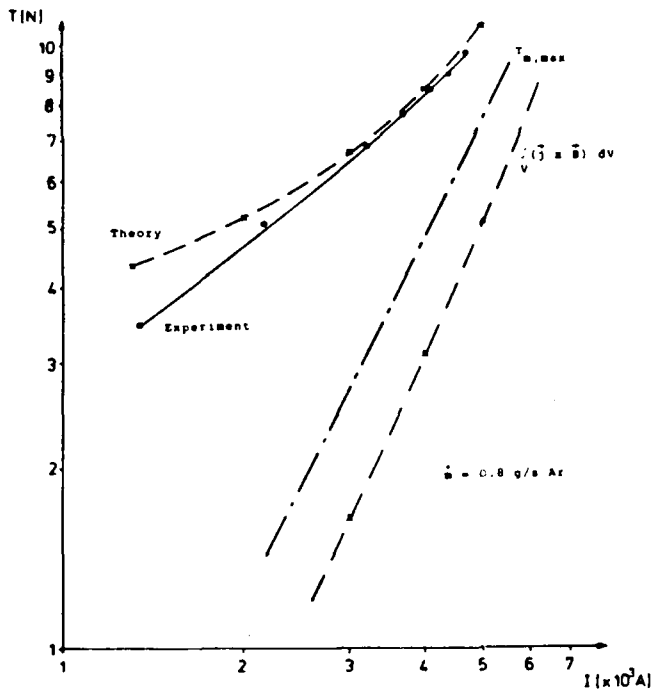


Fig. 75 Comparison between calculated and measured thrust of the DT2-IRS thruster.  $T_{m,max}$  is the maximum possible electromagnetic thrust.

### 5.4 Time Dependent, Two-Dimensional MPD Thruster Investigations

In addition to the steady state MPD theory, a real two-dimensional numerical code has been developed.<sup>54</sup> This code allows the calculation of the time dependent plasma properties during the starting phase of steady state MPD thrusters, as well as for pulsed mode thrusters. The numerical solution is done in a manner similar to that of Jacobi<sup>55</sup> for laser applications. In a first approach, this MPD code was applied to the cylindrical MPD thruster ZT1 being developed at this institute. Fig. 76 shows the drawing of ZT1, and Fig. 77 shows the corresponding simplified scheme for the calculation.

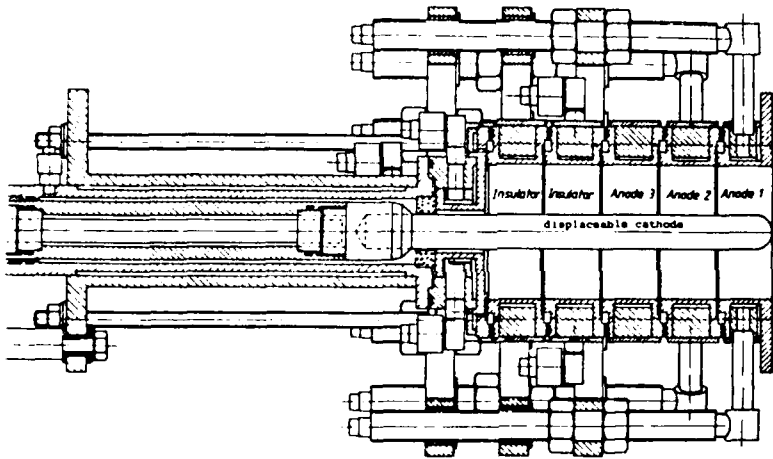


Fig. 76 Cylindrical continuous MPD thruster ZT1-IRS.

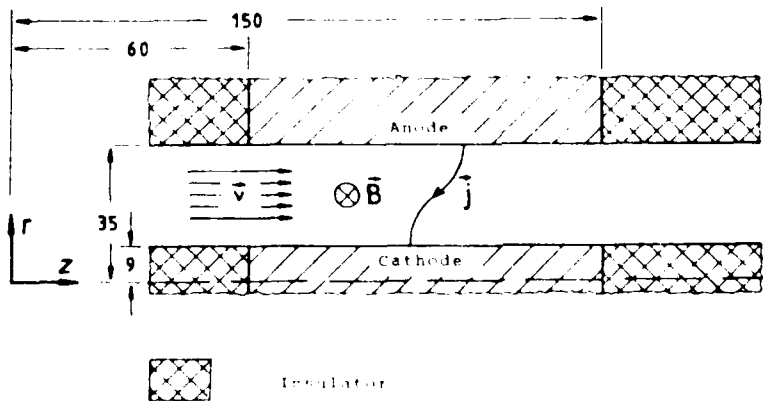


Fig. 77 Simplified scheme used for the calculation.

The geometrical configuration on which the computation is based was chosen as close as possible to the experimental device. The radii of cathode and anode are taken according to the dimensions of the real device; however, the length of the cathode is assumed to be of the same length as the anode and it matches the length of the three anode segments (see Fig. 76). The model is assumed to be an infinite tube of an insulator with a central insulating rod, only the electrodes will be of zero resistance.

For the time dependent calculation of the MPD flow, two independent codes were correlated to determine flow field, current and magnetic field distribution. These two codes are connected in the following manner: for a given flow field, the current, and hence the magnetic field distribution, was determined. With these results the flow field equations were integrated. In the next time step, this new flow field and the new distribution of the thermal properties were taken to calculate the new electromagnetic field distribution, and so on.

As input data the two codes require:

- geometry of the thruster
- mass flow rate
- electric current as a function of time

and at the starting point:

- temperature field
- Mach number.

This yields the following time dependent results:

- flow
- temperature
- pressure
- Mach number
- magnetic field
- current density distribution within the channel
- electrothermal thrust.

### Electromagnetic Code

The electromagnetic properties are obtained in a similar manner as from the steady state thruster code, using the following assumptions:

- rotational symmetry
- no azimuthal current
- electric field normal to the electrode surfaces.

One solves Ohm's law with respect to Maxwell's equations; this means one must solve the elliptic partial differential equation 28.

The boundary conditions are as follows:

On the insulator surface and at the boundary of the integration area, the stream function  $\Psi$  equals zero for the case of the downstream insulator and equals  $\Psi_{\max}$  for the upstream insulator. At the electrodes the boundary condition follows from the requirement that the electric field  $\vec{E}$  must be perpendicular to the surface. This means for a cylindrical channel as considered here that at the electrode surfaces  $E_z$  equals zero. Therefore, the boundary condition follows to

$$\frac{1}{\sigma\mu_0 r} \frac{\partial \Psi}{\partial r} - v_r \frac{\Psi}{r} - \frac{\beta \Psi}{\mu_0 r^2} \frac{\partial \Psi}{\partial z} = 0 \quad (31)$$

With this closed boundary condition, the computation was done with a Gauss-Seidel code and yields as a result the magnetic field and the current density distribution within the channel.

### Flow Field Code

For the description of the time-dependent, two-dimensional, supersonic, ohmically heated flow the conservation equations for mass, impulse and energy were used with the following assumptions:

- friction free flow
- rotational symmetry
- no azimuthal current and velocity
- supersonic flow within the channel

The conservation theorem formulation was chosen in order to satisfy the Rankin-Hugoniot shock conditions implicitly; hence the description of shock depth and shock velocity are very good. These considerations yield the following non-linear hyperbolic differential equation system with cylindrical coordinates

$$\begin{vmatrix} \rho \\ \rho v_r \\ \rho v_z \\ e \end{vmatrix}_t + \begin{vmatrix} \rho v_r \\ p + \rho v_r^2 \\ \rho v_r v_z \\ (p+e)v_r \end{vmatrix}_r + \begin{vmatrix} \rho v_z \\ \rho v_z v_r \\ p + \rho v_z^2 \\ (p+e)v_z \end{vmatrix}_z + \begin{vmatrix} \rho v_r / r \\ \rho v_r^2 / r - j_z \times B_\theta \\ \rho v_r v_z / r - j_r \times B_\theta \\ (p+e) \frac{v_r}{r} - j^2 / \sigma \end{vmatrix} = 0 \tag{32}$$

where the indices  $\|_t, \|_r, \|_z$  indicate the partial differentiation with respect to time and to the r- and z-directions.

**Boundary Conditions:**

- upstream: at that boundary all flow parameters are assumed to be constant and must be set.
- downstream: here the flow parameters are extrapolated because of the calculated field parameters.
- at the side: no normal velocity; normal differentiations equal zero.

**Initial conditions:**

- At  $t = 0$  the flow parameters equal the undisturbed parallel flow;
- uniform current density;
- Mach number and temperature must be set.

For the numerical solution a modified MacCormack code was used; this is an explicit code of second order which uses the shock capturing method. It allows a fairly high energy input into the flow due to ohmic heating and a steep rise in the impulse due to  $\vec{j} \times \vec{B}$  forces. Because of instabilities at the starting phase caused by initial and boundary conditions on the upstream boundary, the initial conditions will be restricted for the moment to values which result in cowling numbers smaller than 1.5 in the middle of the electrodes.

For the example presented, the calculation is based on the following initial values:  $T(0) = 8000$  K,  $Ma(0) = 1.2$ , with a mass flow of 20 g/s argon. The current as a function of time is taken as a sine square function  $\sin^2[\pi t/2t_0]$  rising from  $I(t=0) = 0$  to  $I(t_0=200\mu\text{s}) = 12$  kA and is taken as constant from there on.

With this input data the computation yields the time dependent current density distribution, as illustrated in Fig. 79.

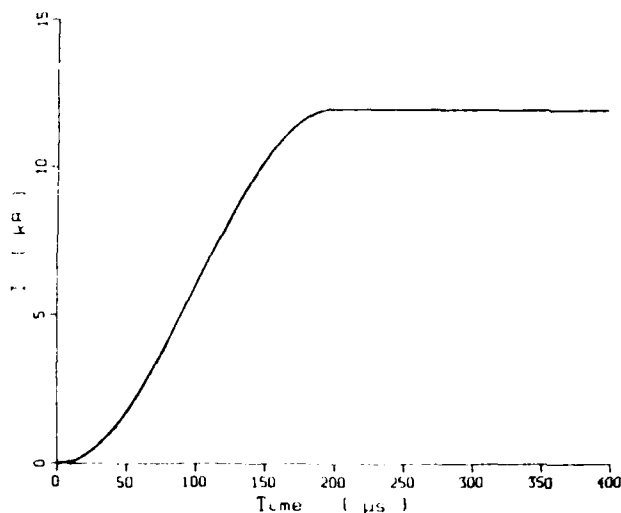


Fig. 78 Current curve versus time.

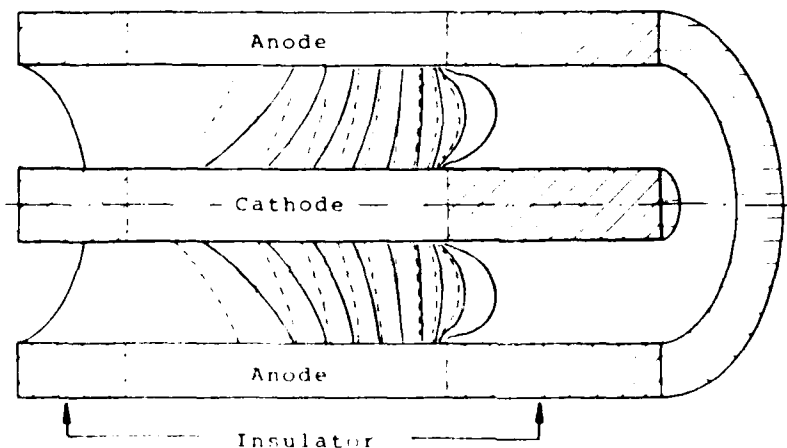


Fig. 79 Calculated current contour lines in a cylindrical MPD thruster. Dotted lines at  $t = 20 \mu\text{s}$ , dashed after  $160 \mu\text{s}$  and solid after  $200 \mu\text{s}$ .

Starting with radially parallel and homogeneous current contour lines at  $t = 0$ , the current is driven more and more downstream--stronger near the anode than at the cathode--and bulges at the electrode ends. The dotted lines are those at  $20 \mu\text{s}$  after starting, and the dashed and solid lines are for  $160 \mu\text{s}$  and  $200 \mu\text{s}$ , respectively.

Fig. 80 illustrates the temperature distribution  $100 \mu\text{s}$  and  $200 \mu\text{s}$  after starting. The strong rise in temperature near the electrode is caused by ohmic heating due to the relatively high current density there. The disturbance at the cathode end due to discontinuous boundary conditions decreases with time. This fairly marked disturbance at starting is one reason for choosing a high initial temperature.

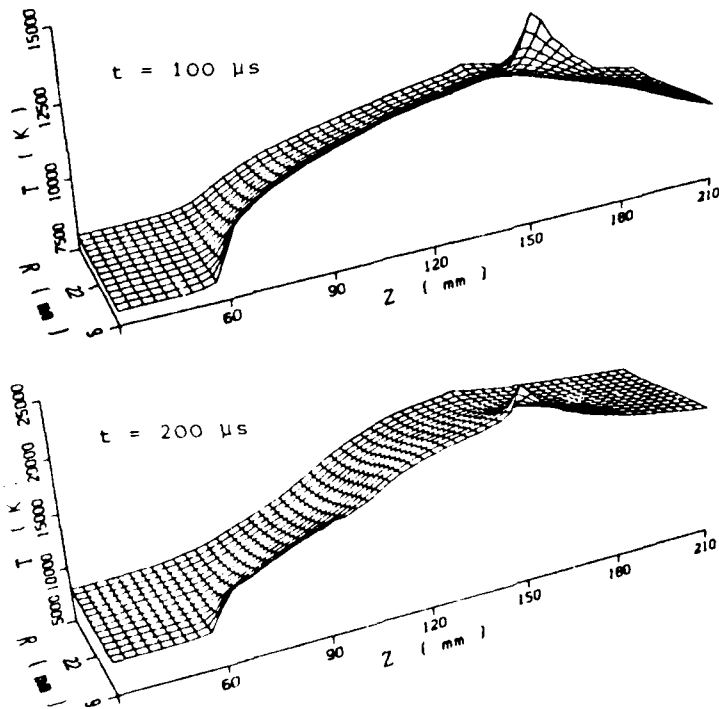


Fig. 80 Temperature distribution within the channel at a)  $100 \mu\text{s}$ , b)  $200 \mu\text{s}$ .

A radial shock front formed at the end of the electrodes moves upstream while lowering its intensity; this is demonstrated in Fig. 81.

The axial and radial velocity distribution at 200  $\mu$ s are plotted in Fig. 82. At both ends of the cathode there is a steep rise in the radial velocity  $v_r$ , while the axial velocity reaches its maximum at the beginning of the cathode. The axial velocity decreases towards the cathode end, with a low rise from this point downstream as well as towards the anode.

The relationship of the Mach number distribution to the temperature and velocity distribution at 200  $\mu$ s is shown in Fig. 83. The Mach number set equal to 1.2 at the upstream boundary reaches an initial maximum at the beginning of the cathode, rises

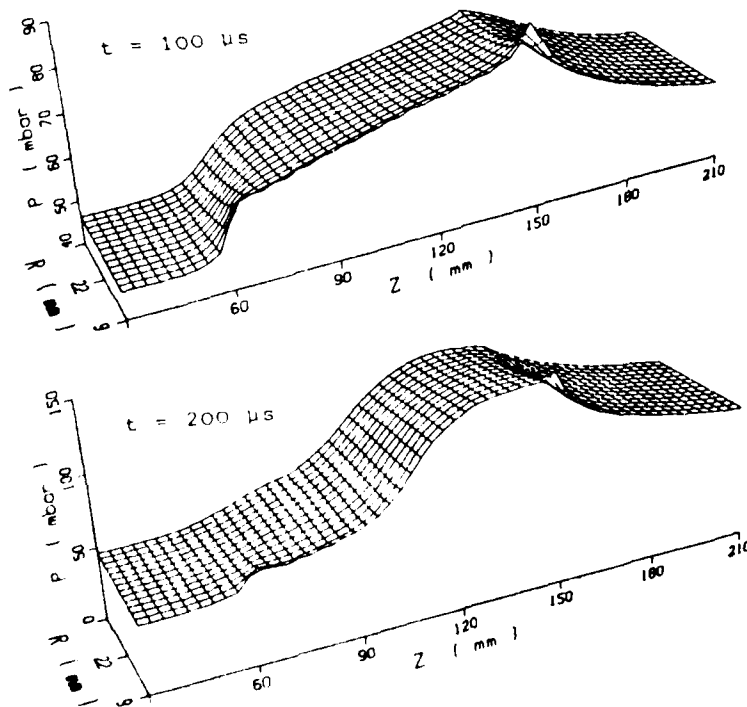


Fig. 81 Pressure distribution within the channel at a) 100  $\mu$ s, b) 200  $\mu$ s.

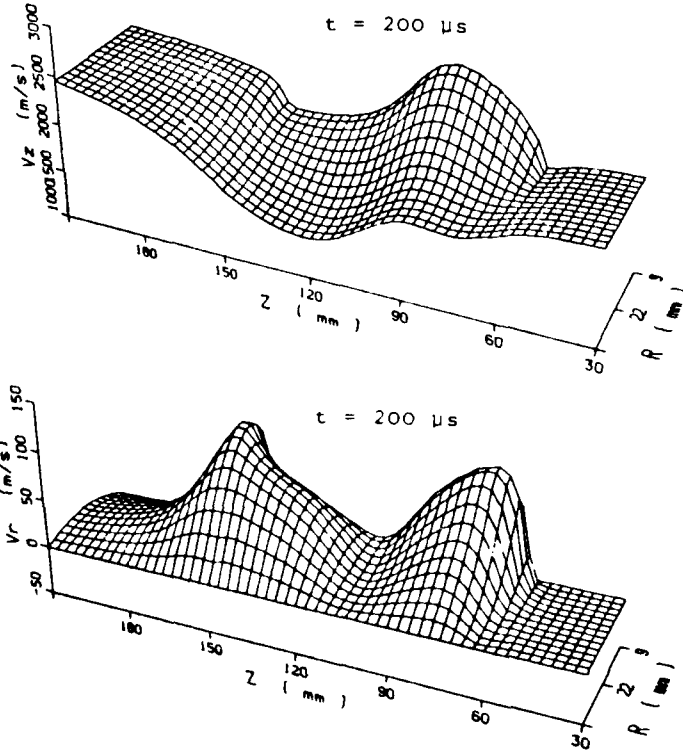


Fig. 82 Velocity distribution at 200  $\mu s$ . a) Axial velocity  $v_z$ , b) radial velocity  $v_r$ .

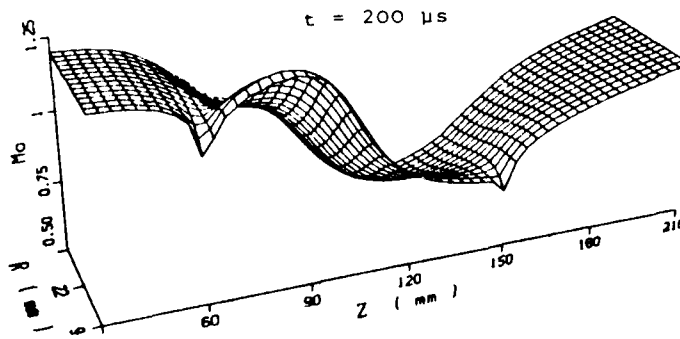


Fig. 83 Mach number distribution at 200  $\mu s$ .

again while reaching an interim maximum at about 1/3 of the cathode length and rises once more behind the electrodes. The minimum at the end of the cathode is caused by the temperature instability at that point. It is remarkable that the Mach number is below 1 within a wide range, especially before the end of the electrodes.

As described in section 5.3, the thrust is composed of an MPD part and a gas dynamic part (see eq. 29a). The pure MPD thrust can be calculated by an integration of the  $\vec{j} \times \vec{B}$  forces within the entire current-carrying volume; another possibility is to use the well-known formula<sup>12</sup>

$$T_{\max} = \frac{\mu_0 I^2}{4\pi} \ln \frac{r_A}{r_C} \quad (33)$$

where  $r_A/r_C$  is the anode to cathode ratio. Both have been done for the example described here with a coincidence of within 1%.

In Fig. 84 the pure MPD thrust (dashed line) and the total thrust (solid line) are plotted depending on time. The total calculated thrust at 400  $\mu s$  lies within a 3% deviation from the expected thrust.

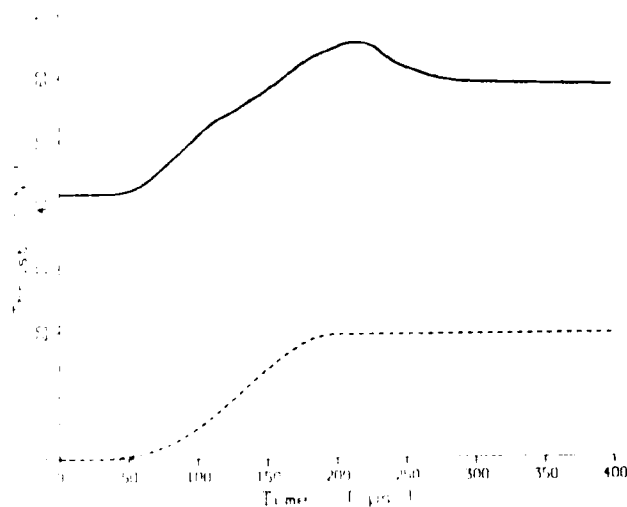


Fig. 84 Thrust versus time. Solid line: total thrust. Dashed line: electromagnetic thrust.

Even more troublesome is the fact that the conservation of mass is only valid within a 10% range. Fig. 85 shows the mass flow versus time at four different channel cross sections.

These deviations from the mass conservation law are an inherent attribute of the MacCormack code.

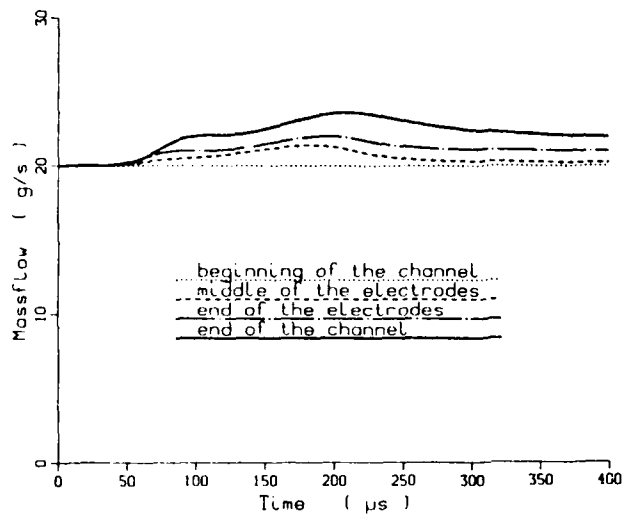


Fig. 85 Mass flow versus time at different channel cross sections.

## 6. Mission Analysis

Parallel to the MPD investigations, some mission analysis was performed to evaluate the employment limits and to justify the development of those thrusters. The output was first an optimization study in which the known results of Langmuir and Irving [56, 57] were refined by better and more realistic assumptions, e.g. by taking the specific power of the power supply unit as a function of the specific impulse. The results were presented at the 21st Joint Propulsion Conference, 1985 (see chapter 7) and will be published in summer 1987 in the Journal of Propulsion and Power.

Second, a trajectory optimization program [58] was modified to allow the calculations of optimal low thrust trajectories. This study is also supported by an ESA contract and is not yet completed (see Samland, chapter 7).

## 7. List of Reports and Publications

During the period of the research grant, the following reports, papers and student theses have been accomplished.

### Interim Scientific Reports

No. 1, Part A - Herbert O. Schrade, Monika Auweter-Kurtz, Helmut L. Kurtz: Plasma Thruster Development. October 1985.

No. 1, Part B - Rolf D. Bühler<sup>+</sup>: Plasma Thruster Development: Magnetoplasmadynamic Propulsion, Status and Basic Problems. (ed. by H. L. Kurtz), published as AFRPL-86-013, February 1986.

### Student Theses

Kettner, B. F.: Nichtlineare, instationäre Wärmebilanzrechnung strahlungsgekühlter Elektroden. Diplomarbeit, ISD, Universität Stuttgart, 1984.

Merke, W. D.: Messung von Strom- Spannungscharakteristiken quasi-stationär betriebener Eigenfeldbeschleuniger. Studienarbeit, Institut für Raumfahrtantriebe, Universität Stuttgart, Stuttgart 1985.

Merke, W. D.: Untersuchungen zur Energiebilanz in einem gepulsten Plasmabeschleuniger. IRS-86-S9, Diplomarbeit, ITLR, Universität Stuttgart, 1986.

Daum. A.: Leistungsmessung an quasi-stationär betriebenen MPD Triebwerken. IRS-87-S6, Studienarbeit, Institut für Raumfahrtssysteme, Universität Stuttgart, 1987.

Ehrlich, H.: Theoretische Untersuchungen zum Einfluß der Düsengeometrie auf die Leistungsdaten eines MPD-Triebwerkes. Diplomarbeit, Institut für Raumfahrtantriebe, Universität Stuttgart, 1985.

Schleinitz, J. P.: Berechnung des Strömungs- und elektrischen Stromdichtefeldes im MPD-Eigenfeldbeschleuniger für isothermes Elektronen- und adiabatisches Ionenverhalten. Diplomarbeit, IRA-85-S1, Institut für Raumfahrtantriebe, Universität Stuttgart, 1985.

Isselhorst, A.: Berechnung des Expansionsvorgangs in einem Plasmatriebwerk unter Berücksichtigung der elektromagnetischen Kompression. Diplomarbeit, IRS, Universität Stuttgart, IRS-87-S5, 1987.

Sleziona, P. C.: Instationäre Berechnung der elektrischen Stromkontourlinien und des Strömungsfeldes im zylindrischen MPD-Triebwerk. Diplomarbeit, IRS, Universität Stuttgart, IRS-86-S7, 1986

von Bülow, H.: Konstruktion eines zylindrischen MPD-Triebwerkes. Diplomarbeit, IRA-86-S4, 1986.

Samland, G.: Berechnung interplanetarer Übergangsbahnen von Raumfahrzeugen mit elektrischen Raketenantrieben. Diplomarbeit, Institut für Raumfahrtsysteme, Universität Stuttgart, Summer 1987.

#### Papers and Publications

Auweter-Kurtz, M., Kurtz, H. L., Schrade, H. O.: Optimization of Propulsion Systems for Orbital Transfer with Separate Power-supplies Considering Variable Thruster Efficiencies. AIAA-85-1152, 21st Joint Propulsion Conference, Monterey, CA, 1985.

Kurtz, H. L., Auweter-Kurtz, M., Schrade, H. O.: Self Field MPD Thruster Design--Experimental and Theoretical Investigations. AIAA-85-2002, 18th International Electric Propulsion Conference, Alexandria, VA, 1985.

Schrade, H. O., Auweter-Kurtz, M., Kurtz, H. L.: Cathode Erosion Studies on MPD Thrusters. AIAA-85-2019, 18th International Electric Propulsion Conference, Alexandria, VA, 1985.

Kurtz, H. L., Auweter-Kurtz, M., Merke, W. D. and Schrade, H.O.: Experimental MPD Thruster Investigations. AIAA-87-1019, 19th International Electric Propulsion Conference, Colorado Springs, CO, 1987.

Auweter-Kurtz, M., Kurtz, H.L., Schrade, H.O. and Sleziona, P.C: Numerical Modeling of the Flow Discharge in MPD Thrusters. 19th International Electric Propulsion Conference, Colorado Springs, CO, 1987.

Acknowledgements

For the support of the Air Force Office of Scientific Research through the European Office of Aerospace Research and Development, all the participants of this research work are greatly indebted.

The authors would like to thank Ms. Rhoda Stephens for typing and for her great help in interpreting and correcting the manuscript.

8. References

- [ 1 ] Vondra, R. J., Caveny, L. H.: Plasma Thruster Research in the U.S.A. Proceedings of the 17th International Electric Propulsion Conference, Tokyo, 1984, pp. 20-27
- [ 2 ] Auweter-Kurtz, M., Kurtz, H. L., Schrade, H. O.: Optimization of Propulsion Systems for Orbital Transfer with Separate Power Supplies Considering Variable Thruster Efficiencies, AIAA-85-1152, AIAA/SAE/ASME, 21st Joint Propulsion Conference, Monterey, CA, 1985
- [ 3 ] Wolff, M., Kelly, A. J., Jahn, R. G.: A High Performance magnetoplasmadynamic Thruster, IEPC 84-32, Proceedings of the 17th International Electric Propulsion Conference, Tokyo, 1984
- [ 4 ] Schrade, H. O., Auweter-Kurtz, M., Kurtz, H. L.: Basic Processes of Plasma Propulsion. Final Report, AFOSR Grant 82-0298, Institute for Space Systems, University of Stuttgart, FRG, 1987
- [ 5 ] Hgel, H.: Flow Rate Limitations in the Selffield Accelerator. AIAA-73-1094, AIAA 10th Electric Propulsion Conference, Lake Tahoe, Nevada, 1973
- [ 6 ] Burton, R. L., Clark, K. E., Jahn, R. G.: Measured Performance of a Multimegawatt MPD Thruster. Journal of Spacecraft and Rockets, Vol 20, No 3, 1983
- [ 7 ] Sovie, R. J., Conolly, D. J.: Effect of Background Pressure on Magnetoplasmadynamic Thruster Operation. Journal of Spacecraft and Rockets, Vol. 7, p. 255, March 1970
- [ 8 ] Cann, G. L., Harder, R. L., Moore, R. A., Lenn, P. D.: Hall Current Accelerator. NASA CR-54705, 1966
- [ 9 ] Krlle, G., Zeyfang, E.: Preliminary Conclusions of Continuous Applied Field Electromagnetic Thruster Research at DFVLR. AIAA-75-417, 1975
- [ 10 ] Hgel, H.: Zur Funktionsweise der Anode im Eigenfeldbeschleuniger. Forschungsbericht DFVLR-FB 80-20, 1980
- [ 11 ] Kuriki, K., Inutake, M.: Establishment of Quasi-steady Operation in a Pulsed MPD Arcjet. AIAA Journal, Vol. 11, No. 2, p. 133, 1973
- [ 12 ] Mcker, H.: Plasmastrmungen in Lichtbgen infolge eigenmagnetischer Kompression. Zeitschrift fr Physik, Vol. 141, p. 198, 1955
- [ 13 ] Yoshikawa, T., Kagaya, I., Kuriki, K.: Thrust and Efficiency of New K-III MPD Thruster. AIAA-82-1887, 1982
- [ 14 ] Maisenhlder, F., Mayerhofer, W.: Jet Diagnostics of a Self-Field Accelerator with Langmuir Probes. AIAA Journal, Vol. 12, No. 9, p. 1203, 1974

- [15] Baksht, F. G., Moizhes, B. J., Rybakov, A. R.: Critical Regime of a Plasma Accelerator. Sov. Phys. Tech. Phys., 18-12, pp. 1613-1616, 1974
- [16] Jahn, R. G., Kelly, A. J., Merfeld, D.: Pulsed Electromagnetic Gas Acceleration. MAE Report 1467 i, Princeton, 1984
- [17] Schrade, H. O., Auweter-Kurtz, M., Kurtz, H. L.: Stability Problems in Magnetoplasma-dynamic Arc Thrusters. AIAA 18th Fluid Dynamics and Plasmadynamics and Laser Conference, Cincinnati, OH, July 1985
- [18] Bühler, R. D.: Plasma Thruster Development: Magnetoplasma-dynamic Propulsion, Status and Basic Problems. AFRPL TR-86-013, February 1986
- [19] King, D. Q., Smith, W. W., Jahn, R. G., Clark, K. E.: Effect of Thrust Chamber Configuration on MPD Arcjet Performance. AIAA-79-2051, 14th International Electric Propulsion Conference, Princeton, NJ, 1979
- [20] Merfeld, D. J., Kelly, A. J., Jahn, R. G.: MPD Thruster Performance: Propellant Distribution and Species Effect. AIAA-85-2022, 18th International Electric Propulsion Conference, Alexandria, VA, 1985
- [21] Seikel, G. R., York, T. M., Condit, W. C.: Applied-Field Magnetoplasma-dynamic Thrusters for Orbit-Raising Missions. in Caveny, L. H. (ed.): Orbit-Raising and Maneuvering Propulsion: Research Status and Needs, Progress in Astronautics and Aeronautics, Vol. 89, AIAA, New York, 1984
- [22] Szimmat, J.: SMART II, Benutzerhandbuch. ISD Report 192, Institut für Statik und Dynamik der Luft- und Raumfahrt-konstruktionen, Universität Stuttgart, 1982
- [23] Kettner, B. F.: Nichtlineare, instationäre Wärmebilanzrechnung strahlungsgekühlter Elektroden. Diplomarbeit, ISD, Universität Stuttgart, 1983
- [24] Jahn, R. G., Kelly, A. J.: Quasi-Steady Magnetoplasma-dynamic (MPD) Thruster Performance Development. MAE Report 1507 d, Princeton, 1983
- [25] Merke, W.: Messung von Strom- Spannungscharakteristiken quasistationär betriebener Eigenfeldbeschleuniger. Studienarbeit, Institut für Raumfahrtantriebe, Universität Stuttgart, Stuttgart 1985
- [26] Di Capua, M. S., Kurtz, H. L.: Electrolytic Capacitor Power Source Design for Quasi-steady MPD Arcs. Journal of Spacecraft and Rockets, Vol 11, No 8, 1974
- [27] Jahn, R. G., Kelly, A. J.: Pulsed Electromagnetic Acceleration. Technical Monthly Progress Report, MAE Report No. 1692.8, Princeton University, Princeton, NJ, 1985

- [28] Daum, A.: Leistungsmessung an quasi-stationär betriebenen MPD Triebwerken. IRS-87-S6, Studienarbeit, Institut für Raumfahrtssysteme, Universität Stuttgart, 1987
- [28] Merke, W.: Untersuchungen zur Energiebilanz in einem gepulsten Plasmabeschleuniger. IRS-86-S9, Diplomarbeit, ITLR, Universität Stuttgart, 1986
- [30] Kuriki, K., Shimizu, Y., Morimoto, S., Kuwahara, K., Kisaragi, T., Uematsu, K., Enya, S., Sasao, Y.: MPD Arcjet System Performance Test. IAF Preprint 83-392, 34th IAF Congress, Budapest, Hungary, 1983
- [31] Clark, K. E. and Jahn, R. G.: Magnetoplasmadynamic Thruster, Erosion Studies, Phase I. Interim Report, AF Contract No. R 04611-79-C-0039, April 1983
- [32] Hügel, H. and Krülle, G.: Phänomenologie und Energiebilanz von Lichtbogenkathoden bei niedrigen Drücken und hohen Stromstärken. Beiträge der Plasmaphysik, Vol. 9, p. 87, 1969
- [33] Schrade, H. O., Auweter-Kurtz, M. and Kurtz, H. L.: Plasma Thruster Development. Report, IRA 85-P3, Institut für Raumfahrtantriebe, Universität Stuttgart, April 1985
- [34] Guile, A. E. and Jüttner, B.: Basic Erosion Processes of Oxidized and Clean Metal Cathodes by Electric Arcs. IEEE-Transactions on Plasma Science, Vol. P.S.-8, No. 3, p. 259, 1980
- [35] Harris, L. P.: Arc Cathode Phenomena. Contribution in "Vacuum Arcs, Theory and Application", J. M. Lafferty, ed., John Wiley & Sons, New York, 1980
- [36] Bushik, A. I., Jüttner, B., Pursch, H. and Shilov, A.: Effects of Local Heat Accumulation at the Cathode of Vacuum Arcs. Preprint: Akademie der Wissenschaften der DDR, Zentralinstitut für Elektronenphysik, Feb. 1983
- [37] Djakov, B. E. and Holmes, R., Journal of Phys. D. Appl. Phys., Vol. 4, p. 504, 1971
- [38] Daalder, J. E., IEEE Trans. Power Appar. Syst., PAS-93, p. 1747, 1974
- [39] Roman, W. C., Proceedings of the Vth International Conference on Phenomenon in Ion Gases, p. 287, Paris, 1963
- [40] Murphree, D. L. and Carter, R. P., AIAA-Journal, Vol. 7, p. 1430, 1969
- [41] Good, R. H. and Müller, E. W.: Field Emission. contr. in Encyclopedia of Physics, "Electron-Emission and Gas Discharges I", ed. by S. Flügge, Vol. XXI, Springer Verlag, Berlin, 1956

- [42] Ecker, G.: Electrode Components of the Arc Discharge. in Ergebnisse der exakten Naturwissenschaften, Vol. 33, p. 1, 1961
- [43] Schrade, H. O., Auweter-Kurtz, M. and Kurtz, H. L.: Analysis of the Cathode Spot of Metal Vapor Arcs. IEEE Transactions on Plasma Science, Vol. PS-11, No. 3, p. 103, 1983
- [44] Schrade, H. O.: MPD Effects in Electric Arcs. Interim Scientific Report, Grant AFOSR 82-0298, 1983
- [45] Tuma, D. T. et al., Journal of Applied Physics, Vol. 49, 1978
- [46] Hügel, H.: Zur Strömung kompressibler Plasmen im Eigenfeld von Lichtbogenentladungen. DLR-FB-70-13, 1970. Publishing Co.: Wissenschaftliches Berichtswesen der DFVLR, Postfach 906058, D-5000 Köln 90
- [47] King, D. Q.: Magnetoplasmadynamic Channel Flow for Design of Coaxial MPD Thrusters. Ph.D. thesis, Department of Mechanical and Aerospace Engineering, Princeton University, 1981; also available as MAE Report 1552
- [48] Minakuchi, H. and Kuriki, K.: Magnetoplasmadynamic Analysis of Plasma Acceleration. 17th International Electric Propulsion Conference, IEPC 84-06, Tokyo, 1984
- [49] Kimura, I., Toki, K. and Tanaka, M.: Current Distribution on the Electrodes of MPD Arcjets. AIAA Journal, Vol. 20, No. 7, p. 889, 1982
- [50] Lawless, J. L. and Subramaniam, V. V.: A Theory of Onset in MPD-Thrusters. AFOSR-Report 83-0033, 1983
- [51] Heimerdinger, D.: An Approximate Two-Dimensional Analysis of an MPD Thruster. SSL 9-84, MIT, Cambridge, Mass., June 1984
- [52] Ehrlich, H.: Theoretische Untersuchungen zum Einfluß der Düsengeometrie auf die Leistungsdaten eines MPD-Triebwerkes. Diplomarbeit, Institut für Raumfahrtantriebe, Universität Stuttgart, 1985.
- [53] Isselhorst, A.: Berechnung des Expansionsvorgangs in einem Plasmatriebwerk unter Berücksichtigung der elektromagnetischen Kompression. Diplomarbeit, IRS, Universität Stuttgart, IRS-87-S5, 1987
- [54] Sleziona, P.C.: Instationäre Berechnung der elektrischen Stromkontourlinien und des Strömungsfeldes im zylindrischen MPD-Triebwerk. Diplomarbeit, IRS, Universität Stuttgart, IRS-86-S7, 1986
- [55] Jacobi, H.: Entwicklung eines theoretischen Modells zur Beschreibung der Wechselwirkung zwischen elektrischer Entladung und Überschallströmung eines gepulsten CO-Lasers. DFVLR-FB 84-45, 1984. Publishing Co.: Wissenschaftliches Berichtswesen der DFVLR, Postfach 906058, D-5000 Köln 90

- [56] Langmuir, D. B.: Low Thrust Flight: Constant Exhaust Velocity in Field-Free Space. in "Space Technology", Seifert, H. S. (ed.), John Wiley and Sons, New York, 1959
- [57] Irving, J. H.: Low Thrust Flight: Variable Exhaust Velocity in Gravitational Fields. in "Space Technology", Seifert, H. S. (ed.), John Wiley and Sons, New York, 1959
- [58] Schöttle, U. M.: Trägeroptimierungs- und Simulationsprogramm (TOPS). Institut für Raumfahrtantriebe, Programmversionen, 1979-1985

END

10-87

DTIC